Dissertation
submitted to the
Combined Faculties of the Natural Sciences and for Mathematics
of the Ruperto-Carola University of Heidelberg, Germany
for the degree of
Doctor of Natural Sciences

Put forward by

Diplom-Astronom:	Sergey Koposov
Born in:	Podolsk, Moscow region, Russia

Oral examination: 4 November 2009

Understanding the Milky Way Halo through Large Surveys

Referees: Prof. Dr. Hans-Walter Rix

Dr. habil. Andreas Just

Zusammenfassung

Diese Doktorarbeit beschreibt Untersuchungen der stellaren Feinstruktur in den Randgebieten der Milchstraße (MS), wobei die Analyse von SDSS Daten mit theoretischen Modellen verbunden wurde. Solche Feinstruktur, welche entweder aus gebundenen Sternhaufen und Satellitengalaxien oder aus durch Gezeitenkräfte zerrissenen Objekten in Form von Sternenströmen besteht, liefert wertvolle Aufschlüsse über die Dynamik und Entstehungsgeschichte der MS. Basierend auf SDSS-Katalogen habe ich eine Methode entwickelt, um nach stellaren Überdichten im Halo der MS zu suchen. Dies führte zu der Entdeckung der kleinsten und sternärmsten ($\sim 1000 L_{\odot}$) Kugelsternhaufen, mit Relaxationszeiten $\ll t_{Hubble}$. Durch die detaillierte Analyse von SDSS-Daten eines bekannten Sternenstroms (GD-1) war ich imstande, dessen 6-D Phasenraumstruktur über 60 Grad am Himmel zu kartieren. Durch Modellierung des Orbits dieses Stroms konnte ich das galaktische Potential stark eingrenzen, u.a. $V_{circ}(R_0) = 224 \pm 13$ km/s. Die Anwendung der algorithmischen Suche nach stellaren Überdichten auf den SDSS-Datensatz sowie auf Pseudodatensätze erlaubte es mir, die gravierende radiale Unvollständigkeit bei der erfolgreichen Suche nach ultraschwachen Zwerggalaxien zu verstehen und dadurch die Leuchtkraftfunktion von Satellitengalaxien der MS bis zu Leuchtkräften von $M_V \approx -3$ zu bestimmen. Um die Vorhersagen des CDM-Modells für die Satellitenpopulation der Milchstraße mit Beobachtungen zu vergleichen, verwendete ich ein semi-analytisches Modell. Dieser Vergleich hat gezeigt, dass die derzeitig wachsende Zahl von Satellitengalaxien der MS, ein besseres Verständnis der radialen Unvollständigkeit sowie die Unterdrückung der Sternentstehung nach der Reionisation das "missing satellite problem" vollständig zu lösen imstande sind.

Abstract

This thesis presents an extensive study of stellar substructure in the outskirts of the Milky Way(MW), combining data mining of SDSS with theoretical modeling. Such substructure, either bound star clusters and satellite galaxies, or tidally disrupted objects forming stellar streams are powerful diagnostics of the Milky Way's dynamics and formation history. I have developed an algorithmic technique of searching for stellar overdensities in the MW halo, based on SDSS catalogs. This led to the discovery of unusual ultra-faint $\sim (1000 L_{\odot})$ globular clusters with very compact sizes and relaxation times $\ll t_{Hubble}$. The detailed analysis of a known stellar stream (GD-1), allowed me to make the first 6-D phase space map for such an object along 60 degrees on the sky. By modeling the stream's orbit I could place strong constraints on the Galactic potential, e.g $V_{circ}(R_0) = 224 \pm 13$ km/s. The application of the algorithmic search for stellar overdensities to the SDSS dataset and to mock datasets allowed me to quantify SDSS's severe radial incompleteness in its search for ultra-faint dwarf galaxies and to determine the luminosity function of MW satellites down to luminosities of $M_V \approx -3$. I used the semi-analytical model in order to compare the CDM model predictions for the MW satellite population with the observations; this comparison has shown that the recently increased census of MW satellites, better understanding of the radial incompleteness and the suppression of star formation after the reionization can fully solve the "Missing satellite problem".

To my high school teachers: Galina Ionovna Eseleva, Dmitriy Genrihovich Kuznetsov and Rudolf Karlovich Bega

Contents

List of Figures

List of Tables

LIST OF TABLES

1

Introduction

Nowadays the field of observational cosmology is developing very rapidly. New datasets are coming from different instruments and surveys such as WMAP, 2dF, HST, HESS, SDSS, SWIFT (Aharonian et al., 2006; Colless et al., 2001; Gehrels et al., 2004; Riess et al., 2004; Spergel et al., 2007; York et al., 2000) and others. These datasets are confronting the existing cosmological models and theories, which in turn, are evolving and adapting to the new data (Benson et al., 2002; Bower et al., 2006; Gnedin et al., 2004; Somerville and Primack, 1999; Tegmark et al., 2006). Despite the significant improvements both in the theoretical cosmology and in the observations, many questions about galaxy formation and evolution are still waiting to be answered.

One of the keystones of the existing theories of galaxy formation is the Cold Dark Matter (CDM) paradigm. The basic concepts of the CDM paradigm of galaxy formation have been around for thirty years (Fall and Efstathiou, 1980; White and Rees, 1978) and their creation was motivated by the growing amount of evidence (Rubin et al., 1978; Zwicky, 1933) that all galaxies are baryon condensates at the bottom of massive dark halos (White and Rees, 1978). Despite the fact that the nature of the matter constituting dark halos is still unknown (Bergström, 2000; Bertone et al., 2005, and references therein), the CDM paradigm has been very successful in explaining observations and making observational predictions.

In the ΛCDM (i.e. CDM + dark energy) universe baryonic structure formation starts at redshift ∼1000 when the ionized hydrogen recombines (Blumenthal et al., 1984; Dicke et al., 1965; Peebles, 1968). Before the recombination, baryons were in quasi-equilibrium with the radiation field and were distributed almost uniformly, but

after the recombination baryons do not feel radiation pressure anymore and start to fall in the potential wells formed by dark matter (White and Rees, 1978), which started to collapse much earlier than the epoch of recombination. As the baryons cooled and formed the first molecular clouds in the most massive dark matter halos, first stars formed at a redshift of $\sim 20-50$. These stars are thought to be formed in dark matter halos with masses of $\sim 10^5 - 10^6 M_\odot$ (see Abel et al., 2002, and references therein). Due to the absence of metals in the early universe, the first stars were very hot, massive and short-lived. When these stars formed, they started to ionize and chemically enrich the surrounding interstellar and intergalactic medium. As the number of stars in the Universe increased, the Strömgren spheres from the first galaxies started to overlap. And finally the whole universe became ionized again at redshift $\sim 7-11$ (Barkana and Loeb, 2001; Fan et al., 2006; Gnedin and Ostriker, 1997). Subsequent growth and evolution of galaxies takes place by continuing accretion of baryons and star formation in the centers of dark matter halos following the picture of White and Rees (1978) combined with hierarchical merging. The important effects modulating the galaxy formation within that picture are gas cooling efficiency in the presence of UV ionizing background (Quinn et al., 1996; Thoul and Weinberg, 1996), stellar feedback (Dekel and Silk, 1986; Martin, 1999), AGN feedback (Springel et al., 2005, and references therein), environmental effects occurring in dense environments leading to gas stripping and star formation quenching (Abadi et al., 1999; Grebel et al., 2003), and satellite accretion (Abadi et al., 2003; Hernquist and Mihos, 1995). As a result of these complicated processes the star formation efficiency and therefore the galaxy properties are strong functions of dark matter halo masses (Benson et al., 2003; van den Bosch et al., 2007): star formation seems to be inefficient both at the very massive end of the dark matter halo mass function and at its low-mass end, although current model predictions for low-mass galaxy formation are quite uncertain.

ΛCDM is particularly successful in the explanation of large scale structure (Cole et al., 2005; Eisenstein et al., 2005) and the Cosmic Microwave Background (CMB) (Dunkley et al., 2009). But a number of ΛCDM predictions on small scales were found to be discrepant from the observations. The perfect test-bed for testing CDM predictions at small scales is the Milky Way and when, in 1999, Klypin et al. (1999) and Moore et al. (1999) compared the number of MW satellites predicted by CDM with the number of actually observed MW satellites they found that CDM predicted hundred

times too many subhalos around the MW (see also Kauffmann et al., 1993), compared to the known (at the time) MW satellite galaxies. This problem has been called the "missing satellite" problem and has been a major issue for the CDM paradigm for the last decade. Furthermore, in the CDM galaxy formation picture the hierarchical nature of galaxy formation predicted that the MW halo should be filled with, or even constituted of remnants of accreted smaller systems (e.g. stellar streams Bullock and Johnston, 2005), when only one stellar stream was known in the MW halo (Sagittarius) by 2000. The apparent lack of substructure in the MW halo lead to both theoretical attempts to reduce the amount of small scale structure in the models (Bode et al., 2001; Narayanan et al., 2000; Zentner and Bullock, 2003) and to observational attempts to discover the predicted substructures with the advent of large homogenous sky surveys such as 2MASS, SDSS. The observational searches for substructure in these surveys turned out to be very successful, and significant substructure such as globular clusters, dwarf galaxies and stellar streams have been found in the halos of the Milky Way and other nearby galaxies (e.g. Belokurov et al., 2006c, 2007c; Ferguson et al., 2002; Grillmair and Dionatos, 2006b; Ibata et al., 2001; Majewski et al., 2003; Odenkirchen et al., 2001). This slightly alleviated the substructure problem in the CDM, but did not fully solve it.

The search and analysis of the substructure in halos of galaxies is particularly important because it gives us clues to the history of the accretion process and the build-up of the Galaxy. The pioneering work in the field was the paper of Searle and Zinn (1978) who used the metallicities of globular clusters to infer the formation history of the MW halo. Since then the field of "galactic archaeology" has achieved important results (see e.g Fellhauer et al., 2006; Helmi, 2004; Helmi et al., 1999; Ibata et al., 2001; Koch et al., 2006; Koposov et al., 2009a). Through the study of substructure we also have a unique chance to see the lowest-luminosity galaxies formed in the early universe and through them probe the star formation process at high redshifts (Koposov et al., 2009b; Ricotti and Gnedin, 2005).

Another interesting aspect of studying the substructure in the MW halo is related to stellar dynamics. It is important to understand that the dynamics of stellar structures in the halo may constitute a regime opposite to "classical dynamics", where everything is phase-mixed and virialized. Instead (see e.g. Bell et al., 2008; Grillmair, 2009; Klement et al., 2009), the halo seems to consist of large numbers of different structures

possibly originating from different accretion events, which are not mixed, because the mixing time is of the order of the Hubble time. It turns out that the study of these unrelaxed substructures in the MW halo may be very helpful in order to trace the Galactic potential (Fellhauer et al., 2006; Koposov et al., 2009a). Proper analysis of these structures in the MW halo is important because the era of the GAIA (Perryman et al., 2001) space mission is coming, and we will have soon a multi-dimensional phase-space picture of the MW halo with a much larger number of substructures.

This thesis is devoted to the analysis and the understanding of some of the galaxy formation and CDM problems mentioned above, by studying our MW: a possible solution of the substructure problem in CDM models based on new data and a better understanding of observational uncertainties (Chapters 4, 5), new models of the formation of low-mass galaxies (Chapter 5), and new methods of the analysis of stellar substructures in the MW halo (Chapters 2, 3).

The thesis is structured as follows: In Chapter 2 we present the discovery of two highly unusual globular clusters in the SDSS that resulted from the first application of our algorithmic substructure search. We determine the properties of these clusters such as their ages, relaxation times and distances to these objects. We discuss the possible evolutionary status of the discovered objects and their possible association to the Sagittarius stellar stream. In Chapter 3 we analyse the properties of the halo stellar stream named GD-1, presumed to be the remnant from the accretion of a globular cluster in the MW halo. We use the SDSS data as well as our own observations in order to construct the 6-dimensional map of the stream in phase space. We fit this 6-D map of the stream by a single test-particle orbits in different Galactic potentials. Later we use these fits in order to put strong constraints on the parameters of the potential, such as its flattening (of the overall potential) and the circular velocity at the Sun's position. We also try to put constraints on the flattening of the MW dark matter halo. Chapters 4 and 5 are devoted to our attempts to solve the "missing satellite" problem with the SDSS data. In Chapter 4 we describe the methods employed to search for substructure in the MW halo, the determination of the incompleteness of these searches and the measurement of the luminosity function of the MW satellites after correcting for incompleteness. We illustrate that the searches for dwarf galaxies are significantly incomplete at the faint end of the luminosity function and that the luminosity function of dwarf galaxies is much flatter than the mass function of DM

halos, which suggests some suppression of star formation in these low mass DM halos. In Chapter 5 we use a semi-analytical model for star formation in dwarf galaxies in order to reproduce the observed number and properties of the MW satellites. In the comparison with observations we take into account the incompleteness effects analyzed in Chapter 4. In our semi-analytical model we consider different important physical effects such as the suppression of star formation after the epoch of reionization due to the UV background, the suppression of star formation in small dark matter halos before the epoch of reionization due to the destruction of H_2 molecules, or feedback effects. By comparing the predictions of our models with observations we confirm the importance of the suppression of star formation in low-mass dark matter halos. Finally we find that our model can fully reproduce the observed number and properties of the MW satellites, thereby giving the possible solution to the "missing satellite" problem. Chapter 6 concludes the thesis and discusses the possible improvements and future prospects of the methods presented in the thesis.

2

The discovery of two globular clusters

This chapter reproduces the paper: S. Koposov, J. T. A. de Jong, V. Belokurov, H.-W. Rix, D. B. Zucker, N. W. Evans, G. Gilmore, M. J. Irwin, and E. F. Bell. "The Discovery of Two Extremely Low Luminosity Milky Way Globular Clusters" published in ApJ, volume 669, page 337-342, November 2007.

2.1 Introduction

The population of globular clusters around the Milky Way has been studied extensively and the current census finds the majority at low latitudes in the inner Galaxy ($R_{\rm GC} < 20\,{\rm kpc}$). Globular clusters are almost universally "old" ($t_{\rm age} \approx 0.5 - 1 \times t_{\rm Hubble}$), show no convincing evidence for dark matter, and have characteristic luminosities of $10^5 L_\odot$ ($M_V \sim -8$) and typical sizes of 3 pc. Yet, the observed range of structural properties (e.g. mass, size, and concentration) is quite wide. This range is of great interest, as it appears to be determined by a set of astrophysical processes: the initial structure and orbit; subsequent external processes, such as galactic tides and dynamical friction; and ensuing mass segregation, evaporation and core collapse (see e.g., Gnedin and Ostriker, 1997; Meylan and Heggie, 1997). Indeed, there has long been a sense that the observed population of Galactic globular clusters mainly reflects the subset of objects that could survive for $\sim t_{\rm Hubble}$. In individual cases, there is clear evidence for internal reshaping processes (as in M15, Sosin and King, 1997) and tidal disruption (as in Pal5,

Odenkirchen et al., 2001). Within this context, identification and study of globulars with extreme properties is undoubtedly of great interest.

Our census of objects at the outskirts of the Milky Way has increased rapidly in the last few years, mostly based on large-area CCD surveys like the Sloan Digital Sky Survey (SDSS; York et al., 2000). Recent searches for Galactic halo objects have not only found many dwarf galaxies (Belokurov et al., 2007c; Irwin et al., 2007; Willman et al., 2005b; Zucker et al., 2006b), but also added 2 faint and extended objects that may be Milky Way globulars. The newcomers, Willman 1 and Segue 1, both have distorted irregular isopleths, perhaps indicating ongoing tidal disruption. Willman 1 seems to show some evidence for dark matter and metallicity spread (Martin et al. 2007 in prep.), casting some doubt on whether it is a globular cluster at all.

Here, we announce the discovery of two new, distant, extremely faint and compact ($\sim 3\,$pc) globular clusters, named Koposov 1 and Koposov 2, first detected in SDSS Data Release 5 (DR5) and subsequently confirmed with deeper imaging at Calar Alto. The total luminosity of Koposov 2 appears to be $\sim -1^m$, lower than that of the faintest Galactic globular known to date, AM 4 (-1.4^m, Inman and Carney, 1987). Koposov 1 is not much brighter: at $M_{V,tot} \sim -2^m$, it has the third-lowest luminosity. In total, only 3 out of the previously-known ~ 160 Galactic clusters, have comparably low luminosity and small sizes: AM 4, Palomar 1, and Whiting 1 (Whiting et al., 2002). Willman 1 and Segue 1 also have extremely low luminosities but are an order-of-magnitude larger.

Here, we describe the deep follow-up data confirming the discoveries and give estimates of the structural parameters of the new objects. We argue that the discovery of these two low-mass globulars in less than 1/5 of the sky may mean a substantial population of such clusters lurks in the outer halo of the Milky Way.

2.2 Discovery and observations

The two new globular clusters were originally selected amongst other candidates in the course of our systematic search for small-scale substructure in the Milky Way halo. The aim of the search was to detect all significant small-scale stellar overdensities above the slowly-varying Galactic background that are likely to be either dwarf spheroidal galaxies or globular clusters. A detailed description of the algorithm and its efficiency will be provided in next chapters, and we only present here a brief outline of the method. The

algorithm is based on the so-called Difference of Gaussians method, first developed in Computer Vision (Babaud et al., 1986; Lindeberg, 1998). Starting from a flux-limited catalog of stellar positions, the number-counts map in (α, δ) plane is convolved with a filter optimized for the detection of overdensities, namely the difference of two 2-D Gaussians (Koposov et al., 2008b). Having zero integral, the kernel guarantees that the convolution with a constant (or slowly varying) background will result in zero signal. When the data contains an overdensity with a size comparable to the size of the inner Gaussian, the filter will be close to optimal.

We applied this filtering procedure to the entire stellar subset of the DR5 source catalog with $r < 22^m, g - r < 1.2^m$. In our analysis we used the photometry cleaned by switching on quality flags as described in SDSS SQL pages [1] This minimizes the influence of various artefacts including those caused by proximity of very bright or extended objects. In the resulting map that had been convolved with a $2'$ kernel, we found two very compact objects among other overdensities ranked highly according to their statistical significance. Figure 2.1 shows the SDSS images and Figure 2.2 shows the spatial distribution of extracted sources, where central concentrations of stars are clearly visible. These concentrations are detected at high level of significance. The areas of $1'$ radius marked by circles centered on Koposov 1 and 2 plotted in Figure 2.2 contain 22 objects and 23 objects respectively while mean density of $g-r < 0.6^m$ $r > 20^m$ stars should produce approximately 2.5 objects, which implies a high statistical significance of the overdensities – for pure Poisson distribution of objects, the probability to find such group of stars in all DR5 is around 10^{-9}.

The differential Hess diagrams for stars within $2'.5$ radius centered on the objects are shown in Figure 2.3. There is a clear excess of blue stars ($g - r < 0.5$), which we interpret as main sequence turn-off stars at $r \sim 22$, which roughly corresponds to distances of $\sim 50\,\mathrm{kpc}$.

To confirm the nature of discovered candidates and quantify their structural and population properties, we acquired follow-up GTO observations in January 2007 on the 2.2m telescope at Calar Alto using the CAFOS camera. This camera has a $2k \times 2k$ CCD with a $16' \times 16'$ field of view and a pixel scale of $0''.5$/pix. We observed each object for a total of 2 hours in Johnson B and 1.5 hours in Cousins R. The integrations were split in 5 individual dithered exposures for cosmic ray and bad pixel rejection.

[1] `http://cas.sdss.org/dr5/en/help/docs/realquery.asp#flags`

2. THE DISCOVERY OF TWO GLOBULAR CLUSTERS

Figure 2.1: $3' \times 3'$ SDSS cutout images of Koposov 1 and 2. The bright star in the center of Koposov 1 is a foreground star with $V \sim 14.5^m$ and large proper motion $(\mu_\alpha, \mu_\delta) \sim (-32, -12)$ mas/yr, according to the USNO-B1.0 catalog (Monet et al., 2003). The bright extended object near the center of Koposov 2 is a background galaxy.

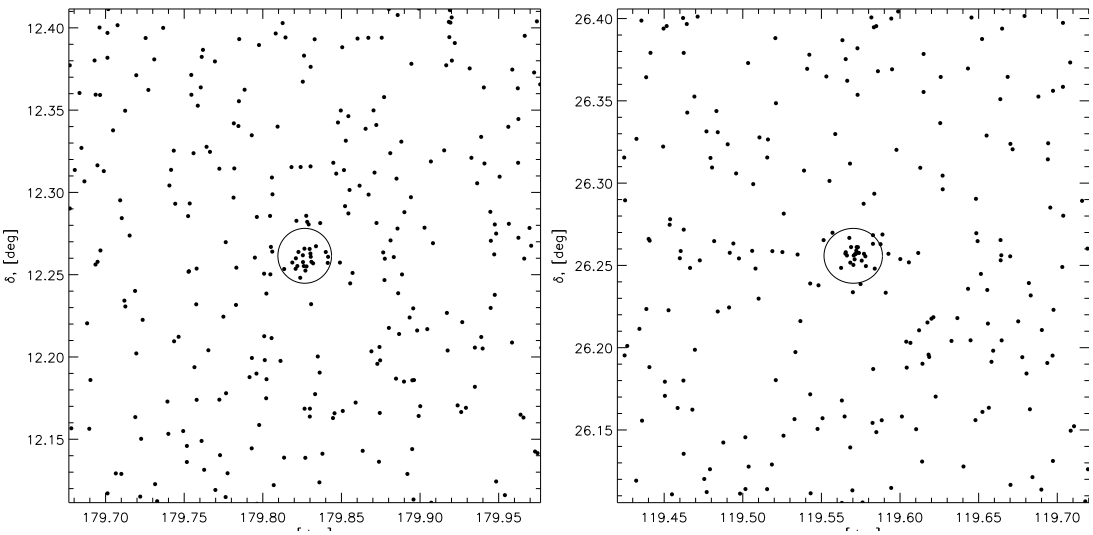

Figure 2.2: The spatial distribution of the objects in the area of Koposov 1 and Koposov 2. All objects classified as stars with colors $(g - r) < 0.6^m$ and $r > 20^m$ in the area $0.3^\circ \times 0.3^\circ$ are shown. The circles with $1'$ radii centered on the objects are overplotted.

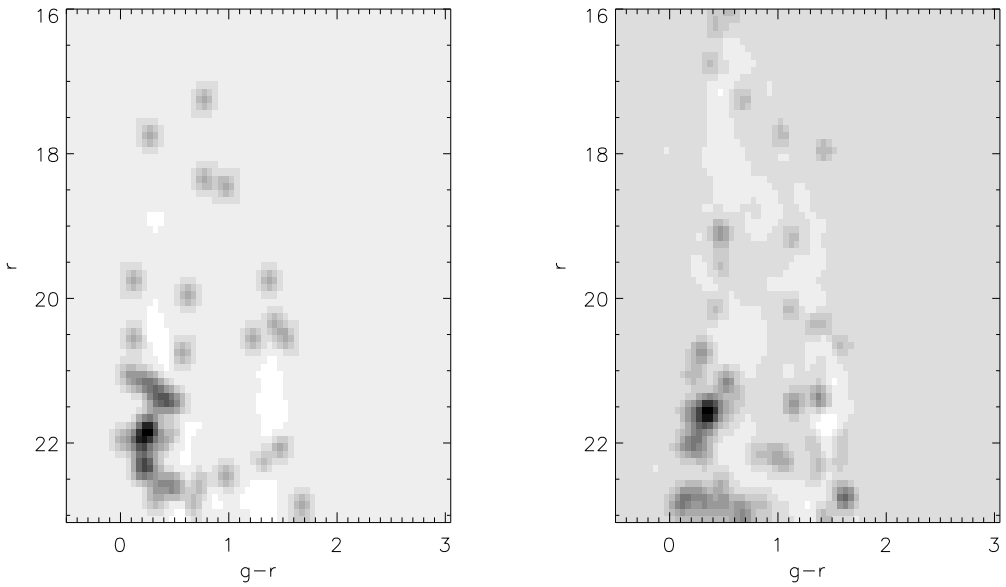

Figure 2.3: The residual $g - r$ versus g Hess diagrams of the clusters from the SDSS data. In each case the residual Hess diagram is constructed by subtracting the normalized background Hess diagram from the Hess diagram of stars lying within $2'.5$ radius from the centers of objects

The observations were carried out in good photometric conditions with a seeing of $1'' - 1.3''$. The data was bias-subtracted and flat-fielded. The individual frames were WCS-aligned, drizzled and median-combined using our software and the SCAMP and SWARP programs (Bertin, 2006). The combined B band images of the objects are shown in Figure 2.4.

The central stellar overdensities are clearly corroborated by the Calar Alto photometry, which is nearly 2 magnitudes deeper than the original SDSS data. While the follow-up data are quite deep, the stars are subject to significant crowding, due to the compactness of the clusters. Therefore, for the purposes of robust source detection and photometry, we used the DAOPHOT/ALLSTAR software (Stetson, 1987). To get the absolute calibration of the photometry from each frame, we cross-matched the DAOPHOT sources with the SDSS catalog using the Virtual Observatory resource SAI CAS [1] (Koposov et al., 2007a). To convert the Sloan g and r magnitudes into the Johnson-Cousins photometric system, we used the conversion coefficients from Smith

[1] `http://vo.astronet.ru/cas`

et al. (2002). The resulting B versus $B-R$ color-magnitude diagrams of the central regions of the objects together with the color-magnitude diagrams of the comparison fields, extending to $B \sim 23.5^m - 24^m$, are shown in the Figure 2.5. The median photometric accuracy of the data is 0.05–0.1 magnitude. The color magnitude diagrams clearly show the presence of the main sequences near the centers of the objects, while they are absent in the the comparison fields. Also, the statistical significance of the overdensities is clearly supported by the new data. The CMD diagram of objects within $2'$ from the center of Koposov 1 contain 96 objects, while the background density inferred from the comparison field should give around 23 objects, which gives a 15 sigma deviation. For Koposov 2 , the number of objects within $1.2'$ is 92 while the background density from the comparison field should produce around 24 objects, which gives a 14 sigma deviation. In the next section we will discuss the properties of the objects which can be derived from the follow-up data.

2.3 Properties

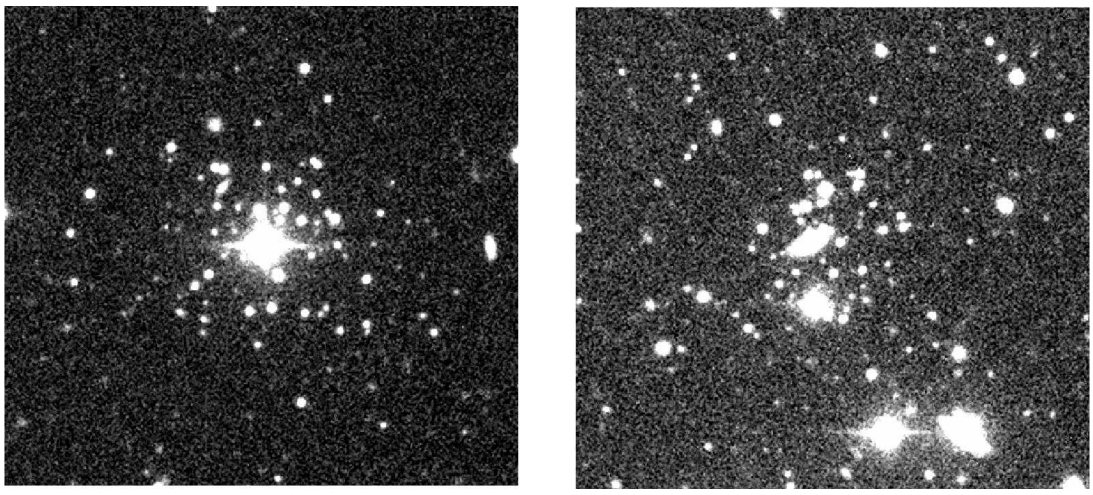

Figure 2.4: B band Calar Alto view of Koposov 1 and Koposov 2. The $2' \times 2'$ images are centered on the clusters (North is up, East is left).

The color-magnitude diagrams (CMDs) of the objects from the Calar Alto data (Figure 2.5) clearly show a distribution of stars which can be attributed quite convincingly to an old main sequence. In the case of Koposov 1, the MS turn-off is clear-cut, while for the second cluster, it is not so well defined. To estimate the distances to the

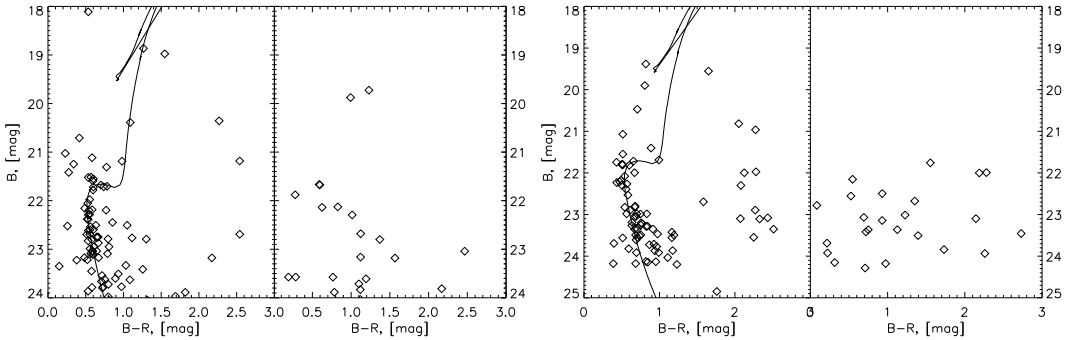

Figure 2.5: *Left panel (left half)*: B versus $B-R$ CMDs derived from the Calar Alto data for stars lying within $2'$ of Koposov 1 with 8 Gyr and [Fe/H]$= -2$ Girardi et al. (2000) isochrones overplotted. *Left panel (right half)*: for comparison, the CMDs of stars in the annulus centered on Koposov 1 defined by radii $3.2'$ and $3.7'$. *Right panel (left half)* : B versus $B-R$ CMDs of stars lying within $1.'2$ of Koposov 2 with 8 Gyr and [Fe/H]$= -2$ Girardi et al. (2000) isochrones overplotted. *Right panel (right half)*: for comparison, the CMDs of stars in the annulus centered on Koposov 2 defined by radii $2'$ and $2.3'$.

objects, we overplot in Figure 2.5 the 8 Gyr [Fe/H]$= -2$ isochrones from Girardi et al. (2000). For Koposov 1, this gives a distance of 50 kpc. For Koposov 2, the estimate is 40 ± 5 kpc, but it is not well constrained due to a lack of MS turn-off stars. The angular diameters of the clusters are $< 0.5'$, which translates into a physical size of $r \sim 5$ pc. Unfortunately, the number of stars detected in the central regions is not enough to measure precisely half-light radii of the objects; our best estimate is $r_h \sim 3$ pc. For Koposov 1, we subtracted the bright foreground star near the center, integrated the light of the whole cluster in apertures and fitted it to a Plummer profile with $r_h = 3$ pc. For Koposov 2, r_h we performed a maximum likehood fit with $r_h \sim 3$ pc. Moreover, the minuscule number of stars in both clusters does not allow us to establish firmly their total luminosities. Our estimate of $-1 \gtrsim M_V \gtrsim -2$ is based on the absence of the giants in these clusters and the visible similarity of the CMDs to that of the lowest luminosity globular AM4 ($M_V = -1.6$, Inman and Carney, 1987). We checked that estimate by simple Monte-Carlo experiment: using the Salpeter IMF and Girardi isochrones we simulated fake clusters and deduced that the clusters with $-1 \gtrsim M_V \gtrsim -2$ have the number of stars within 1.5-2 magnitudes below the turn-off is close to the observed number of stars (50-70) in our objects. We must say also that due to the intrinsic faintness of the clusters and low number of stars in them the estimates of the total lu-

minosity and especially the age have large uncertainties. But with the existing data we can not do any better. Much deeper and accurate photometry may be required to get precise age/luminosity measures. The spectroscopic observations would be interesting in constraining the metallicity of these objects, which is currently completely unknown.

We note that the CMD of Koposov 1 shows several stars brighter and bluer than the tentative MS turn-off, which we interpret as blue stragglers. This hypothesis is not implausible considering the low luminosity of the cluster and taking into account the observed anti-correlation between the frequency of blue stragglers and the luminosity of the globular cluster (Piotto et al., 2004).

The distance and the position of Koposov 1 suggest that this cluster may be related to the Sagittarius tidal stream. Its location is a good match to the distant tidal arm discovered in Belokurov et al. (2006c). Figure 2.6 shows the arms of the Sagittarius stream in the DR5 slice around $\delta \sim 10^\circ$ and the position of Koposov 1.

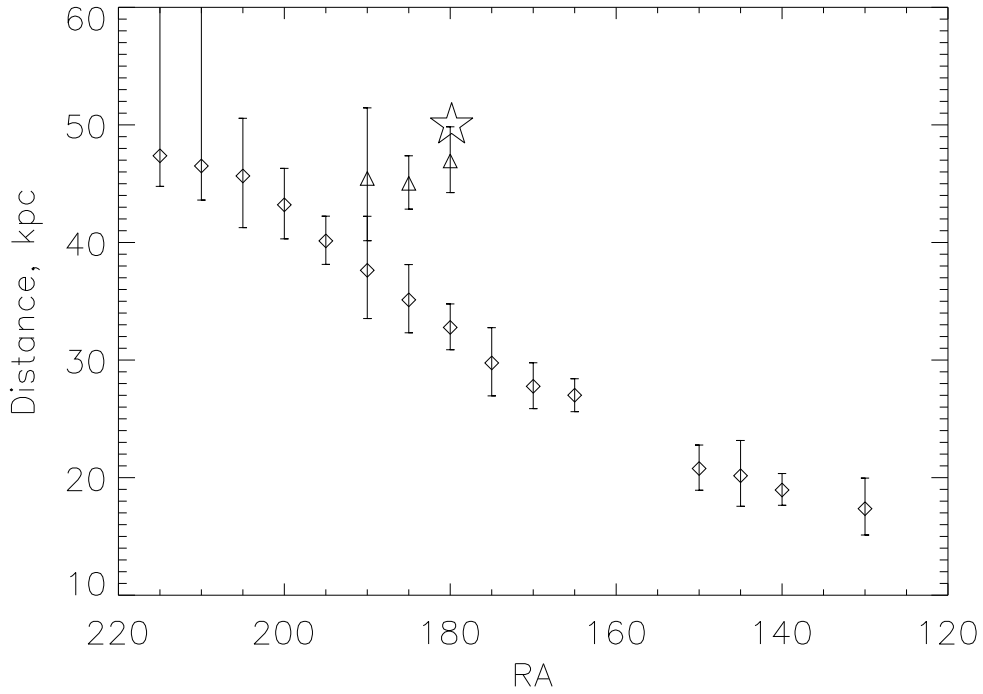

Figure 2.6: Right ascension versus distance for the A and C branches of the Sagittarius Stream (see Belokurov et al., 2006c). The position of Koposov 1 is marked by a star.

Parameter	Koposov 1	Koposov 2
Coordinates (J2000)	11:59:18.5 +12:15:36	07:58:17.00 +26:15:18
Coordinates (ℓ, b)	$(260.98°, 70.75°)$	$(195.11°, 25.55°)$
Distance	$\sim 50\,\mathrm{kpc}$	$\sim 40\,\mathrm{kpc}$
Size	$\sim 3\,\mathrm{pc}$	$\sim 3\,\mathrm{pc}$
M_V	$\sim -2^m$	$\sim -1^m$
Relaxation Time	$\sim 70\,\mathrm{Myrs}$	$\sim 55\,\mathrm{Myrs}$
Tidal radius	$\sim 11\,\mathrm{pc}$	$\sim 9\,\mathrm{pc}$

Table 2.1: Globular cluster parameters

2.4 Discussion

Figure 2.7 shows Koposov 1 and 2 on the size-luminosity plane along with other Galactic globular clusters. This illustrates how unusual Koposov 1 and 2 are in their structural properties. It appears that the detection of these clusters contributes to growing evidence for a large population of small and extremely faint objects (including Palomar 1, AM 4, E3 and Whiting 1). There is a clear indication as well that this sub-population of globulars may have significantly younger ages compared to classical globulars: Palomar 1 (Sarajedini et al., 2007) and Whiting 1 (Carraro et al., 2007) have ages between 4 and 6 Gyrs. The current estimate of age for Koposov 1 is $\approx 8\,\mathrm{Gyrs}$, and the age of E3 globular is $\approx 10\,\mathrm{Gyrs}$. This group of clusters is also quite apparent on the Galactocentric distance versus luminosity plane shown in Figure 2.8). At least 2 out of these 5 unusual clusters (Whiting 1 and Koposov 1) seem to be associated with the Sagittarius dwarf galaxy.

Two quantities that are crucial for the long term evolution and survival of Koposov 1 and 2 are the relaxation time and the expected tidal radius. For the half-mass relaxation time, we find using Eq. 2-63 of Spitzer (1987) or Eq. 72 of Meylan and Heggie (1997),

$$t_{\rm rh} = 0.14 \frac{M_{\rm tot}^{1/2} {R_{\rm hl}}^{3/2}}{\langle m_* \rangle G^{1/2} \ln(\Lambda)} = 70 \text{ and } 55 \text{ Myr}$$

respectively for Koposov 1 and Koposov 2. Here, we have assumed $L \approx 200 L_\odot$, $M/L \approx 1.5$, $\langle m_* \rangle \approx 0.6 M_\odot$ and N= 500 for Koposov 2, whilst for Koposov 1, we have assumed twice as many stars, using the observational estimates of section 2.3. This means that both clusters have extremely short relaxation times, less than 1% of $t_{\rm Hubble}$ and

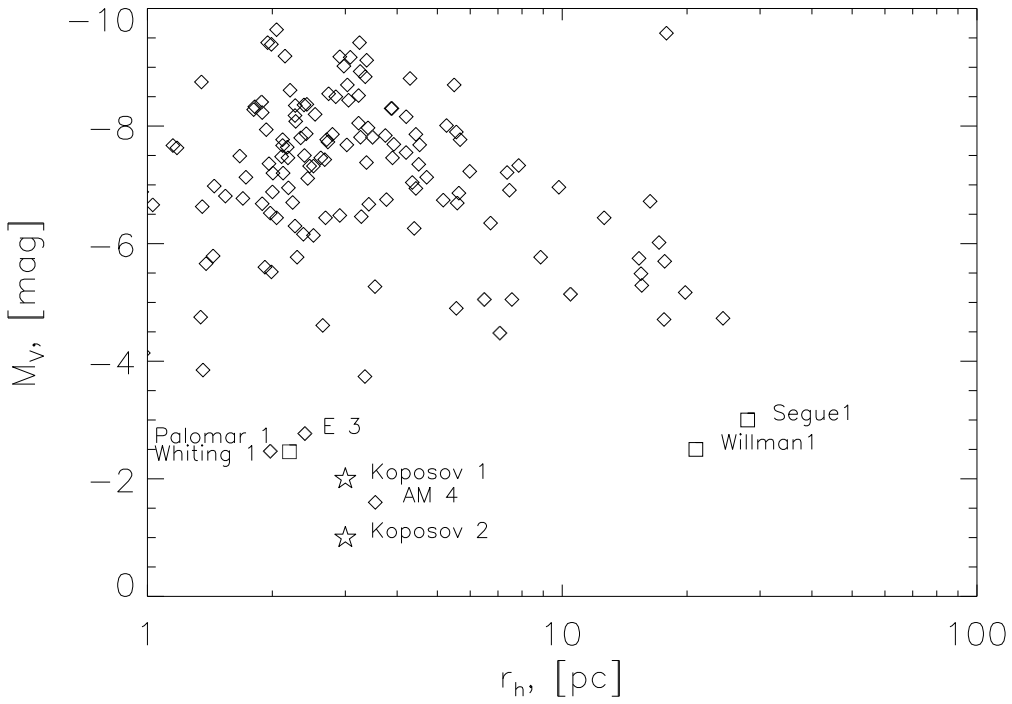

Figure 2.7: The size versus absolute magnitude plot for Galactic globular clusters. The data from the Harris (1996) catalog are plotted with diamonds. Squares mark the locations of the recently discovered globular clusters Willman 1, Segue 1 and Whiting 1. Koposov 1 and 2 are shown as stars.

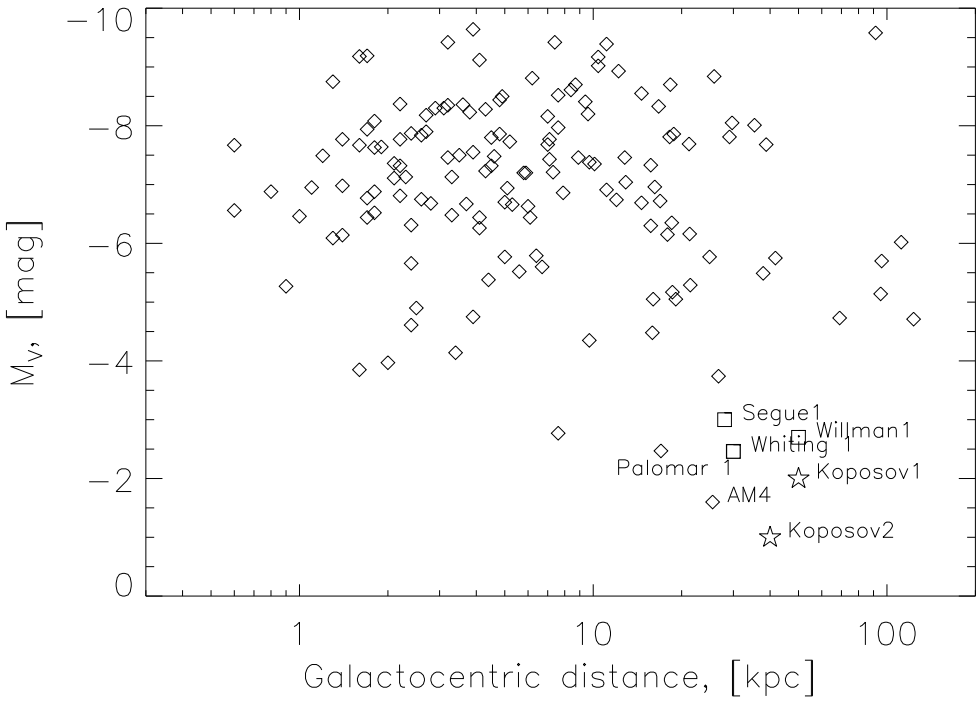

Figure 2.8: The galactocentric distance versus magnitude plot for Galactic globular clusters. The symbols are as in Figure 2.7.

$t_{rh} \approx 0.01 t_{age,*}$. The most immediate effect of two-body relaxation is mass segregation, which should be quite drastic given the apparent stellar population age. The expected tidal truncation of these clusters occurs at (see e.g., Innanen et al., 1983)

$$r_t = 0.43 \left(\frac{M_{\rm cluster}}{M_{\rm MW}} \right)^{1/3} \times R_{\rm peri} = 11 \text{ and } 9 \text{ pc}$$

where we have assumed an orbital eccentricity of 0.5, and that the clusters are now near apocenter (hence $R_{peri} \approx 16\,$kpc), a Milky Way circular speed of 190 km/s at 16 kpc and a cluster (stellar) mass of 600 and 300 $M_\odot$ for Koposov 1 and 2, respectively. Hence, the detectable extent of the globular clusters (3 pc) falls well within the tidal limit. From this argument, the clusters are under no threat of destruction by tidal forces. Although formal profile fits are not feasible with so few stars, the stellar distributions (see Figures 2.1 and 2.4) are well localized, but not centrally concentrated by globular cluster standards; a core to tidal radius ratio of the observed stellar distribution of 4 seems reasonable, implying a concentration parameter of $c \equiv \log(r_t/r_c) \approx 0.5$. For such low concentrations, the evaporation timescale $t_{\rm ev}$, which is the time-scale over which two-body relaxation drives stars to beyond the escape velocity, is $t_{\rm ev} \approx 1.5 t_{\rm cc} \approx 12 t_{\rm rh}$(where $t_{\rm cc}$ is core collapse time) (Figure 17 and 19 in Gnedin et al., 1999)For Koposov 1 and 2, this implies evaporation time-scales of 0.7 Gyrs and 1.1 Gyrs, respectively. This estimate of $t_{ev} \sim 0.1 t_{Hubble}$ may be an underestimate, if the brightest stars which we observe are more concentrated than the faint stars due to mass segregation; then the total mass and half-mass radius can be larger. Nonetheless, this estimate makes it clear that the present structural and dynamical state cannot have prevailed, even approximately, for a time-span of $\sim 10\,$Gyrs. The above arguments hold irrespective of whether Koposov 1 and Koposov 2 were once part of a satellite galaxy, because they are mostly derived from internal evolution factors. This discrepancy of time-scales is more pronounced in Koposov 1 and 2, because their relaxation time-scales are shorter than those of Palomar 1 and Whiting 1, which in any case have accurate photometry suggesting younger ages $\sim 4 - 6\,$Gyr.

At face value, Koposov 1 and 2 have survival times in their current state of $\sim 0.1 t_{\rm Hubble}$, and were found in a search of 20% of the whole sky (SDSS DR5). The naive multiplication of these factors points to a large parent population of ~ 100 objects. The most likely reservoir for this parent population is the globular clusters, and possibly even old open clusters, in satellite galaxies that have been accreted, like the Sagittarius.

In objects like Koposov 1 and 2, it is clear that the very short relaxation and evaporation times must lead to drastic mass segregation and the expulsion of basically all low-mass stars (this line of reasoning lead us to the modest $M/L \approx 1.5$) . This gives new life to the view that truly *many* of the accreted globular clusters must have been destroyed. Yet, it is also clear that the actual dynamical prehistory and future of these clusters requires much more careful modelling. The small number of stars makes them ideal subjects of direct N-body calculations. But regardless of their dynamical evolution, these clusters manifestly demonstrate the parameter space of globular clusters in the Milky Way is not yet fully explored.

3

Constraining the MW potential with a 6-D phase-space map of the GD-1 stream

This chapter reproduces the paper: Koposov, S. E., Rix, H.-W., & Hogg, D. W. 2009 "Constraining the Milky Way potential with a 6-D phase-space map of the GD-1 stellar stream" submitted to ApJ in july 2009, arXiv:0907.1085

3.1 Introduction

The Sloan Digital Sky Survey (SDSS) is an imaging and spectroscopy survey which mapped quarter of the sky near the North Galactic Cap. The data have proven extremely useful for the understanding of the Milky Way halo. In addition to a large list of MW satellites (Belokurov et al., 2007c; Irwin et al., 2007; Koposov et al., 2007b; Walsh et al., 2007) several extended stellar sub-structures in the MW halo have been found in the SDSS data, such as the tidal tail of the Palomar 5 globular cluster (Grillmair and Dionatos, 2006a; Odenkirchen et al., 2001), the Monoceros ring (Newberg et al., 2002), two tidal arms of the disrupting Sagittarius galaxy (Belokurov et al., 2006c), the so called "Orphan" stream (Belokurov et al., 2007b; Grillmair, 2006), the Aquila overdensity (Belokurov et al., 2007a) and the very long thin stellar stream called GD-1 (Grillmair and Dionatos, 2006b). Streams are presumed to be remnants of tidally disrupted satellite galaxies and clusters. They provide important insights into the his-

tory of accretion events and the physics of Galaxy formation. The tidal debris from disrupted satellites (clusters) spreads out in orbital phase on a path that is close to the orbit of the progenitor. Streams tracing out orbits therefore provide opportunities to constrain the Milky Way's gravitational potential.

After initial searches for tidal tails of globular clusters (e.g. Grillmair et al., 1995) it was the extended Sagittarius tidal tail that first made deriving such constraints practical (see e.g. Helmi, 2004; Ibata et al., 2001; Johnston et al., 2005; Law et al., 2005). However, the tidal tail of the Sagittarius galaxy is quite wide and contains a considerable mixture of stellar orbits, making it complex to model. For constraining the gravitational potential, a stellar stream that is very thin but of large angular extent, is ideal, because it permits precise orbital models.

The first studies of globular cluster tidal debris only revealed short ($\lesssim 1^\circ$) signs of tails, but in recent years with the advent of large photometric surveys such as SDSS and 2MASS and significant advances in the techniques used to find streams, significant progress has been made. The matched filter technique (Odenkirchen et al., 2001; Rockosi et al., 2002) has revealed the beautiful tidal stream of Palomar 5. Detailed analysis of the Pal 5 stream, including kinematics (Odenkirchen et al., 2003, 2009, 2001), have shown the promise of this approach, but also revealed that data over more than 10° on the sky are needed to place good constraints on the potential. Grillmair (2006), Grillmair and Dionatos (2006a,b), Grillmair and Johnson (2006) were successful in the detection of very long stellar streams using this technique, including the 63° long stellar stream GD-1 . Besides the stream length and the approximate distance, most of the properties of GD-1 were unknown. Since the stream is long but relatively thin, with no apparent progenitor remnant, it was suggested that it arose from a globular cluster. Here we make an attempt to determine all possible properties of the GD-1 stream including distance, position on the sky, proper motion, and radial velocity and try to constrain the Milky Way potential using that information. This work goes in parallel with the work done by Willett et al. (2009), but we are able to get a full 6-D phase space map of the stream and are able to use that map to provide significant constraints on the MW potential. See also Eyre and Binney (2009) for theoretical discussion of using thin streams in order to constrain the MW potential.

In performing this study we have obtained the first 6-D phase-space map for a kinematically cold stellar stream in the Milky Way. We view our present analysis in

same sense as a pilot study for the GAIA (Perryman et al., 2001) age, when this ESA space mission will deliver dramatically better data on streams such as GD-1.

This chapter is organized as follows: In Section 3.2 we discuss the analysis of the SDSS photometry, which entails mapping the GD-1 stream in 3D as well as determining its stellar population properties. In Section 3.3 we present the kinematics, with proper motions from SDSS/USNO-B1.0 and line-of-sight velocities from SDSS and Calar Alto. In Section 3.4 we combine this information in an iterative step that involves improved stream membership probabilities, which in turn affects the estimates of proper motions and distances. This procedure results in the most comprehensive 6-D data set for a stellar stream in our Milky Way. In Section 3.5 we model the stream data by a simple orbit in a simple parametrized gravitational potential. We measure the potential circular velocity and find that the overall Milky Way potential at the GD-1 stream position is somewhat flattened, but that much of that flattening can be attributed to the disk.

3.2 Stellar population of the stream

The probability that a star is a member of the GD-1 stream depends on its 6-D position and its metallicity. In the space of photometric observables, this means that it depends on (α, δ), magnitude and color. In practice, the determination of the stream's angular position, distance and metallicity (presuming it is 'old') is an iterative process which we detail here.

Grillmair and Dionatos (2006b) made the initial map of the stream using a matched color-magnitude filter based on the CMD of M13 observed in the same filters. Not presuming a particular metallicity (e.g. that of M13), we start our analysis with a simple color-magnitude box selection for stars ($0.15 < g - r < 0.41$ and $18.1 < r < 19.85$). The resulting distribution is shown in Fig. 3.1. That particular color-magnitude box was selected as appropriate to find metal-poor main sequence (MS) stars at a distance of $\sim 10\,\mathrm{kpc}$, and indeed the stream is marginally discernible in the Figure. With just a color-magnitude box, however, the detection fidelity of that stream is noticeably lower than that achieved by Grillmair and Dionatos (2006b)(their Fig. 1). The distribution of stars on Figure 3.1 is plotted in a rotated spherical coordinate system (ϕ_1, ϕ_2), approximately aligned with the stream, where ϕ_1 is longitude and ϕ_2 is the latitude.

The north pole of that coordinate system is located at α_p=34°.5987, δ_p = 29°.7331, the zero-point for ϕ_1 is located at $\alpha = 200°$, and we will use this coordinate system for convenience throughout the chapter to describe stream positions. The transformation matrix from (α, δ) to (ϕ_1, ϕ_2) is :

$$\begin{pmatrix} \cos(\phi_1)\cos(\phi_2) \\ \sin(\phi_1)\cos(\phi_2) \\ \sin(\phi_2) \end{pmatrix} = \begin{pmatrix} -0.4776303088 & -0.1738432154 & 0.8611897727 \\ 0.510844589 & -0.8524449229 & 0.111245042 \\ 0.7147776536 & 0.4930681392 & 0.4959603976 \end{pmatrix} \times \begin{pmatrix} \cos(\alpha)\cos(\delta) \\ \sin(\alpha)\cos(\delta) \\ \sin(\delta) \end{pmatrix}$$

If we integrate the low-contrast 2D map in Fig. 3.1 along the ϕ_1 axis, creating a one-dimensional profile of the stream, the presence of the stream becomes very clear. Figure 3.2 shows this profile for stars with $0.15 < g - r < 0.41$, $18.1 < r < 19.85$ and with $-60° < \phi_1 < -10°$. In that Figure we also overplot the Gaussian fit to this profile with $\sim$ 760 stars and Gaussian width (σ_{ϕ_2}) of $\sim 12'$. This number of stars corresponds to a total stellar mass of $M_* \approx 2 \times 10^4 M_\odot$, if we assume a distance of $\sim$ 10 kpc(see below), and a Chabrier IMF (Chabrier, 2001) with an old, metal-poor stellar population. Given that number of stars, we expect to see around 3000 stream stars in SDSS with r <22.

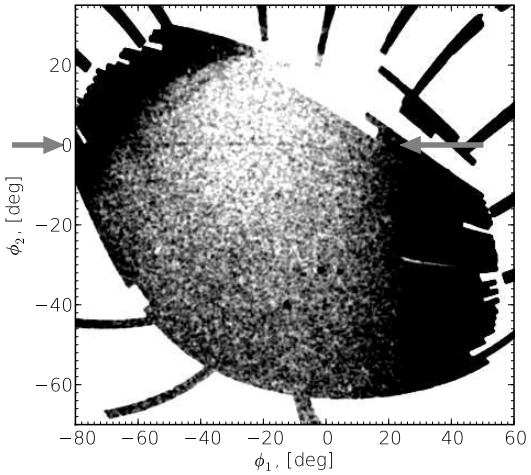

Figure 3.1: The number density of SDSS DR7 stars with $0.15 < g - r < 0.41$ and $18.1 < r < 19.85$, shown in the rotated spherical coordinate system that is approximately aligned with the GD-1 stream. The map was convolved with a circular Gaussian with $\sigma = 0.2°$. The gray arrows point to the stream, which is barely visible in this representation, extending horizontally near $\phi_2 = 0°$, between $\phi_1 = -60°$ and 0°.

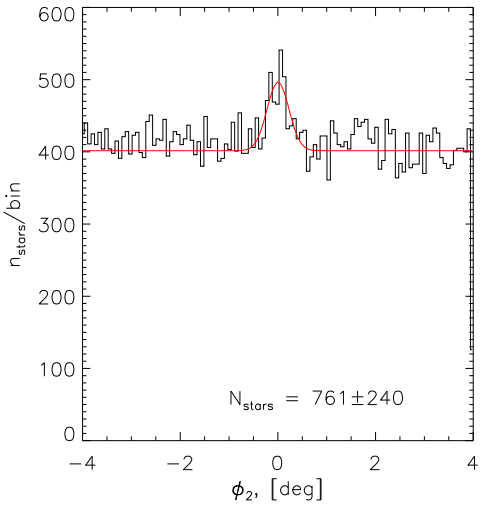

Figure 3.2: One-dimensional stellar density profile across the stream using the stars with $0.15 < g - r < 0.41$ $18.1 < r < 19.85$ across the $\phi_2 = 0°$ axis, integrated along the stream in the interval $-60° < \phi_1 < -10°$. The Gaussian fit with ~ 760 stars and σ=12′ is shown in red.

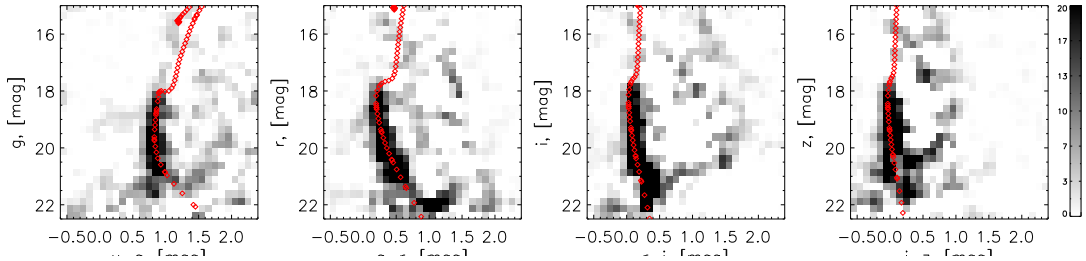

Figure 3.3: Color magnitude (or Hess) diagrams of the stream derived by statistical background subtraction using the Eq. 3.1 fit, in different filters ($u - g$ vs g, $g - r$ vs r, $r - i$ vs i and $i - z$ vs z (from left to right). The grayscale shows the number of stars per rectangular bins. All the magnitudes are extinction corrected. Overplotted are theoretical isochrones for age = 9 Gyrs, $\log(Z/Z_\odot) = -1.4$, distance = 8.5 kpc.

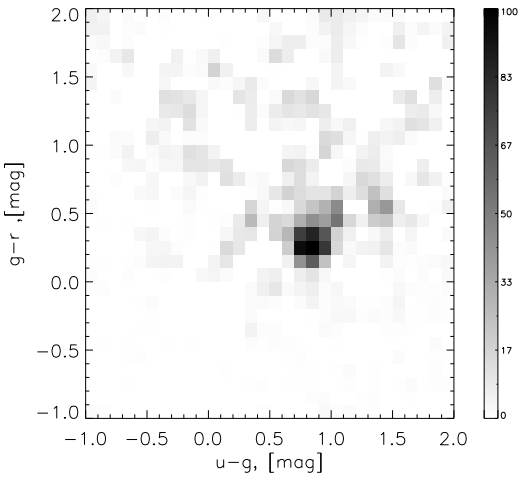

Figure 3.4: $(u-g)-(g-r)$ color-color diagram of the stream, which constitutes a photometric metallicity estimator (following Ivezić et al., 2008, Eq. 4), shown after statistical background subtraction as for Fig. 3.3. All the magnitudes were extinction corrected. The grayscale shows the number of stars per bin, with a distinct concentration of stars at (0.8,0.35), that implies a well defined metallicity [Fe/H] $= -1.9 \pm 0.1$.

We expand this approach to the determination of the CMD of the stream. The data and the fit shown in Figure 3.2 was obtained for a fairly wide color-magnitude selection box. But we can construct such a profile for any other (e.g.) color magnitude box and that profile can then be fitted by

$$N_{obs}(\phi_2|CMD) = N_{BG}(CMD) + N_{stream}(CMD) \times \frac{1}{\sqrt{2\pi}\sigma_{\phi 2}} \exp\left(-0.5\left(\frac{\phi_2-\phi_{2,0}}{\sigma_{\phi 2}}\right)^2\right) \tag{3.1}$$

, where CMD refers to a given color-magnitude bin, and where we assume that both center ($\phi_{2,0}$) and width ($\sigma_{\phi 2}$) of the stream are fixed at 0 and 12 arcminutes. A fit of the Eq. 3.1 model to the observed data $N_{obs}(\phi_2|CMD)$ can be performed in χ^2 sense. As a result $N_{stream}(CMD)$, the number of stream stars (and its error), can be determined for each given color-magnitude bin, resulting in a Hess diagram for each set of filters. Figure 3.3 shows the resulting Hess diagram of the stream derived in several bands. These clearly show a main sequence(MS). The location of the MS turn-off cannot be clearly identified, although there may be a hint at $g = 18.5$, $u-g = 1$. On Figure 3.3 we also overplot the Marigo et al. (2008) isochrones with age$= 9$ Gyrs, $\log(Z/Z_\odot) = -1.4$

at 8.5 kpc, which seem to match quite well. Ivezić et al. (2008) recently showed that the location of MS stars in the $(u-g)-(g-r)$ color-color plane is a good metallicity diagnostic. Therefore, we construct the $(u-g)-(g-r)$ color-color diagram of the stream stellar population shown in Fig. 3.4, which exhibits a distinct concentration of stars at (0.8,0.3). This argues for a population of single or a dominant metallicity and we can convert this color location to a metallicity using Eq. 4 from Ivezić et al. (2008): $[\mathrm{Fe/H}]_{phot} = -1.9 \pm 0.1$. This provides a metallicity estimate that is directly linked to SDSS spectral metallicity estimate.

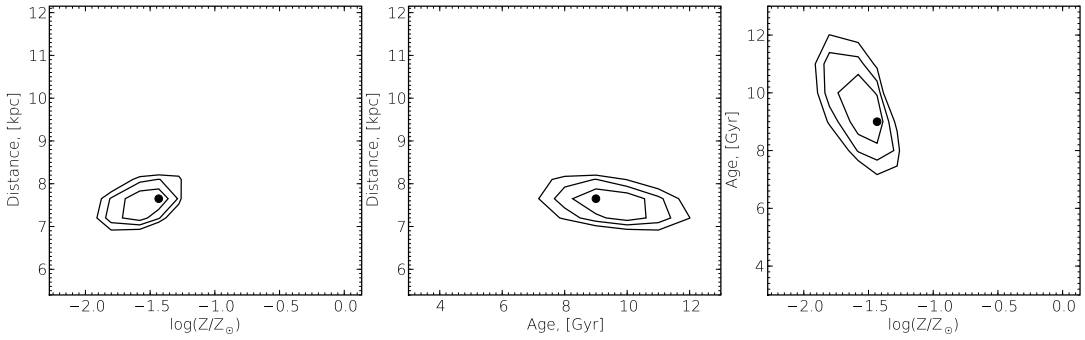

Figure 3.5: Isochrone fits to the color magnitude diagrams (Fig. 3.6) in u, g, r, i, z bands for the stream integrated over $-60° < \phi_1 < -10°$. The contours show the formal 90%, 99%, 99.9% confidence regions as a function of distance, age and metallicity respectively. Filled circles show the location of the best goodness of fit point.

To derive the metallicity, age, and distance of stream stars in a systematic way, we fit the color-magnitude diagrams using a grid of isochrones populated realistically according to the IMF (de Jong et al., 2008; Dolphin, 2002). We focus on fits to the color-magnitude diagrams in u, g and g, r filters, since that the $u-g$ color of the MS turn-off is a good metallicity indicator (Ivezić et al., 2008). We create the synthetic Hess diagrams for a grid of model stellar populations (Girardi et al., 2000; Marigo et al., 2008)[1] with different ages ($3-12$ Gyr), metallicities ($\mathrm{Z} = 0.0001-0.025$), distances ($6-14$ kpc), and a Chabrier IMF (Chabrier, 2001). We then explore that grid by computing log-likelihood of the distribution of stars in color-magnitude space. Figure 3.5 shows the 2D profile likelihoods contours of the age vs metallicity, age vs

[1]To retrieve the isochrones we used the web interface provided by Leo Girardi at the Astronomical Observatory of Padua `http://stev.oapd.inaf.it/cgi-bin/cmd_2.1`

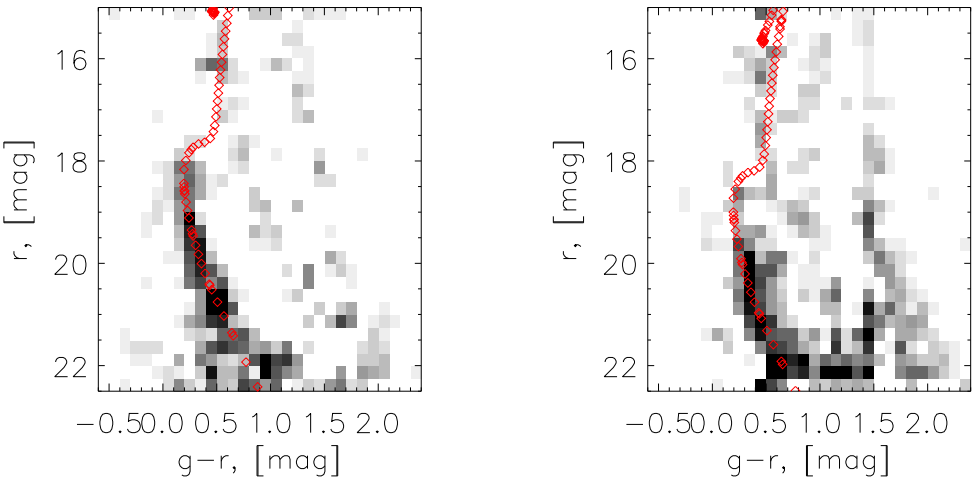

Figure 3.6: Distance variation along the stream. The CMD diagrams of the stream for two different parts of the stream, $-40° < \phi_1 < -20°$ (left), $-10° < \phi_1 < 10°$ (right). The isochrones for the the best fit model $\log(Z/Z_\odot) = -1.4$, age= 9 Gyr were shifted to the distance of 8.5 kpc on the left panel and to 11 kpc on the right panel. Some distance variation apparent, with the stellar population shown on the right located at greater distances.

distance and distance vs metallicity planes. The filled circle indicates the best fit model: age= 9 Gyrs, $\log(Z/Z_\odot) = -1.4$ and distance= 8 kpc. Clearly the age is the least well constrained parameter; the distance seems to be relatively well constrained, but has a covariance with [Fe/H]. We will revisit this issue later, as the analysis of Fig. 3.4 implies a lower metallicity. Fig. 3.3 shows that the isochrones are reproducing the observed Hess diagrams well, and hence further we will use t= 9 Gyrs, $\log(Z/Z_\odot) = -1.4$ as the baseline model for the stream's stellar population. It should be noted that the distance measurement from Fig. 3.5 represents the averaged distance along the stream from $-50° < \phi_1 < -20°$. In section 3.4 we will present estimates of the distance to different parts of the stream.

It is noticeable that the metallicity derived from the CMD fitting is higher than from the estimate based on empirical calibration of Ivezić et al. (2008)(see above) and higher than the measurement based on the SDSS spectra given by Willett et al. (2009). This discrepancy is understandable given the known inaccuracies of the isochrones in the SDSS photometric system (An et al., 2008). In particular the Figure 19 of An et al. (2008) paper clearly shows a mismatch between fiducial isochrone derived for the M92

globular cluster (which is used elsewhere as a good approximation of old metal-poor stars in the halo) and the theoretical isochrones. For main sequence stars below the turn-off (which are of the most interest here), the mismatch can be approximated by a distance shift of $\sim 10\%$. Therefore in our analysis we reduce all the distances derived on the basis of the CMD fit by 10%.

Splitting the CMD data into ϕ_1 bins shows that there is a distance gradient along the stream: Figure 3.6 shows two Hess diagrams obtained for two different pieces of the stream, on the left $-40^\circ < \phi_1 < -20^\circ$, and on the right -10° $< \phi_1 <$ 10°. The baseline isochrone is shifted to distances of 8.5 kpc(left) and 11 kpc(right) respectively. Clearly, the part of the stream at $-10^\circ < \phi_1 < 10^\circ$ is further from the Sun, (as already noted by Grillmair and Dionatos, 2006b; Willett et al., 2009).

The determination of the CMD properties for the stream allows us to select the possible stream member stars with much less background contamination, compared to a simple color magnitude box. Figure 3.7 shows the map of the stream (in ϕ_1, ϕ_2 coordinates) after applying a matched filter based on the CMD of the stream. For Fig. 3.7 each star in the SDSS dataset was weighted by the ratio of the stream membership probability and the background probability $\frac{P_{stream}(u-g,g-r,r-i,r)}{P_{BG}(u-g,g-r,r-i,r)}$,where $P_{stream}(u-g, g-r, r-i, r)$ have been computed based on the stellar population fit (Fig. 3.5), and $P_{BG}(u-g, g-r, r-i, r)$ was computed empirically from the regions adjacent to the stream (see e.g. Rockosi et al., 2002, for the application of similar method). The resulting image after the CMD weighting shows the stream with obviously greater contrast than Figure 3.1.

3.3 Kinematics

In this section we describe how we derived estimates of the 3D kinematics of the stream by looking at the proper motions and radial velocities of the probable stream members.

3.3.1 Proper motion

Despite the distance of ~ 10 kpc to the GD-1 we demonstrate in this section that it is possible to derive good constraints on its proper motion. The analysis is based on proper motions derived from combining USNO-B1.0 (Monet et al., 2003) with SDSS data (Munn et al., 2004, 2008), which we take from SDSS DR7 (Abazajian et al., 2009).

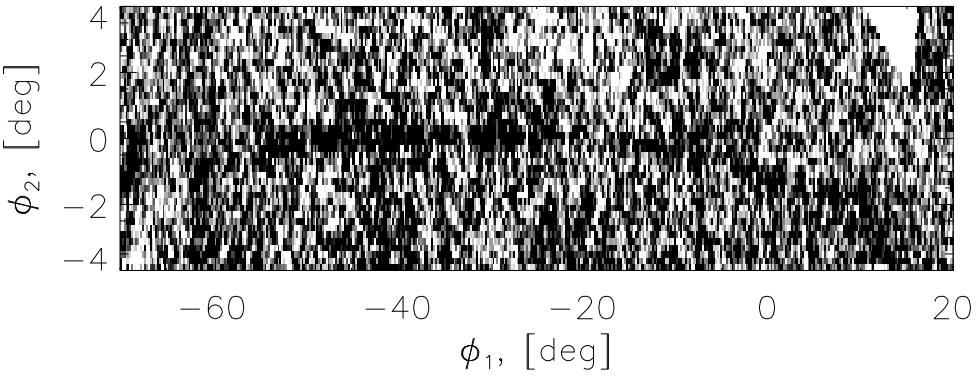

Figure 3.7: Map of stream stars in the rotated coordinate system after applying the matched CMD filter from Section 3.2. The figure shows the histogram of stars in ϕ_1, ϕ_2, where each star has been weighted by the CMD weight $\frac{P_{stream}(u-g,g-r,r-i,r)}{P_{BG}(u-g,g-r,r-i,r)}$

At a distance of $\sim 10\,\mathrm{kpc}$ a stream that is moving transversely at approximately constant distance from us, should have a proper motion in the order $\sim 4\,\mathrm{mas/yr}$ (where $200\,\mathrm{km/s}$ was taken as a characteristic velocity in the halo). Hence the expected proper motion is comparable to the precision of individual proper motion measurements. As stream member stars that are adjacent on the sky should have (nearly) identical proper motions, we can, however, determine statistical proper motions for ensembles of stars.

We start by deriving the $\vec{\mu}$-distribution of likely member stars, by extending the analysis of Section 3.2 and using both the angular position on the sky (specifically ϕ_2) and the location in CMDs for each star to evaluate its stream membership probability. Specifically, we determine for each proper motion 'pixel' $(\vec{\mu}, \vec{\delta\mu})$ $N_{stream}(\vec{\mu}|\phi_2, CMD)$ (number of stream stars) by integrating along the stream direction ϕ_1 and fitting the ϕ_2 distribution with the Eq. 3.1 for the stars with high membership probabilities in the CMD (u-g,g-r,r-i,i) space $P_{stream}/P_{BG} \gtrsim 0.1$. The resulting distribution $N_{obs}(\vec{\mu})$ is shown in Fig. 3.8. The grayscale in the left panel of the Figure shows the proper motion distribution of μ_α, μ_δ of probable stream member stars (N_{stream}) integrated along the stream, while the contours show the proper motion distribution of the background stars selected with the same color-magnitude criteria (corresponding to N_{BG} from Eq. 3.1). It is clear that the stream stars are on average moving differently than the bulk of background stars. However, the observed proper motions contain the reflex motion of

Sun's motion in the Galaxy. We can account for this and then convert $\vec{\mu}$ to $(\mu_{\phi_1}, \mu_{\phi_2})$, the proper motion along the stream $\mu_{\phi_1} \equiv \mu_{along}$ and proper motion across the stream μ_{ϕ_2} in the Galactic rest-frame (where ϕ_1, ϕ_2 are the stream coordinates introduced in Section 3.2). The proper motion component arising from the Sun's movement in the Galaxy can be easily computed for each star.

$$\vec{\mu}_{reflex} = \frac{1}{4.74\,|\vec{r}|}(\vec{V}_\odot - (\vec{V}_\odot \cdot \vec{r})\frac{\vec{r}}{|\vec{r}|^2})$$

where $\vec{V}$ is a 3D velocity of the sun ($\sim 220\,\mathrm{km/s}$) and $\vec{r}$ is the vector from the sun towards each star. As we approximately know the distance to the stream, this correction $\mu_{\phi_{1,2},c} = \mu_{\alpha,\delta} - \mu_{reflex}$ can be done. We will discuss the consequences of the uncertainties in the Sun's motion and the stream differences in Section 3.4.

The right panel of Fig. 3.8 shows the distribution of $\mu_{\phi_1}, \mu_{\phi_2}$ of the stream stars. The contours show the corresponding distribution of background stars with the similar color-magnitudes to the stream stars. Reassuringly we see that stream stars are moving approximately along ϕ_1, i.e. along the stream orbit, an important plausibility check for the correctness of the proper motion measurement. In contrast, the proper motion distribution of the background stars after subtracting the proper motion due to sun's movement is centered around $(\mu_{\phi_1}, \mu_{\phi_2}) = (0, 0)$, which appears reasonable since with our color-magnitude selection we are selecting primarily the halo stars at distances $\sim 10\,\mathrm{kpc}$. Those show little net rotation (Carollo et al., 2007; Xue et al., 2008). The estimate $\langle \mu_{\phi_1} \rangle \approx -8\,\mathrm{mas/yr}$ also immediately implies that the stream is going retrograde with respect to the Milky Way's disk rotation.

In Figure 3.9 we illustrate the proper motion variation along the stream. These plots, showing only $\mu_{\phi_1}(\phi_1)$ were derived the same way as Fig. 3.8, except that we did not integrate in ϕ_1 along the entire stream but only in ϕ_1 intervals. The left panel of Fig. 3.9 shows the distribution of the proper motions along the stream of the background stars. The right panel of the Figure shows the distribution of proper motions of likely stream member stars as a function of angle along the stream (the proper motion due to the Sun's motion was subtracted). The right panel reveals a slight, but significant gradient in $\langle \mu_{\phi_1} \rangle$, of the order of 3 to 5 mas/yr. Note that the decrease of the proper motions towards $\phi_1 = 0$ coincides with the distance increase to the stream (see Fig. 3.6).

Having determined the stream proper motions, we can further improve the CMD-filtered map of the GD-1 stream (Fig. 3.7) by requiring that the proper motions of the

stars are consistent with the proper motion of the stream. That is shown in Fig. 3.10. and discussed in Section 3.3.2.

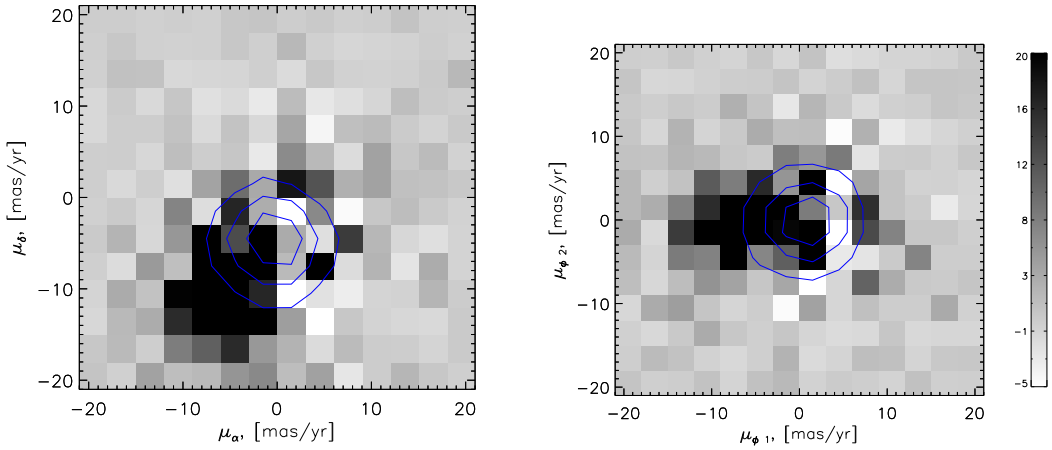

Figure 3.8: Proper motion of the stream. The left panel shows the proper motion in right ascension and declination μ_α, μ_δ (as observed, e.g. no correction for the Solar motion in the Galaxy was made). The right panel shows the proper motion in the rotated coordinate system (ϕ_1, ϕ_2) (ϕ_1 is oriented along the stream) and after the subtraction of the proper motion due to the Sun's motion in the Galaxy (assuming for now $V_c = 220\,\mathrm{km/s}$). The grayscale in each of the panels shows the number of stars per proper motion bin. Contours shows the the proper motion distribution for the field stars. with similar colors and magnitudes to the stream stars. The proper motions of the stream stars are clearly distinguishable from the proper motions of the background stars. The right panel confirms the fact that the stream stars are moving approximately along its orbit ($\mu_{\phi_2} \approx 0\,\mathrm{mas/yr}$), while the mean proper motions of background stars after subtracting Sun's motion are consistent with zero.

3.3.2 Radial velocities

To construct the 6-D phase space distribution of the stream, the radial velocities are the remaining datum. By necessity the actual sample for which spectra, and hence radial velocities, will be available, will differ from the photometric sample just described. In this section we will use both the data from the SDSS/SEGUE survey (Yanny et al., 2009) as well as radial velocities obtained by us with the TWIN spectrograph on Calar Alto, specifically targeting likely stream member stars.

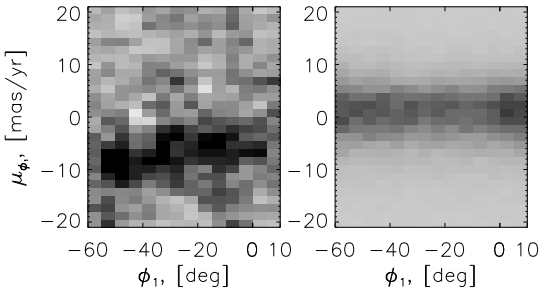

Figure 3.9: Variation of the proper motions along the stream (corrected for the Solar reflex motion, assuming $V_0 = 220\,\mathrm{km/s}$). The left panel shows the distribution of μ_{ϕ_1} for the stream candidate stars as a function of ϕ_1. The right panel shows the distribution of μ_{ϕ_1} of the field stars selected using the same color-magnitude criteria as the stream stars. The variation of proper motions of stream stars with ϕ_1 is clearly visible in the left panel. Near $\phi_1 \sim 0°$ the proper motion of the stream is around $-5\,\mathrm{mas/yr}$, while at $\phi_1 \sim -50°$ it is around $-8\,\mathrm{mas/yr}$.

3.3.2.1 SDSS radial velocities

SEGUE and SDSS only provide sparse spatial sampling of high latitude stars. SEGUE did not target any GD-1 member stars specifically. Therefore we have to search through the existing SEGUE spectra to identify likely, or possible, member stars by position on the sky, CMD position and proper motion. In the previous section we described that we used the ratio of the stream/background probabilities $\frac{P_{stream}(u-g,g-r,r-i,r)}{P_{BG}(u-g,g-r,r-i,r)}$ to select high probability members of the stream. Now additionally to that we also select the stars within the μ_α, μ_δ box (see Fig. 3.8). That allows us to have a sample of stream stars with much less background contamination, although the overall size of that sample is significantly smaller, since the the SDSS/USNO-B1.0 measurements of the proper motions were done for stars with $r \lesssim 20$ (Munn et al., 2004). To illustrate how good the proper motion selection is when combined with the color-magnitude selection we show map of high probability stream member stars on Figure 3.10. The stream is now clearly seen in individual stars. In Figure 3.10 we also overplot the location of existing SEGUE DR7 pointings, some of which cover the stream. Therefore we may expect to find some stream members among the SEGUE targets in these fields.

Figure 3.11 shows the SDSS/SEGUE radial velocity distribution as a function of ϕ_1 for those stars whose proper motions and color-magnitude position are consistent with stream membership, and which are located within 3 degrees from the center of the

stream. The filled red circles in this Figure show the subset of stars located within 0°.3 from the center of the stream and therefore represent the subset with very high membership probability, while the open black circles represent(spatially selected, $|\phi_2| > 0.3°$) background stars with similar proper motion and color magnitude. The filled symbols in Fig. 3.11 clearly delineate the radial velocity of the stream. Clumps of red circles are visible at (ϕ_1, V_{rad})≈(-25°,-100 km/s), (-30°,-80 km/s), (-47°,0 km/s), (-55°,40 km/s). In order to perform the formal measurements of the radial velocities we performed a maximum likelihood fit by a model, consisting from two Gaussians one (wide) Gaussian was representing the background distribution, while the second (narrow) was modeling velocity distribution of stream stars. This fit gave us the following results: (ϕ_1, V_{rad})=(-56°,39±14 km/s), (-47°,-7±10 km/s), (-28°,-61±6 km/s), (-24°, -83±9 km/s).

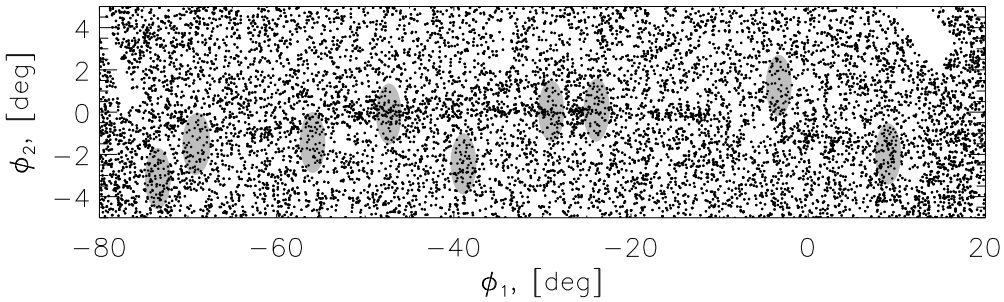

Figure 3.10: Stars that match the expectations for stream members with regards to proper motions, colors and magnitudes (but no ϕ_2 filter), used in the candidate selection for radial velocity measurements. The stream can be clearly seen in distribution of individual stars. The locations of the SEGUE DR7 pointings are shown by gray circles.

3.3.2.2 Calar Alto radial velocities

Since the SDSS/SEGUE radial velocities only provide constraints at a few points of the stream, we decided to obtain additional radial velocity information with targeted observations. We based the target selection for likely stream members on all the available information discussed in the previous sections: position on the sky, color-magnitude location and proper motions. We selected 34 stars likely members with r $\lesssim$ 19 for the observations. All these stars are within the sample plotted in the Figure 3.10.

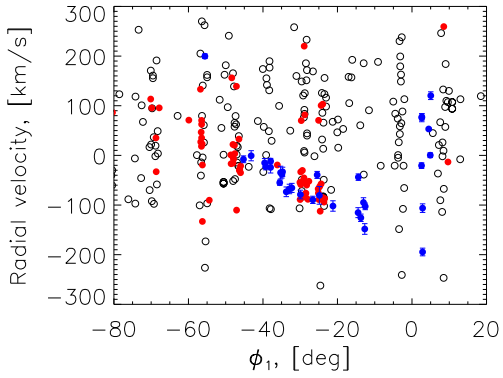

Figure 3.11: Radial velocities of likely stream stars (filled circles). The Figure shows the radial velocities drawn from the SDSS/SEGUE (red circles) and Calar Alto spectra (blue circles). The red and blue symbols reflect the radial velocities of all stars matching in color, magnitude and proper motion that have positions with $|\phi_2| < 0.3°$. The open circles represent SDSS/SEGUE velocities of similar stars but with $|\phi_2| > 0.3°$. The radial component of the Solar reflex motion (taking $V_0 = 220\,\mathrm{km/s}$) was subtracted from all datapoints.

The observations were performed the TWIN spectrograph on the 3.5m telescope at Calar Alto observatory, during several nights of service observing in February 2009. We used the blue and red arms of the spectrograph at a resolution of 4000-5000 to observe the H_β, Mgb lines and CaII near-IR triplet respectively. The standard data reduction steps were applied to the dataset using custom written routines in Python language.

We used both the blue and the red spectra to compute the radial velocity of each star. The radial velocity of each star was derived by minimizing χ^2 as a function of velocity shift of the template convolved with the appropriate Line Spread Function (LSF). The χ^2 for each star was a sum of the χ^2 for the blue and the red part of the spectra. As template in the blue spectral range we used the spectra from the ELODIE database (Prugniel et al., 2007) for stars of similar color and magnitude to the targeted ones and with low metallicity [Fe/H] ~ -2. In the red spectral range the template spectra was simply consisting from three lines of Ca triplet at 8498.02Å 8542.09Å and 8662.14Å. The error of each velocity measurement was determined using the condition $\Delta(\chi^2(V)) = 1$.

The Calar Alto measurements of the velocities together with their errors are over-plotted in blue symbols in Fig. 3.11. It is apparent from Fig. 3.11 that for $-50° < \phi_1 <$

-10° the targeting strategy was very successful, nicely delineating the projected velocity gradient along the stream. Overall out of 34 observed stars ~ 24 stars belong to the stream and ~ 5 didn't have enough S/N for the velocity determination. Unfortunately the targeting near $\phi_1 \approx +5^\circ$ failed to identify stream members, probably because the stream there is less intense and further away.

3.4 Modeling

In the previous section we described the derivation of different stream properties such as distance, position on the sky, proper motion separately. In this Section we will map the stream in 6-D position-velocity space in a more consistent way, using all the available information (see e.g. Cole et al., 2008, for the application of similar, although simpler method to Sgr stream). This will provide us with a set of orbit constraints along different sections of the GD-1 stream, which we will then model by an orbit to derive potential constraints.

3.4.1 Positions on the sky and distances to the stream

We start by characterizing the projected stream position and its distance from the Sun through a maximum likelihood estimate for a parametrized model of the stream $P_{stream}(r, g-r, \phi_1, \phi_2)$ that describes it in 4-dimensional space of photometric observables r,$g-r$,ϕ_1,ϕ_2:

$$P_{stream}(r, g-r, \phi_1, \phi_2) = \mathrm{CMD}(r, g-r, D(\phi_1)) \times \\ \times I(\phi_1) \times \frac{1}{\sqrt{2\,\pi}\sigma_{\phi_2}(\phi_1)} \exp\left(-\frac{(\phi_2 - \phi_{2,0}(\phi_1))^2}{2\,\sigma^2_{\phi_2}(\phi_1)}\right) \tag{3.2}$$

Here $\phi_{2,0}(\phi_1)$ is the ϕ_2 position of the stream center on the sky as a function of ϕ_1, $\sigma_{\phi_2}(\phi_1)$ is the projected width of the stream in ϕ_2, $I(\phi_1)$ is the "intensity" (i.e. the number density) of the stream as a function of ϕ_1, and $D(\phi_1)$ is the distance to the stream. Further, $CMD(r, g-r, D(\phi_1))$ is the normalized Hess diagram (i.e. the probability distribution in CMD space) expected for the stream's stellar population at a distance of $D(\phi_1)$ after accounting for the observational errors. We construct that CMD based on the age and metallicity obtained in Section 3.2 and the isochrones from Girardi et al.

(2000); Marigo et al. (2008) (assuming that $\frac{d[Fe/H]}{d\phi_1}$=0 and $\frac{d(age)}{d\phi_1}$=0). In this model, P_{stream} depends on four functions – $I(\phi_1)$, $\phi_{2,0}(\phi_1)$, $\sigma_{\phi_2}(\phi_1)$, $D(\phi_1)$ – which we take to be piecewise constant; i.e. for intervals $\delta\phi_1$ they simply become four parameters.

For the field stars, $P_{BG}(r, g-r, \phi_1, \phi_2)$ the analogous 4D distribution is

$$P_{BG}(r, g-r, \phi_1, \phi_2) = I_{BG}(\phi_1, \phi_2) \times CMD_{BG}(r, g-r, \phi_1)$$

, where $I_{BG}(\phi_1, \phi_2)$ is the 2D number density distribution of the field stars around the stream and $CMD_{BG}(r, g-r, \phi_1)$ the corresponding color-magnitude diagram. These functions are determined empirically from the data in adjacent parts of the sky ($|\phi_2| \gtrsim 0.5^\circ$). $I_{BG}(\phi_1, \phi_2)$ is determined by fitting the density of the stars in the ϕ_1, ϕ_2 space by a polynomial. $CMD_{BG}(r, g-r, \phi_1)$ is determined by constructing the Hess diagrams using all the stars with $0.3^\circ < |\phi_2| < 5^\circ$ in several ϕ_1 bins.

To simplify the determination of $P_{BG}(r, g-r, \phi_1, \phi_2)$ and $P_{stream}(r, g-r, \phi_1, \phi_2)$, we split the stream in several ϕ_1 pieces, and consider $I(\phi_1)$, σ_{ϕ_2}, $D(\phi_1)$ and $\phi_{2,0}(\phi_1)$ as constants within them. The log-likelihood for the mixture of the P_{stream} and P_{BG} distribution can be written as (here for convenience we introduce α as a fraction of stream stars instead of $I(\phi_1)$):

$$\ln(\mathcal{L}) = \sum_{stars} 2\ln(\alpha\, P_{stream}(r_i, g_i - r_i, \phi_{1,i}, \phi_{2,i}) + (1-\alpha) P_{BG}(r_i, g_i - r_i, \phi_{1,i}, \phi_{2,i})) \tag{3.3}$$

and should be maximized with respect to the parameters (σ_{ϕ_2}, $D(\phi_1)$, $\phi_{2,0}(\phi_1)$ and α). The maximization is performed using the Truncated Newton method(Nash, 1984). The parameter errors are obtained by using the $\delta(\ln(\mathcal{L}))$ criteria (e.g. Cash, 1979).

The left and central panels of Figure 3.12 show the resulting estimates of the projected position and the distance of the stream, the parameters used in the subsequent orbit fitting. We do not use the number density of stream stars, as it varies noticeably along the stream (see Fig. 3.7) and the reason of these variations is not clear. It is apparent from Fig. 3.10 that the projected stream position is very well defined, and that a distance gradient exists along the stream.

3.4.2 Proper motions

The likelihood maximization just described also results in stream membership probabilities for any given star i, $P_{stream}(r_i, g_i - r_i, \phi_{1,i}, \phi_{2,i})$. This information can then be used to estimate via maximum likelihood the mean proper motions of different stream pieces, thereby extending the observational estimates to the full 6-D space (r,$g-r$,ϕ_1,ϕ_2,μ_{ϕ_1},μ_{ϕ_2}).

$$P_{stream,\mu}(r, g-r, \phi_1, \phi_2, \mu_{\phi_1}, \mu_{\phi_2}) = P_{stream}(r, g-r, \phi_1, \phi_2) \times \frac{1}{2\,\pi\,\sigma_\mu^2} \times \exp\left(-\frac{(\mu_{\phi_1} - \mu_{\phi_1,0}(\phi_1))^2 + (\mu_{\phi_2} - \mu_{\phi_2,0}(\phi_1))^2}{2\,\sigma_\mu^2}\right) \tag{3.4}$$

where we simply take the previously determined P_{stream} as a prior, to be modified by the Gaussian distribution in the 2D proper motions space. Here, the proper motion distribution is characterized by three functions, $\mu_{\phi_1,0}(\phi_1)$, $\mu_{\phi_2,0}(\phi_1)$ and σ_μ, which again we take to be piecewise constant. The distribution of the background stars in the 6-D space $P_{BG,\mu}(r, g-r, \phi_1, \phi_2, \mu_{\phi_1}, \mu_{\phi_2})$ is obtained empirically by binning the observational data. Then we construct again the logarithm of likelihood, considering variations in four parameters: the number of stream stars, the proper motion of the stream in ϕ_1 and ϕ_2 and the proper motion spread σ_μ. This likelihood is then maximized and we determine the μ_{ϕ_1}, μ_{ϕ_2} and σ_μ for different stream pieces. The right panel of the Figure 3.12 shows the resulting proper motion estimates as a function of ϕ_1. These proper motions have not been corrected here for the Sun's reflex motion, which we will model in Section 3.5.

Overall, the analysis presented in the previous sections has resulted in the best and most extensive set of 6-D phase-space coordinate map for a cold stream of stars in the Milky Way.

3.5 Orbit fitting

If we can assume that all the stream stars lie close to one single test-particle orbit, then our phase space map of the GD-1 stream should not only define this orbit, but at the same time constrain the Milky Way's potential. The assumption that the stream stars

Star	ϕ_1	ϕ_2	V_{rad}
	deg	deg	km/s
SDSS J094105.35+315111.6	−45.23	−0.04	28.8 ± 6.9
SDSS J094705.26+332939.8	−43.17	−0.09	29.3 ± 10.2
SDSS J095740.48+362333.0	−39.54	−0.07	2.9 ± 8.7
SDSS J095910.43+363206.6	−39.25	−0.22	-5.2 ± 6.5
SDSS J100222.01+374113.3	−37.95	0.00	1.1 ± 5.6
SDSS J100222.02+374049.2	−37.96	−0.00	-11.7 ± 11.2
SDSS J101033.02+393300.8	−35.49	−0.05	-50.4 ± 5.2
SDSS J101110.08+394453.9	−35.27	−0.02	-30.9 ± 12.8
SDSS J101254.83+395525.6	−34.92	−0.15	-35.3 ± 7.5
SDSS J101312.05+400613.3	−34.74	−0.08	-30.9 ± 9.2
SDSS J101702.15+404747.3	−33.74	−0.18	-74.3 ± 9.8
SDSS J101951.76+412701.5	−32.90	−0.15	-71.5 ± 9.6
SDSS J102216.20+415534.7	−32.25	−0.17	-71.5 ± 9.2
SDSS J103003.87+434351.7	−29.95	−0.00	-92.7 ± 8.7
SDSS J104341.92+460224.7	−26.61	−0.11	-114.2 ± 7.3
SDSS J104840.98+464922.1	−25.45	−0.14	-67.8 ± 7.1
SDSS J105036.96+472000.1	−24.86	0.01	-111.2 ± 17.8
SDSS J110711.27+494415.9	−21.21	−0.02	-144.4 ± 10.5
SDSS J114242.08+533841.4	−14.47	−0.15	-179.0 ± 10.0
SDSS J114724.59+535546.8	−13.73	−0.28	-191.4 ± 7.5
SDSS J115116.08+542142.7	−13.02	−0.21	-162.9 ± 9.6
SDSS J115326.06+542930.6	−12.68	−0.26	-217.2 ± 10.7
SDSS J115404.06+543511.4	−12.55	−0.23	-172.2 ± 6.6

Table 3.1: Radial velocities from the Calar Alto observations

ϕ_1	ϕ_2
deg	deg
-60.00	-0.64 ± 0.15
-56.00	-0.89 ± 0.27
-54.00	-0.45 ± 0.15
-48.00	-0.08 ± 0.13
-44.00	0.01 ± 0.14
-40.00	-0.00 ± 0.09
-36.00	0.04 ± 0.10
-34.00	0.06 ± 0.13
-32.00	0.04 ± 0.06
-30.00	0.08 ± 0.10
-28.00	0.03 ± 0.12
-24.00	0.06 ± 0.05
-22.00	0.06 ± 0.13
-18.00	-0.05 ± 0.11
-12.00	-0.29 ± 0.16
-2.00	-0.87 ± 0.07

Table 3.2: Stream positions

ϕ_1	**Distance**
deg	kpc
-55.00	7.20 ± 0.30
-45.00	7.59 ± 0.40
-35.00	7.83 ± 0.30
-25.00	8.69 ± 0.40
-15.00	8.91 ± 0.40
0.00	9.86 ± 0.50

Table 3.3: Stream distances

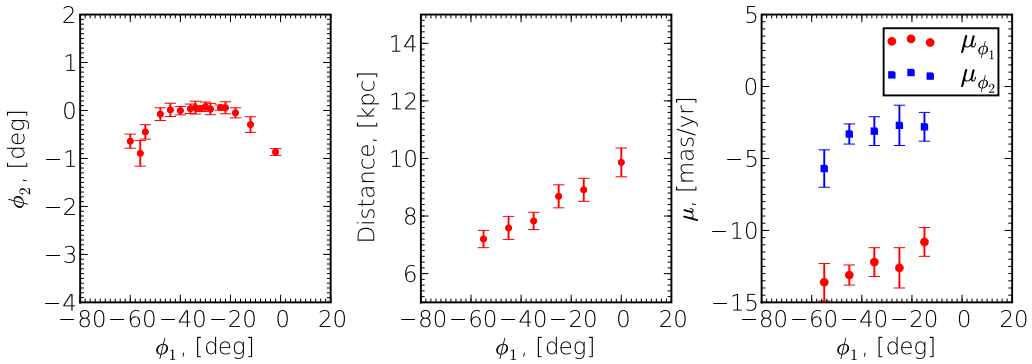

Figure 3.12: Summary of photometrically derived stream properties based on maximum likelihood fits to chunks of the stream, drawing on SDSS photometry and astrometry (see Section 3.4). The left panel shows the positions of the stream on the sky in ϕ_1,ϕ_2 coordinates. The middle panel show the measurements of the distances as a function of ϕ_1. The right panel shows the statistical proper motions of the stream stars (without the correction for the Solar motion); red circles show the μ_{ϕ_1} (the proper motion along the stream), blue squares show the μ_{ϕ_2} (the proper motion perpendicular to the stream).

ϕ_1	μ_{ϕ_1}	μ_{ϕ_2}	σ_μ
deg	mas/yr	mas/yr	mas/yr
−55.00	−13.6	−5.7	1.3
−45.00	−13.1	−3.3	0.7
−35.00	−12.2	−3.1	1.0
−25.00	−12.6	−2.7	1.4
−15.00	−10.8	−2.8	1.0

Table 3.4: Stream proper motions

are moving along the same orbit is plausible , especially if the stream is near pericenter (Dehnen et al., 2004, & private communication) . But it is not straightforward to quantify the quality of such an approximation. For now we simply fit an orbit to our 6-D map of available observational data: the position on the sky, $\phi_2(\phi_1)$, proper motion $\vec{\mu}(\phi_1)$, distance to the stream $D(\phi_1)$ and radial velocity $V_{rad}(\phi_1)$. For each assumed potential, we will determine the best fit orbit, but then marginalize over the orbits to determine the range of viable gravitational potentials. This analysis extends earlier efforts by Grillmair and Dionatos (2006b) and Willett et al. (2009) who have presented orbit solutions for GD-1 . However, we can now draw on a much more extensive set of observational constraints. We also explore the fit degeneracies. Given that our 6-D phase-space map of the GD-1 stream spans only a limited range in R and z (as seen from the Galactic center), it proved useful to consider very simple parametrized potentials at first. Further it proved necessary to consider what prior information we have on the Sun's (i.e. the observers) position and motion, as well as on our Milky Way's stellar disk mass.

3.5.1 One component potential

The stream is located at Galactocentric $(R, z) \approx (12, 6)$ kpc, a regime where presumably both the stellar disk and the dark halo contribute to the potential , and its flattening. Of course, the stream dynamics are solely determined by the total potential, and therefore we consider first a simple single-component potential, the flattened logarithmic potential

$$\Phi(x, y, z) = \frac{V_c^2}{2} \ln\left(x^2 + y^2 + \left(\frac{z}{q_\Phi}\right)^2\right), \tag{3.5}$$

which has only two parameters: the circular velocity V_c and the flattening q_Φ. Note that $(1 - q_{density}) \approx 3(1 - q_\Phi)$ for moderate flattening (e.g. p.48 of Binney and Tremaine, 1987). Such a simple potential seems justified as the stream stars are only probing a relatively small range in R and z.

In practice, we fit an orbit to the 6-D stream map by considering a set of trial starting points in the Galaxy, specified by the initial conditions $(\vec{X}(0), \dot{\vec{X}}(0))$ in standard Cartesian Galactic coordinates. Together with an assumed gravitational potential this predicts $(\vec{X}(t), \dot{\vec{X}}(t))$, which can be converted to the observables, $\phi_2(\phi_1)$, $\vec{\mu}(\phi_1)$, $D(\phi_1)$, $V_{rad}(\phi_1)$ and then compared to the 6-D observations (Fig. 3.13). For each

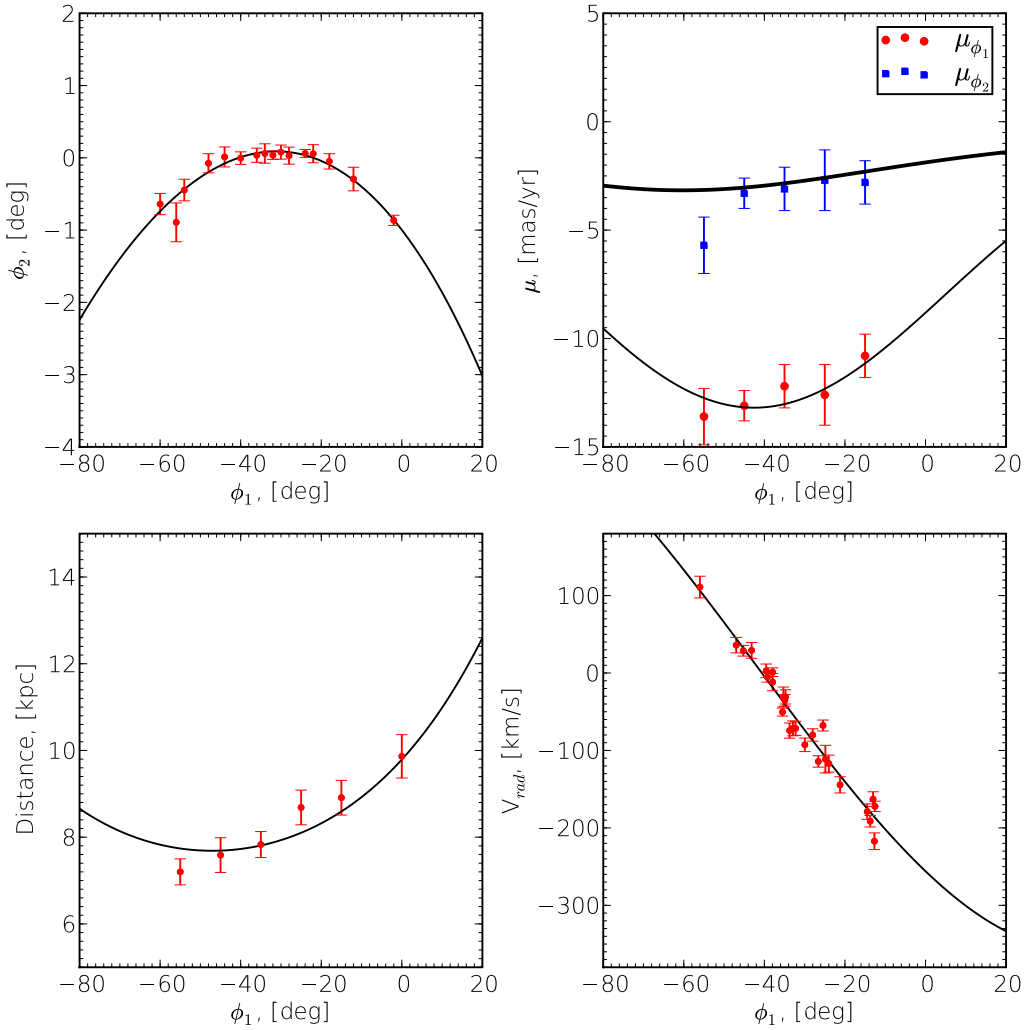

Figure 3.13: The data-model comparison for the best fit orbit in a flattened logarithmic potential (Eq. 3.5 with $V_c = 220\,\mathrm{km/s}$ and q_Φ=0.9. The color data points with error bars shows the observational data, while the black lines show the model predictions for the orbit with $\vec{X}(0) = (-3.41, 13.00, 9.58)\,\mathrm{kpc}$, $\dot{\vec{X}}(0) = (-200.4, -162.6, 13.9)\,\mathrm{km/s}$. The top left panel shows the positions on the sky, the top right panel shows the proper motions, the bottom left panel shows the distances, the bottom right panel shows the radial velocities. On the top right panel, red circles and thin line show μ_{ϕ_1}, while blue squares and thick line show μ_{ϕ_2}.

$[(\vec{X}(0), \dot{\vec{X}}(0)|\Phi(\vec{X})]$ we can evaluate the quality of the fit by calculating χ^2, summing over all data points, shown in Fig. 3.13. For any given $\Phi(\vec{X})$, χ^2 can be then minimized with respect to the orbit, i.e. $(\vec{X}(0), \dot{\vec{X}}(0))$, providing the 'best fit' orbit in this potential and the plausibility of that potential. The minimization is performed using the MPFIT code (Markwardt, 2009) implementing the Levenberg-Marquardt technique (Marquardt, 1963) translated into Python[1]. The data used to constrain the potential are given in the Tables 3.1, 3.2, 3.3, 3.4 (except the SDSS measurements of the radial velocities which are given in the end of Section 3.3).

It is crucial to note that the conversion of $(\vec{X}(t), \dot{\vec{X}}(t))$ to the space of observables depends on the position and motion of the observer, i.e. on distance from the Sun to the Galactic center (R_0) and on the 3D velocity of the Sun in the Galaxy rest-frame ($\vec{V}_0$). At this stage we adopt $R_0 = 8.5\,\mathrm{kpc}$ based on recent determinations (e.g. Ghez et al., 2008), but later we will relax this. The second parameter $\vec{V}_0 \equiv \vec{V}_{LSR} + \Delta\vec{V}_{LSR}$ (where V_{LSR} is the velocity of the Local Standard of Rest and $\Delta\vec{V}_{LSR}$ is the Sun's velocity relative to the LSR) is linked to the fitting not only through conversion of the observable relative stream velocities to the GC rest system, but also conceptually through the plausible demand that $\Phi(\vec{X})$ and in particular $V_c(R_0, 0)$ also reproduces $\vec{V}_{LSR}$. In this way, constraints on the potential flattening can be derived by considering $r\frac{d\Phi}{dr}$ in the disk plane ($\vec{V}_{LSR}$) and the plane of the GD-1 stream. The velocity of the Sun relative to the Local Standard of Rest (LSR) $\Delta\vec{V}_{LSR}$ is quite well known from the HIPPARCOS measurements (Dehnen and Binney, 1998): $\Delta\vec{V}_{LSR}[km/s] = 10\vec{e}_x + 5.25\vec{e}_y + 7.17\vec{e}_z$. The velocity of the LSR, i.e. $V_c(R_0, 0)$ has a considerable uncertainty (Brand and Blitz, 1993; Ghez et al., 2008; Reid et al., 2009; Xue et al., 2008). Initially we will consider the velocity of the LSR simply a consequence of the assumed potential, i.e. $V_{LSR} \equiv V_c(R_0, 0)$.

Figure 3.13 illustrates the result of such fitting, by overplotting the best fit orbit for the plausible potential with $V_c = 220\,\mathrm{km/s}$ and $q_\Phi = 0.9$ over observational data. It is clear that even for the simple flattened logarithmic potential, an orbit can be found that reproduces the observables well. This fit and Figure serve to illustrate a few generic points that also hold for orbit fits in differing potentials: the stream moves on a retrograde orbit and it is near pericenter, where the stream is expected to approximate an orbit well (Dehnen et al., 2004). After fitting a first orbit, we may also note its

[1] `http://code.google.com/astrolibpy/`

global parameters (see Fig. 3.17 for a 3D map of the orbit): pericenter is at 14 kpc from the GC; apocenter is at 26 kpc; and the inclination is 39°.

For any given potential $\Phi(\vec{X}|V_c, q_\Phi)$ we can find best-fit orbit by marginalizing over $(\vec{X}(0), \dot{\vec{X}}(0))$ to see what our 6-D map of GD-1 implies about the relative plausibility of different V_c and q_Φ: Figure 3.14 shows the log-likelihood surface for the potential parameters (V_c, q_Φ); note again that this fit neglects all other prior information on V_c at the Sun's position. The contours show 1σ, 2σ, 3σ confidence regions on the parameters, derived from the $\delta(\ln(\mathcal{L}))$ values for two degrees of freedom (i.e. a two parameter fit)(see e.g. Lampton et al., 1976). The insets at the left and bottom show the marginalized distributions for single parameters. The best fit values with the 2-sided 68% confidence intervals are $V_c = 221^{+16}_{-20}$ km/s and $q_\Phi = 0.87^{+0.12}_{-0.03}$. Figure 3.14 illustrates that the flattening parameter q_Φ is quite covariant with the equatorial circular velocity V_c. An extreme example may serve to explain this covariance qualitatively. If the stream went right over the pole (z-axis), then the local force gradient would be proportional to $V_c \times q_\Phi$ (Eq. 3.5). Information about the potential flattening must therefore come from combining kinematics and dynamics in the disk plane with the information from GD-1 .

The fit shown in Fig. 3.14 asks the data not only to constrain the potential at the stream location and determine the stream orbit, but also to infer the Sun's motion (or at least V_{LSR}) from its reflex effect on the data. Clearly providing a prior on $V_c(R_0, 0)$ is sensible, especially if we care about constraints on the potential flattening. We consider the constraints that arise from the Sun's reflex motion with respect to the Galactic center the most robust and sensible prior in this context. Ghez et al. (2008) recently combined radio data (Reid and Brunthaler, 2004) with near-IR data on the Galactic center kinematics to arrive at $V_c(R_0, 0) = 229 \pm 18$ km/s. It is also noticeable that our own constraint on $V_c(R_0, 0)$ from Fig. 3.14, 221^{+16}_{-20} km/s, is close both in value and uncertainty to the estimate of Ghez et al. (2008), which is based on a completely disjoint dataset and approach.

Fig. 3.15 shows the resulting log-likelihood contours and 1σ, 2σ, 3σ confidence regions after applying this prior on the V_c (229±18 km/s). Note that likelihood on Fig. 3.15 is also marginalized over R_0 with a Gaussian prior ($R_0 = 8.4 \pm 0.4$ kpc Ghez et al., 2008).

Fig. 3.15 shows that the posterior probability distribution on V_c has slightly changed to $V_c(R_0) = 224^{+12}_{-14}$ km/s with noticeably smaller error bar compared to the value from

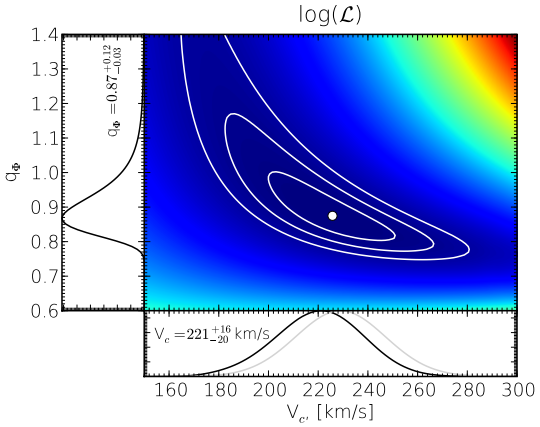

Figure 3.14: The log-likelihood surface of the orbit fit for the family of flattened logarithmic potentials (Eq. 3.5) with different circular velocities V_c and flattenings q_Φ with a flat prior on V_c. Note that V_c enters both into the model velocities of the stream stars and into the correction of all three velocity components for the Sun's motion. The contours show the 1σ, 2σ and 3σ confidence regions. The inset panels at the bottom and on the left show the 1D marginalized posterior probability distributions for V_c, q_Φ respectively. The gray line in the bottom panel shows the probability distribution for the V_c from Ghez et al. (2008), which we shall use as a prior in Fig. 3.15.

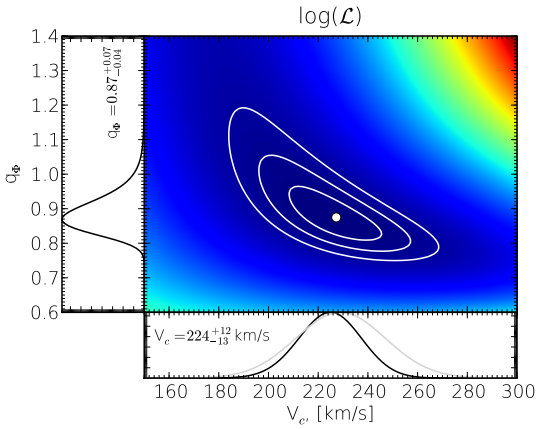

Figure 3.15: The log-likelihood surface of the orbit fit for the family of flattened logarithmic potentials (Eq. 3.5) with different circular velocities V_c and flattenings q_Φ, but now with a prior on the V_c of 229 ± 18 km/s from Ghez et al. (2008). The likelihood was also marginalized over the Gaussian prior on $R_0 = 8.4 \pm 0.4$ kpc. As on Fig. 3.14 the contours show the 1σ, 2σ and 3σ confidence regions. The inset panels at the bottom and on the left show the 1D marginalized posterior probability distributions for V_c, q_Φ respectively. The gray line in the bottom panel shows the adopted prior distribution for the V_c from Ghez et al. (2008)

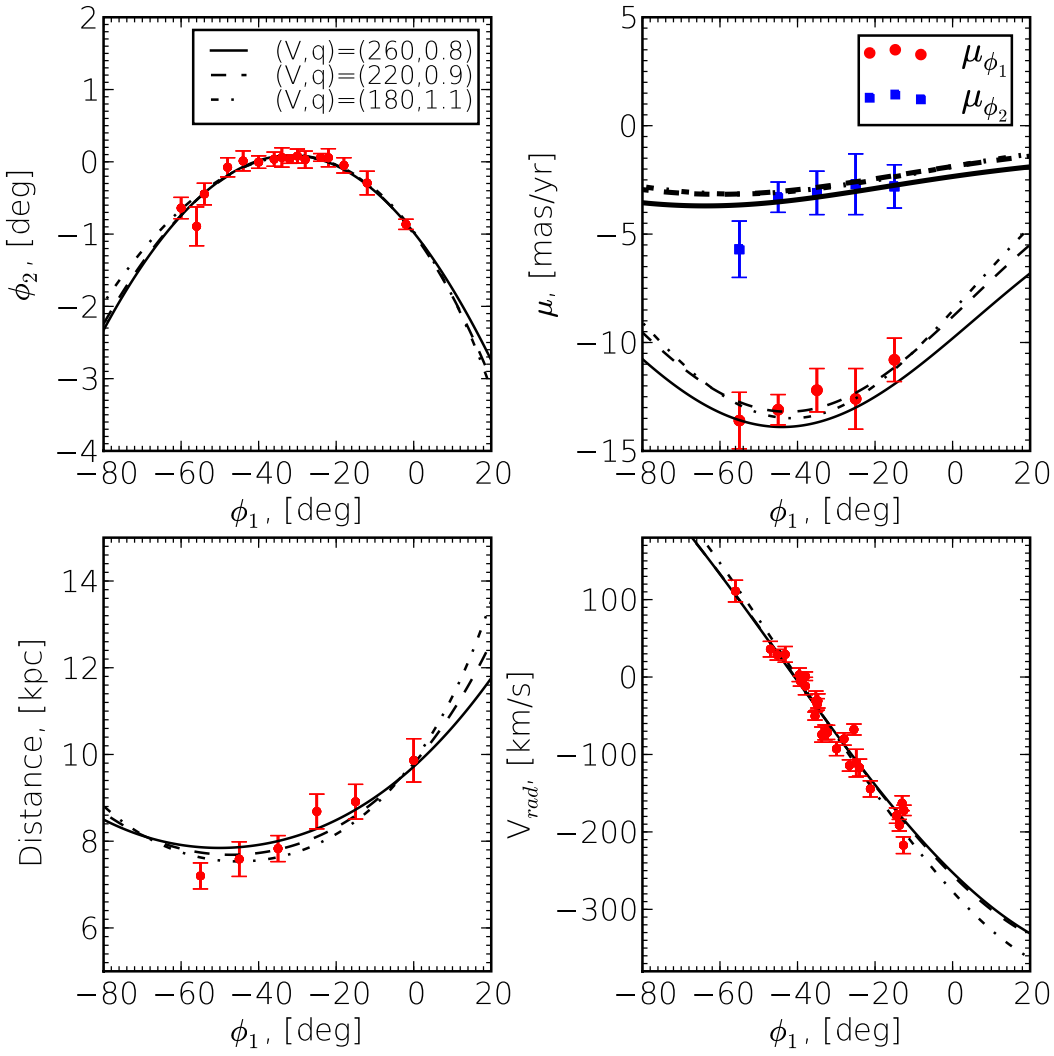

Figure 3.16: The data-model comparison for a set of best-fit orbits in different logarithmic potentials (Eq. 3.5) with three different (V_c, q_Φ) parameters values (180 km/s, 1.1), (220 km/s, 0.9), (260 km/s, 0.8.) The colored data points with error bars show the observational data, while the black lines show the model predictions (different line styles show the orbit models in different potentials). The top left panel shows the positions on the sky, the top right panel shows the proper motions, the bottom left panel shows the distances, the bottom right panel shows the radial velocities. On the top right panel, red circles and thin lines show μ_{ϕ_1}, while blue squares and thick lines show μ_{ϕ_2}.

Ghez et al. (2008). Fig 3.15 also shows us the slightly improved comparing to Fig. 3.14 flattening constraints: $q_\Phi = 0.87^{+0.07}_{-0.04}$. This means that the *total* potential appears to be oblate (in the radial range probed); this may not be surprising, as the stellar disk – which is manifestly very flattened – contributes to the total potential.

Fig. 3.16 illustrates how well the best-fit orbits for different potentials $\Phi(\vec{X}|V_c, q_\Phi)$ can mimic one another other in the space of observables. This is the source of the parameter covariances shown in Fig. 3.14 and 3.15.

The fitting of the orbit shown in Fig. 3.13 allows us to make an estimate of the line-of-sight velocity dispersion in the stream, by comparing the dispersion of the radial velocity residuals with the accuracy of individual radial velocities. This gives an estimate of $\sim 7\,\mathrm{km/s}$, which should be interpreted as an upper-limit for the velocity dispersion of the stars in the stream.

Before we aim at separating possible flattening contributions from the halo and disk, it is worth commenting on the accuracy and limitations of our estimate of q_Φ. In the range $(R, z) \approx (12, 6)\,\mathrm{kpc}$ no other direct observational constraints on the potential shape exist in the literature, and hence our estimate of $q_\Phi = 0.87^{+0.07}_{-0.04}$ is a new and important contribution. On the other hand, an error of $\delta q_\Phi \sim 0.05$, especially when translated into the flattening error of the equivalent scale-free mass distribution, may not appear as particularly helpful in model discrimination, or as impressively accurate. Especially as a manifestly cold stellar stream spanning over 60° on the sky may seem ideal for mapping the potential at first glance.

3.5.2 Constraints on the shape of the dark matter halo from a bulge, disk, halo 3-component potential

In the previous section we constrained the parameters of a simplified MW potential, the spheroidal logarithmic potential. It is clear that the MW potential at the position of the stream must depend explicitly on the sum of baryonic Galaxy components (bulge and disk) and on the dark matter halo. We now explore whether our constraint on the shape of the overall potential, $q_\Phi \sim 0.9$, permits interesting statements about the shape of the DM potential itself. At the distance of $(R, z) \approx (12, 6)\,\mathrm{kpc}$ the contribution of the disk to the potential should still be relatively large, weakening or at least complicating inferences on the shape of the DM distribution.

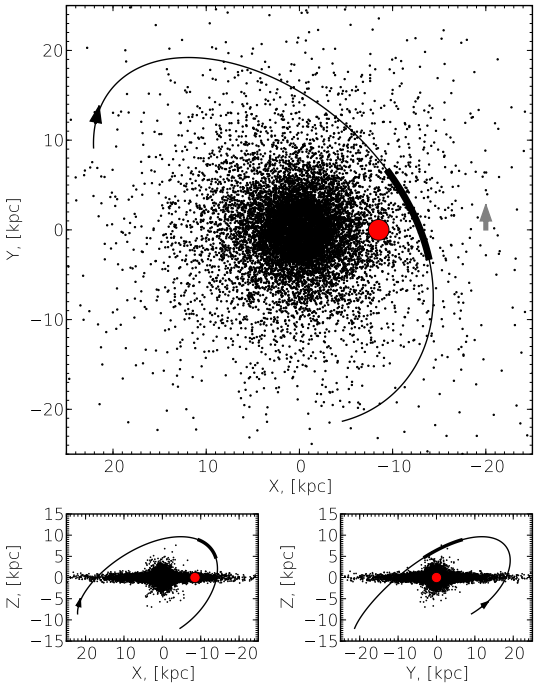

Figure 3.17: 2D projections of the orbit in the Galactic rectangular coordinates. The position of the Sun is shown by a red circle. The Galaxy is shown by a cloud of points and the gray arrow shows the direction of the galactic rotation. The black arrow shows the direction of the orbital movement of the stream stars. The orbit is the best fit orbit for the $V_c = 220\,\mathrm{km/s}$, $q_\Phi = 0.9$ logarithmic potential (Eq. 3.5). The orbit for the 3-component potential (Eqns. 3.6, 3.7, 3.8) is almost undistinguishable from the orbit in logarithmic potential.

3. CONSTRAINING THE MW POTENTIAL WITH A 6-D PHASE-SPACE MAP OF THE GD-1 STREAM

We adopt a three-component model of the Galaxy potential, choosing one that is widely used in the modeling of the Sgr stream (Fellhauer et al., 2006; Helmi, 2004; Law et al., 2005) and reproduces the galactic rotation curve reasonably well.

The model consists of a halo, represented by the logarithmic potential

$$\Phi_{halo}(x,y,z) = \frac{v_{halo}^2}{2} \ln\left(x^2 + y^2 + \left(\frac{z}{q_{\Phi,halo}}\right)^2 + d^2\right), \tag{3.6}$$

where we have adopted $d = 12\,\mathrm{kpc}$ from the previous authors. The disk is represented by a Miyamoto-Nagai potential (Miyamoto and Nagai, 1975),

$$\Phi_{disk}(x,y,z) = \frac{GM_{disk}}{\sqrt{x^2 + y^2 + (b + \sqrt{z^2 + c^2})^2}} \tag{3.7}$$

with $b = 6.5\,\mathrm{kpc}$, $c = 0.26\,\mathrm{kpc}$. The bulge is modeled as a Hernquist potential:

$$\Phi_{bulge}(x,y,z) = \frac{GM_b}{r + a} \tag{3.8}$$

with $M_b = 3.4 \times 10^{10} M_\odot$, $a = 0.7\,\mathrm{kpc}$

As in the previous section, for any given set of potential parameters, we can find the best-fitting stream orbit and compute χ^2 of the fit. Currently we do not make any attempts to fully fit all the parameters of the MW potential, but we try to make an estimate of the MW DM halo flattening. We take the 3-component potential and fix all but 3 parameters — disk mass M_{disk}, circular velocity of the halo v_{halo} and the flattening of the halo $q_{\Phi,halo}$. On a 3D grid of these parameters we perform a χ^2 fit. Figure 3.18 shows the results of such fit after marginalization over the orbital parameters $(\vec{X}(0), \dot{\vec{X}}(0))$, circular velocity of the halo v_{halo} with a Gaussian prior from Xue et al. (2008) and a Gaussian prior on the circular velocity at the Sun's radius from Ghez et al. (2008). The Figure clearly illustrates that in the case of the 3-component potential, the current data is unable to give a significant new insights on the flattening of the DM halo. We can only say that at 90% confidence $q_{\Phi,halo} > 0.89$. We note however that for the future analysis, if a multi-component model for the potential is used then more prior information is required, i.e. not only on V_{LSR} and v_{halo} but on M_{disk} and other parameters of the potential.

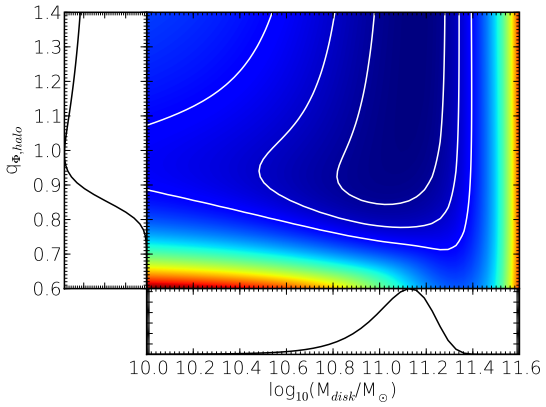

Figure 3.18: The log-likelihood surface of the orbit fit for a 3-component potential (Eq. 3.6, 3.7 and 3.8) with different disk masses M_{disk}, halo circular velocities v_{halo} and halo flattenings $q_{\Phi,halo}$. The likelihood was marginalized over the circular velocity of the halo v_{halo} with the Gaussian prior on $v_{halo} = 170 \pm 15\,\mathrm{km/s}$ from Xue et al. (2008) and the Gaussian prior on $V_{LSR} = 229 \pm 18\,\mathrm{km/s}$) from Ghez et al. (2008) . The contours show the 1σ, 2σ and 3σ confidence regions. The inset panels at the bottom and on the left show the 1D marginalized posterior probability distributions for M_{disk}, $q_{\Phi,halo}$ respectively.

3.6 Discussion and Conclusions

In this chapter we have presented a thorough analysis the GD-1 stream combining the publicly available SDSS and SEGUE data with follow-up spectroscopic observations from Calar Alto. The combination of the photometric SDSS observations, SDSS/USNO-B1.0 proper motions, SDSS, SEGUE and Calar Alto radial velocities allowed us to construct a unprecedented 6-D phase-space map of the stream. The 6-D phase-space map of the stream, spanning more than 60° on the sky, provided the opportunity not only to fit the orbit as Grillmair and Dionatos (2006b) and Willett et al. (2009) have done previously but to explore what constraints can be placed on the MW potential.

The analysis is based on the assumption that the stream stars occupy one orbit. In detail, of course, different stars on the stream have slightly different values of conserved quantities and therefore lie on slightly different orbits. Effectively, our analysis depends on these being small when compared with an orbital uncertainties. The magnitude of the departure of the stream from a single orbit will, in detail, be a function of the progenitor and the disruption process; as these details became understood the model

can be refined.

We found that the distribution of stream stars in phase space can be well fit by an inclined eccentric orbit in the spheroidal logarithmic potential. After marginalization over the stream orbital parameters we derive a circular velocity $V_c = 221^{+16}_{-20}\,\mathrm{km/s}$ and flattening $q_\Phi = 0.87^{+0.12}_{-0.03}$. This measurement has been made without the use of any information other than that in the GD-1 stream itself. It is important that the information available in the observations of the stream is very sensitive to the V_c, the circular velocity at the Sun's position. The reason for that is that the stream extends more then 60° on the sky and therefore both the radial velocities and the proper motions have components coming from the projection of the Sun's motion.

If we combine our circular velocity measurement with existing prior on the V_c from Ghez et al. (2008) and also marginalize over the distance from the Sun to the Galactic center using the Ghez et al. (2008) prior ($R_0 = 8.4 \pm 0.4\,\mathrm{kpc}$), we further tighten the error bar on $V_c = 224^{+12}_{-13}\,\mathrm{km/s}$ and on the flattening of the potential $q_\Phi = 0.87^{+0.07}_{-0.04}$. Our measurement of the V_c is the best constraint to date on the circular velocity at the Sun's position, and the measurement of q_Φ is the only strong constraint on q_Φ at galactocentric radii near $R \sim 15\,\mathrm{kpc}$.

The measurement of the flattening of the potential $q_\Phi = 0.87^{+0.07}_{-0.04}$ describes only the flattening of the overall Galaxy potential at the stream's position $(R, z) \approx (12, 6)\,\mathrm{kpc}$ where the disk contribution to the potential is presumably large. Unfortunately the data on the GD-1 stream combined with the Ghez et al. (2008), Xue et al. (2008) priors on V_c and v_{halo} are not enough for separating the flattening of the halo from the flattening of the total Galaxy potential. So we are unable to place strong constraints on flattening of the MW DM halo; we put a 90% confidence lower limit at $q_{\Phi,halo} > 0.89$.

Despite the negative result on the measurement of the MW DM halo flattening, we note that the data from the GD-1 stream is able to give strong constraints on two important Galaxy parameters. We claim that that our dataset on the GD-1 stream should now be combined with all the available data in order to tighten the existing constraints on the Galaxy parameters. It is important that the constraints on Galaxy potential based on the GD-1 stream dataset are, to large extent, model-independent and purely kinematic i.e. the constraints on the V_c come to large extent from the projection effects and manifest themselves in proper motions and radial velocities.

It is important that while the observed part of the orbit spans $\sim 70^\circ$ on the sky from the Sun's point of view, the orbital phase spanned by the stars as seen from the Galactic center, is only $\sim 40^\circ$. That makes it plausible why orbits of different eccentricities, and hence of different azimuthal velocities at their pericenter, can match so closely the same set of 6-D coordinates. Since very cold streams take many orbits to spread a substantial fraction of 2π in orbital phase (see e.g. also Pal 5; Grillmair and Dionatos, 2006a; Odenkirchen et al., 2001), all future analyses of yet-to-be discovered streams will particularly need to consider the trade-off between the conceptual and practical attractiveness of 'cold' streams and the near-inevitable limitations of their phase coverage.

In addition to the weakness coming from phase coverage, our analysis at this point must rely on photometric distance estimates; these have random errors of $\sim$10%, after an empirical distance correction to the best fit isochrones that is of the same magnitude (see Section 3.2). While the proper motions that we derived for ensembles of stream stars are unprecedented for a stellar stream in the Milky Way's outer halo; yet, the corresponding velocity precision, especially when compounded by distance errors, is still the largest single source of uncertainty in the fitting (e.g. our tests have shown that overestimating heliocentric distances to the stream leads to the overestimated measurement of V_c).

We suggest that future observations of radial velocities of the stream and improvements in proper motion precision should be able to reduce the error bars on Galaxy parameters significantly. It is also important to calibrate properly the distance to the stream, which may be possible via several probable BHB candidates in the stream. Another way to improve the constraints on the Galactic potential is by understanding how much the stream deviates from a single test particle orbit.

We suggest that any attempt to fit the Galaxy potential now should not ignore the dataset on GD-1 and should incorporate it into their fits.

The orbital parameters, which we measured for the GD-1 stream, are more or less consistent with those from Willett et al. (2009): pericenter is at 14 kpc from the GC, the apocenter is at 26 kpc, the orbit inclination with respect to the Galactic plane is 39°. We also estimate the total stellar mass associated with the stream to be $\sim 2 \times 10^4 M_\odot$, which together with the stream width of $\sim$ 20 pc unambiguously confirms that the

progenitor of the stream was a globular cluster. We also measured the upper limit for the velocity dispersion of the stars in the stream $\sim 7\,\mathrm{km/s}$.

Overall in this chapter we have illustrated a method of analyzing the thin stellar stream using all the available information on it and further utilizing that to constrain the Galaxy potential. We believe that in the epoch of Pan-STARRS, LSST and especially GAIA, which will give us a wealth of new information on the MW halo, stream-fitting like that presented in this chapter will be extremely useful and productive.

4

Luminosity Function of MW satellites

This chapter reproduces the paper: S. Koposov, V. Belokurov, N. W. Evans, P. C. Hewett, M. J. Irwin, G. Gilmore, D. B. Zucker, H.-W. Rix, M. Fellhauer, E. F. Bell, and E. V. Glushkova. "The Luminosity Function of the Milky Way Satellites" published in ApJ, volume 686, page 279-291, October 2008a.

4.1 Introduction

In Cold Dark Matter (CDM) models, large spiral galaxies like the Milky Way and M31 form within extensive dark matter halos from the merging and accretion of smaller systems. Although CDM models have had many successes on larger scales, one of the most serious challenges facing CDM models is the so-called "missing satellite" problem. First identified by Klypin et al. (1999) and Moore et al. (1999), the problem manifests itself through the prediction by CDM models of at least 1-2 orders of magnitude more low-mass subhalos at the present epoch compared to the observed abundance of dwarf galaxies surrounding the Milky Way and M31.

There have been a number of theoretical proposals to solve this problem. For example, the satellites that are observed could be embedded only in the rarer, more massive dark subhalos (Stoehr et al., 2002), or, the satellites may form only in the rare peaks of halos that were above a given mass at reionization (Diemand et al., 2005; Moore et al., 2006). Alternatively, star formation in low mass systems could

be inhibited by photoionization in the early Universe (Benson et al., 2002; Bullock et al., 2001b; Somerville, 2002). All these ideas do not alter the abundance of dark matter subhalos, but propose to solve the observed discrepancy by producing a smaller number of directly observable satellites, thus breaking any simple relationship between mass and luminosity.

The known Milky Way dwarf spheroidal (dSph) satellites have been discovered by a variety of methods. The first seven were discovered serendipitously by visual inspection of photographic plates, the Sextans dSph was found using automated scans of photographic plates and the Sagittarius dSph in a radial velocity survey of the Milky Way bulge. All-sky photographic surveys cover most of the sky away from the Zone of Avoidance, but searches of plates are limited to surface brightnesses of ~ 25.5 mag arcsec^{-2} (Whiting et al., 2007). The sample of known dSphs has long been bedeviled with selection effects, which are difficult to model with any accuracy. This situation has changed recently with the advent of very large area, homogeneous, photometric surveys such as the Sloan Digital Sky Survey (SDSS; York et al., 2000). The SDSS makes it possible to carry out a systematic survey for satellite galaxies, which are detectable through their resolved stellar populations down to extremely low surface brightnesses. In essence, SDSS greatly facilitates systematic searches for overdensities of stars in position-color-magnitude space.

Willman et al. (2002) carried out the first SDSS–based survey for resolved Milky Way satellites, subsequently discovering a new dwarf galaxy, Ursa Major (Willman et al., 2005b) as well as an unusually large globular cluster, Willman 1 (Willman et al., 2005a) – although later evidence may favor its interpretation as a dark matter dominated dwarf galaxy with multiple stellar populations (Martin et al., 2007). The color image "Field of Streams" (Belokurov et al., 2006c), composed of magnitude slices of the stellar density in the SDSS around the North Galactic Cap, proved to be a treasure-trove for dwarf galaxies, as Canes Venatici, Bootes I and Ursa Major II (Belokurov et al., 2006b; Zucker et al., 2006a,b) were all found in quick succession. A systematic search in the "Field of Streams" led to the discovery of five more satellite galaxies, Canes Venatici II, Leo IV, Hercules, Coma, and Leo T, as well as another large globular cluster, Segue 1 (Belokurov et al., 2007c; Irwin et al., 2007). Very recently, Walsh et al. (2007) discovered another low luminosity satellite, Bootes II.

As the faintest Milky Way satellites currently constitute our best markers of subhalos, the faint end of the satellite luminosity function of the Milky Way satellites can provide stringent constraints on the process of galaxy formation, and can distinguish between a number of dark matter, structure formation and reionization models. So, it is important not merely to carry out a systematic survey of the star overdensities in SDSS data for the discoveries per se, but also to compute the detection limits. These detection limits are the basis for a volume corrected luminosity function estimate and ultimately for a quantitative connection of satellite frequency and subhalo abundance. Such is the purpose of this chapter. It is important to note that for a volume-corrected estimate of the luminosity function, it is not necessary to use exactly the same detection algorithms as Belokurov et al. (2007c) or Willman et al. (2005b). Similarly, the detection scheme does not need to be optimal for every individual dwarf galaxy. Provided the automated algorithm is able to detect all the Milky Way satellites, and the completeness properties of the algorithm are quantified, an estimate of the true luminosity function can be derived.

4.2 Detection of Satellite Galaxy Candidates in SDSS DR5

The SDSS Data Release 5 (DR5) covers $\sim 1/5$ of the sky, or ~ 8000 square degrees around the North Galactic Pole. SDSS imaging data are produced in five photometric bands, u, g, r, i, and z (Adelman-McCarthy et al., 2006; Fukugita et al., 1996; Gunn et al., 1998, 2006; Hogg et al., 2001). The data are automatically processed through pipelines to measure photometric and astrometric properties (Lupton et al., 1999; Pier et al., 2003; Stoughton et al., 2002; Tucker et al., 2006). All magnitudes quoted in this chapter have been corrected for reddening due to Galactic extinction using the maps of Schlegel, Finkbeiner, and Davis (1998). Sometimes it is convenient to report our results in the V band, for which we use the transformation $V = g - 0.55(g - r) - 0.03$ given by Smith et al. (2002).

The SDSS data with the source catalogs used in this chapter was downloaded from the SAI CAS Virtual Observatory data center[1](Koposov et al., 2007a) and was stored locally in the PostgreSQL database. To perform queries rapidly on the large dataset, we used the Q3C plugin for the spatial queries (Koposov and Bartunov, 2006).

[1] `http://vo.astronet.ru`

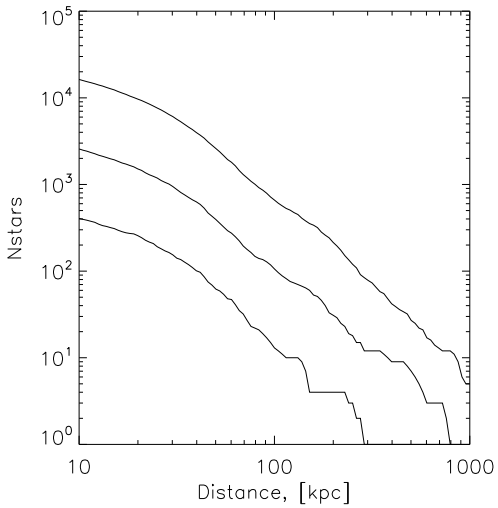

Figure 4.1: The number of stars brighter than $r \simeq 22.5$ in random realizations of Milky Way satellites of luminosity $M_r \sim -3, -5, -7$ (from bottom to top) with M92-like stellar populations, as a function of distance from the Sun. The approximate number of stars required for a significant detection (by the algorithm described in Section 4.2) is $\simeq$30.

All the recent SDSS discoveries of dSph around the Milky Way, bar Leo T, are not directly visible in the flux-limited images, but were detected as overdensities of resolved stars within certain magnitude and color ranges. This makes it straightforward to automate a detection method and assess its efficiency. The essence of any detection algorithm is to count the number of stars in a certain (angular) region on the sky, satisfying specified color and magnitude criteria, and compare the number to the background value. The excess of stars depends on the satellite's luminosity and distance. For a given luminosity, the distance fixes the number of stars brighter than the SDSS limiting magnitude, which is given by an integral over the stellar luminosity function. A simple illustration of the detectability of objects with a luminosity function like that of M92 is shown in Figure 4.1. The curves show the number of stars brighter than $r = 22.5$ for satellites of three different absolute magnitudes. The maximal distance probed by surveys like SDSS is controlled by the apparent magnitude of the brightest stars in the satellite. For intrinsically luminous objects, like CVn I ($M_V = -7.9$) , we can detect stars at the tip of the red giant branch at distances of up to $\sim$1 Mpc. However, for satellites with many fewer stars, like Hercules ($M_V = -5.7$), the giant branch tip is simply not populated and we can only detect objects at distances up to

$\sim$300 kpc.

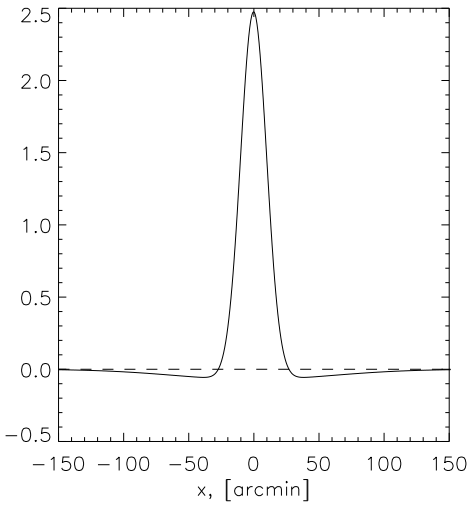

Figure 4.2: Differential convolution kernel applied to the stellar catalog to identify overdensities of a particular scale. A one-dimensional slice of the two-dimensional kernel is shown, where the width, or σ, of the inner Gaussian is $6'$ and of the outer Gaussian is $60'$.

To identify the excess number of stars associated with a satellite, a common approach is to convolve the spatial distribution of the data with window functions or filters [1]. To estimate the star density on different scales, we use a Gaussian of width σ, that is,

$$L(x, y, \sigma) = I(x, y) * g(x, y, \sigma), \tag{4.1}$$

where

$$g(x, y, \sigma) = \frac{1}{2\pi\sigma^2} \exp\left(-\frac{x^2 + y^2}{2\sigma^2}\right) \tag{4.2}$$

and $I(x, y)$ is the distribution of sources

$$I(x, y) = \sum_i \delta(x - x_i, y - y_i) \tag{4.3}$$

This allows us to see the stellar density distribution at different spatial scales. For example, structures with a characteristic size of $1'$ will be more prominent when the

[1] This idea has a long history, particularly in algorithms for searching for features and clusters in imaging data. Widely used in astronomy are kernel-based density estimation methods, in which the density is obtained by convolving all the data points (interpreted as delta-functions) with smoothly decaying kernels, which can be Gaussians (see e.g. Silverman, 1986). A variant of this is used for feature detection in digital images in so-called scale-space science (Babaud et al., 1986; Lindeberg, 1993, 1998).

stellar map is convolved with a $1'$ kernel, and less prominent when the map is convolved with $10'$ and $0.1'$ kernels. The resulting "blobs", or overdensities, can be easily identified on the differential image maps, namely

$$\begin{aligned} \Delta L &= L(x,y,\sigma_1) - L(x,y,\sigma_2) \\ &= I(x,y) * (g(x,y,\sigma_1) - g(x,y,\sigma_2)) \end{aligned} \tag{4.4}$$

Such differential image maps are generally convolutions of the original distribution with the kernel, which is a difference of two Gaussians. A one-dimensional slice of a kernel is shown in Figure 4.2. When we convolve the map $I(x,y)$ with such a kernel, we obtain an estimate of the local density minus an estimate of the local background ($L(x,y,\sigma_2)$). This interpretation allows us to quantify the significance as

$$S(x,y,\sigma_1,\sigma_2) = \frac{\Delta L}{\sigma_L} \tag{4.5}$$

where σ_L^2 is the variance of $L(x,y,\sigma_1)$.

$$\begin{aligned} \sigma_L^2 &= Variance(L(x,y,\sigma_1)) = Variance(I(x,y) * g(x,y,\sigma_1)) = \\ &= I(x,y) * g^2(x,y,\sigma_1) = \sum_{i,j} I(x_i,y_j)\, g^2(x-x_i, y-y_j, \sigma_1) \approx \\ &\approx \sum_{i,j} L(x,y,\sigma_2)\, g^2(x-x_i, y-y_j, \sigma_1) = L(x,y,\sigma_2) \int\int g^2(x,y,\sigma_1)\, dxdy = \\ &= \frac{L(x,y,\sigma_2)}{4\pi\sigma_1^2} \end{aligned} \tag{4.6}$$

$$S(x,y,\sigma_1,\sigma_2) = \sqrt{4\pi}\sigma_1 \frac{\Delta L}{\sqrt{L(x,y,\sigma_2)}}, \tag{4.7}$$

Under the assumption that $\sigma_2 >> \sigma_1$ and a Poisson distribution of the initial set of datapoints, the variance of $S(x,y)$ is unity. This fact allows us to use the map of $S(x,y)$ to identify overdensities above a specified significance threshold.

4.3 Application to SDSS data

SDSS's morphological parameters (Lupton et al., 2001) derived from the imaging data allow robust discrimination between stars and galaxies down to $r = 21.5$. For $21.5 < r \lesssim 22.5$, the discrimination is still reasonably reliable, but it becomes increasingly untrustworthy below $r = 22.5$. Moreover, the catalog is 95% complete at $r = 22.2$ (Stoughton

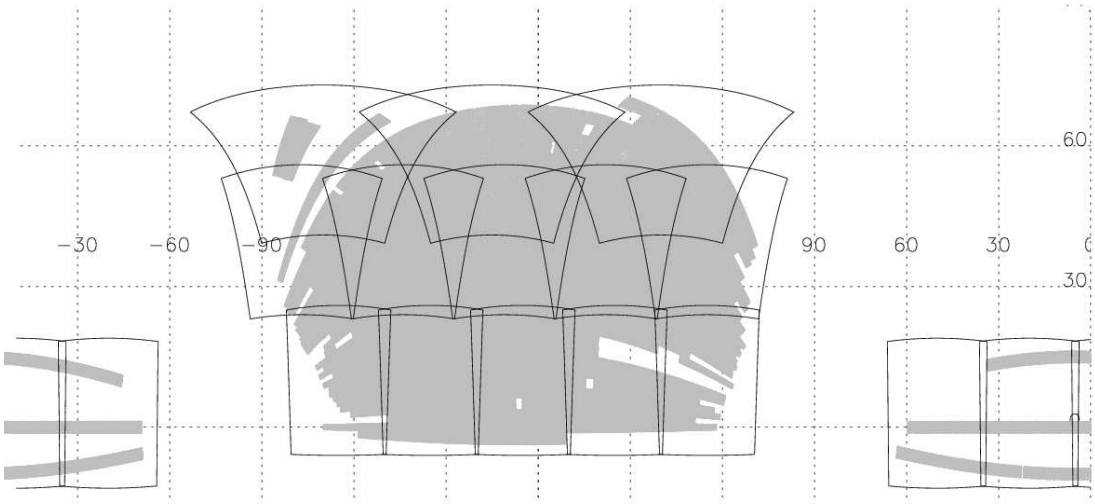

Figure 4.3: The segmentation of the DR5 area into 17 32°× 32° fields, used for the stellar overdensity search described in the text.

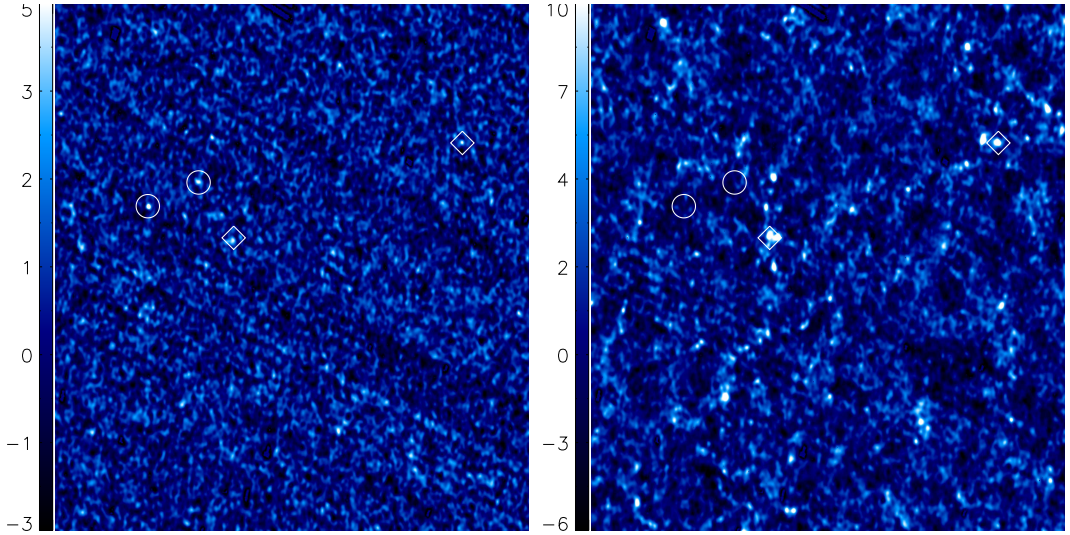

Figure 4.4: A sample 22°× 22°area in the convolved maps of the SDSS DR5 stellar (left) and galaxy (right) catalogs. The positions of objects Ursa Major I and Willman 1 are marked by circles. The positions of galaxy clusters Abell 773 and Abell 1000 are marked by diamonds, and demonstrate that galaxy clusters may lead to significant peaks in the stellar map. The linear diagonal structures seen in both images are caused by SDSS stripes. The images were produced using a kernel specified by $\sigma_1 = 4'$ and $\sigma_2 = 60'$. We reject peaks in the convolved stellar map if they coincide with significant peaks in the galaxy distribution.

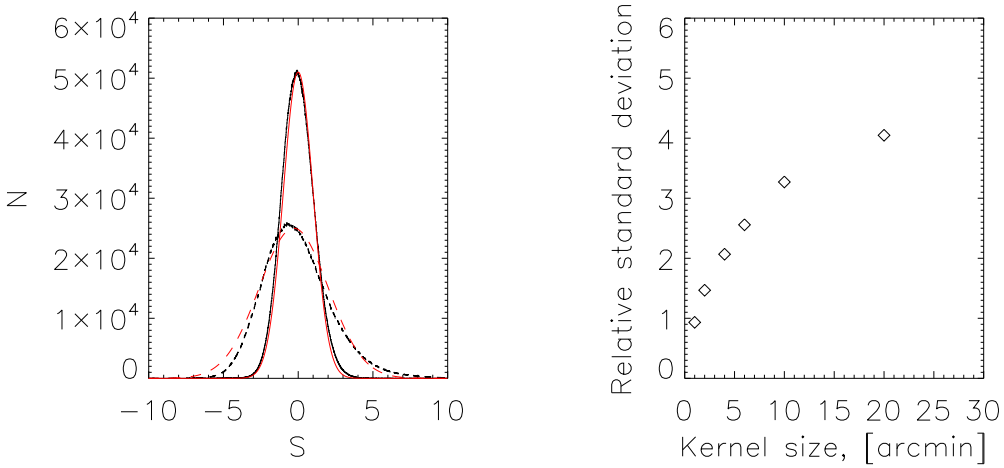

Figure 4.5: Left: The distribution of pixel values in the convolved star map (solid line) and galaxy map (dashed line) for one of our 17 fields in DR5. The Gaussian model curves with width of 1.0 and 2.3 centered on zero are shown in red. Right: The standard deviation in the galaxy map normalized by a Poissonian standard deviation as a function of kernel size.

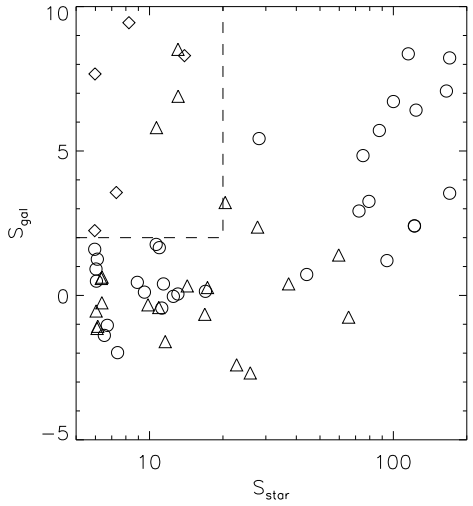

Figure 4.6: Distribution of Milky Way satellite detections in the $S_{\rm star}$ versus $S_{\rm gal}$ plane. The circles mark the known Milky Way satellites, the triangles are RC3 galaxies, and the rhomboids are galaxy clusters. Objects towards the top left of the figure are likely the result of contamination by galaxy clusters or spatially extended galaxies. The decision boundary is shown as a dashed line; objects to the right and below the dashed line are selected as candidate satellites.

Right ascension	Declination	S_{star}	S_{gal}	Name
205.539	28.382	170.13	8.24	NGC 5272
168.355	22.148	170.08	19.16	Leo II
198.220	18.159	165.00	16.48	NGC5024
152.100	12.289	123.86	14.94	Leo I
199.104	17.696	122.09	5.59	NGC 5053
211.359	28.527	121.91	5.61	NGC 5466
229.006	−0.130	115.10	19.48	Pal5
260.038	57.914	100.02	15.64	Draco
250.426	36.467	94.10	2.80	NGC 6205
322.483	12.147	87.58	13.30	NGC7078
182.516	18.544	79.40	7.58	NGC 4147
260.008	57.765	75.07	11.27	Draco
114.534	38.873	72.28	6.80	NGC 2419
323.212	−0.865	65.52	−1.75	NGC 7089
187.670	12.395	59.69	3.25	NGC 4486
202.011	33.549	44.12	1.68	CVn I
187.419	8.003	37.18	0.93	NGC 4472
149.834	30.742	28.13	12.65	Leo A
190.698	2.682	27.73	5.51	NGC 4636
114.608	21.581	25.88	−6.25	NGC 2420
259.027	43.063	22.76	−5.60	NGC 6341
183.904	36.310	20.43	7.49	NGC 4214
185.036	29.286	17.28	0.63	NGC 4278
210.010	14.503	16.95	0.32	Boo I
190.773	11.598	16.84	−1.52	NGC 4647/4637/4638
186.368	12.909	14.28	0.76	NGC 4374
178.814	23.371	13.90	19.34	Abell 1413
186.444	33.539	13.10	16.06	NGC 4395
148.904	69.081	13.08	19.85	NGC 3031
162.325	51.051	13.07	0.11	Willman 1
242.741	14.956	12.52	−0.07	Pal 14

Table 4.1: Objects detected and their significances

Right ascension	Declination	S_{star}	S_{gal}	Name
186.315	18.181	11.59	−3.72	NGC 4382
132.830	63.124	11.40	0.92	UMa II
186.745	23.913	11.22	−1.02	Coma Berenices
143.721	17.058	10.96	3.85	Leo T
188.911	12.544	10.91	−0.97	NGC 4552
210.691	54.332	10.67	13.53	NGC 5457
151.369	0.070	10.64	4.11	Pal 3
186.109	7.294	9.85	−0.76	NGC 4365
172.319	28.961	9.53	0.26	Pal 4
247.764	12.789	8.91	1.05	Hercules
197.870	−1.335	8.23	22.00	Abell 1689
194.292	34.298	7.39	−4.61	CVn II
196.743	46.569	7.30	8.29	Abell 1682
193.379	46.415	6.71	−2.41	Candidate X
168.146	43.440	6.52	−3.22	Candidate Y
352.182	14.714	6.39	1.47	Pegasus
202.388	58.404	6.37	−0.59	NGC 5204
225.323	1.672	6.34	1.36	NGC 5813
187.038	44.090	6.13	−2.49	NGC 4449
173.235	−0.554	6.10	2.92	Leo IV
0.807	16.097	6.09	−2.66	NGC 7814
179.144	21.049	6.05	1.14	Candidate Z
184.843	5.786	6.04	−1.25	NGC 4261
149.993	5.316	6.03	2.12	Sextans B
139.470	51.718	5.97	17.86	Abell 773
179.223	23.379	5.96	5.22	galaxy cluster
158.695	51.918	5.95	3.72	UMa I

Table 4.2: Objects detected and their significances (continuation)

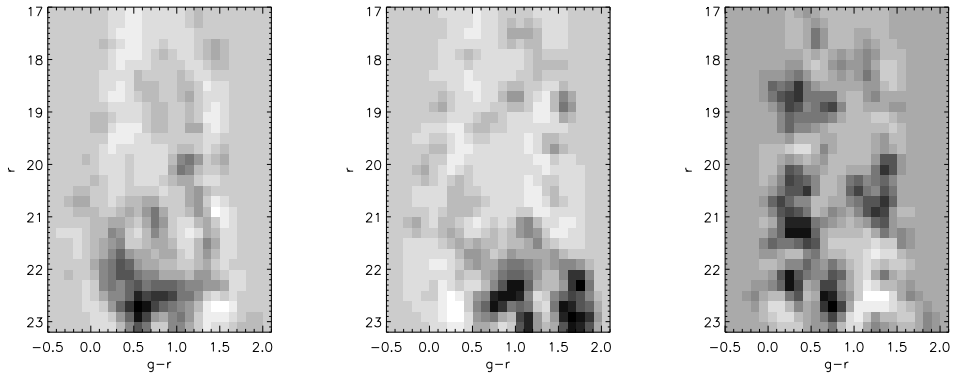

Figure 4.7: Left to right: Hess diagrams for Candidates X, Y and Z listed in Tables 4.1 and 4.2

et al., 2002) and drops quickly below this magnitude. At the faint end, the "stellar" catalog of unresolved sources is polluted by faint galaxies which are intrinsically strongly clustered. We will see shortly that the main task in providing a clean sample of dwarf galaxy candidates is removal of the extragalactic contaminants, for which we will employ the SDSS galaxy catalog.

To proceed with the convolution (Eq. 4.4), the DR5 field of view is split into 17 segments as shown in Figure 4.3. The division is for computational convenience and to minimize distortion in the gnomonic projections. In practice, we select stars and galaxies with a magnitude cut-off of $r < 22.5$. Due to the properties of the kernel, we expect edge effects at the boundaries of the DR5 footprint and we discard all overdensities within 1° of a boundary. We use a color-cut of $g - r < 1.2$ and kernel sizes with $\sigma_1 = 4'$ and $\sigma_2 = 60'$. The color cut is chosen to be as conservative as possible as regards inclusion of the tip of the red giant branch stars for metal-poor populations, whilst the kernel size is of the order of the angular size of the known dwarfs (see next section for details). The color magnitude cut used in this work may not be optimal for the detection of each individual dwarf galaxy (e.g. the isochrone masks should definitely work better), but the primary goal here is not to define an optimal algorithm, but rather to develop a consistent algorithm that can detect known objects, for which the detection efficiency can be determined. Figure 4.4 provides an example of the application of the detection pipeline to the stellar and galaxy catalogs of SDSS DR5. The method successfully removes the varying background to leave underdensities (black regions) and

overdensities (white regions). The sample field of view chosen for Figure 4.4 contains the already known Milky Way satellites Willman 1 and Ursa Major I (Willman et al., 2005a,b). They are both recovered in the stellar map with significances of $S_{\rm star} = 13.07$ and 5.95 respectively. However, as we see in Figure 4.4, unresolved sources in rich galaxy clusters such as Abell 773 and 1000, visible as prominent overdensities in the galaxy map, also show up in the stellar map as significant peaks.

In order to remove false positives caused by galaxy clustering, we need to understand the significance $S_{\rm gal}$ of overdensities in the map derived from the galaxy catalog. Equation (4.7) does not hold, because the underlying distribution is no longer Poissonian (Figure 4.5). The left panel shows the distributions of $S_{\rm star}$ and $S_{\rm gal}$ for all pixels in the same field of view as Figure 4.4. For the stars, the convolved source count distribution is almost a Gaussian with unit standard deviation, whilst the distribution for the galaxies is broader. The right panel shows how the width of the $S_{\rm gal}$ distribution grows with increasing kernel width as the convolution samples coherent structures on larger scales. To assign significance to the overdensities in galaxies, we rescale $S_{\rm gal}$, dividing by its standard deviation.

Next, we remove obvious false positives by rejecting all objects within the region marked by dashed lines in Figure 4.6, namely the intersection of the regions $S_{\rm star} < 20$ and $S_{\rm gal} > 2$. This removes most, but not all, the false positives caused by galaxy clusters. Additionally, there remains contamination from galaxies with large angular size. The SDSS photometric pipeline mis-classifies HII regions and stellar clusters in these galaxies as stars. We remove the contaminants by cross-correlating with the positions of galaxies in the Third Reference Catalogue (RC3) of de Vaucouleurs et al. (1991). Even so, there still remain objects at a moderately high level of significance whose nature is unclear. Most of these are probably caused by galaxy clusters or photometry artifacts, as judged from examination of Hess diagrams and SDSS image cut-outs, but there may still be a very small number of genuine Milky Way satellites.

We detect all the known Milky Way satellites, except Boo II, in a catalog with magnitude limit $r < 22.5$, analyzed using a kernel with $\sigma_1 = 4'$. The most marginal detections are Leo IV and Ursa Major I, which have significances $S_{\rm star} = 6.10$ and 5.95 respectively. Objects above the threshold are listed in Table 4.1, and include three likely false positives, which are "Candidates" X, Y and Z. The Hess diagrams of these three detections are shown in Figure 4.7. The Hess diagrams offer little evidence to

support identification of the candidates as genuine satellites. Deeper data are needed to provide definitive classification of the candidates but for the purpose of determining the satellite luminosity function we exclude all three candidates, as false positives, from further consideration.

It is prudent to search for candidate satellites on the map convolved with different inner kernels, since the kernel biases the algorithm towards objects of a preferred size. Therefore, we performed a search on the map convolved with kernels of $2'$ and $8'$. In the former case, setting the significance to $S_{\rm star} > 6.5$ results in the detection of all objects except UMa I and no false positives; in the latter case, setting $S_{\rm star} > 6.0$ includes all objects except CVn II, Leo IV, LeoT, UMa I and no false positives.

Boo II, found by Walsh et al. (2007), is problematic for our algorithm. Boo II contains a very sparsely populated giant branch, and so the brightest stars are sub-giants and turn-off stars at colors of $g - r < 0.5$. Given our preferred cuts, Boo II is undetected. It can nonetheless be found with our algorithm, but only by optimizing the color and magnitude cuts, for example, to $g - r < 0.5$ and $21 < r < 23$.

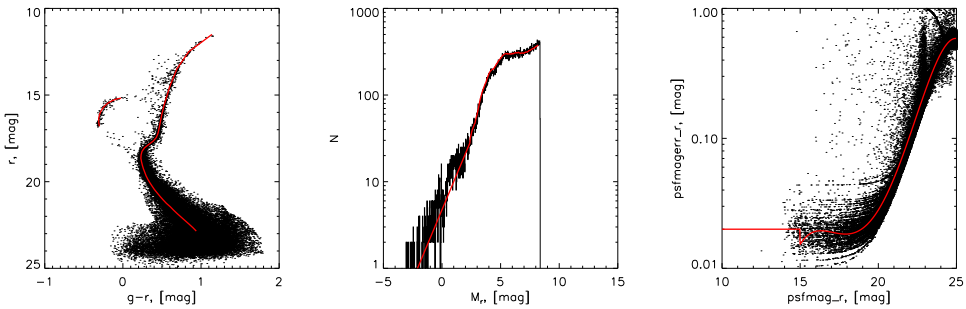

Figure 4.8: Left: M92 color-magnitude data from Clem (2006) used as a template for our simulated Milky Way satellites, together with the ridge line for the main sequence and red giant branch. The ridge line for the horizontal branch is our fit to Clem's (2006) data. Center: The observed luminosity function of main-sequence and red giant branch stars in M92, together with our model fit of the luminosity function used in the simulations. Right: The photometric errors of the SDSS r-band photometry and our model fit used in the simulations

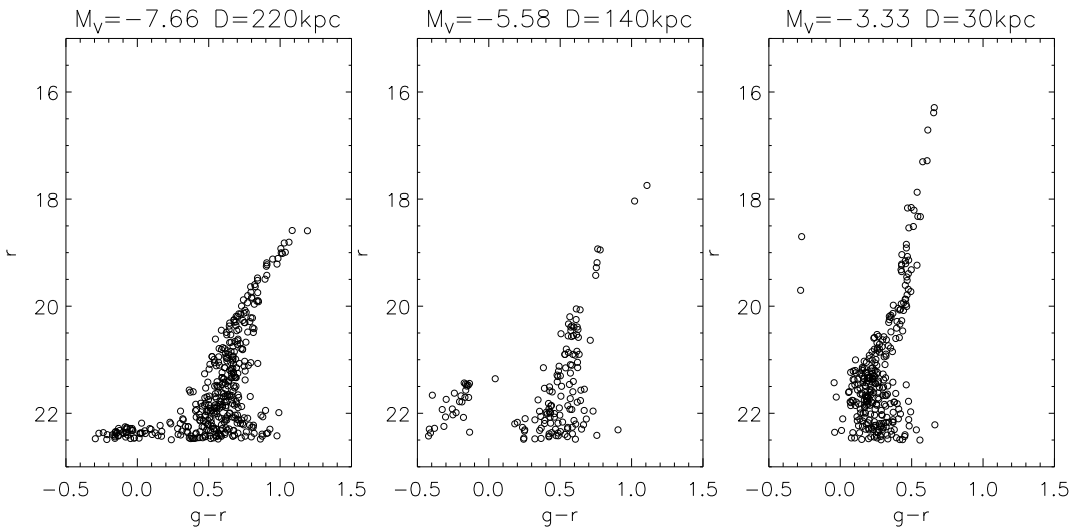

Figure 4.9: Simulated color-magnitude diagrams for hypothetical Milky Way satellite galaxies with properties close to those of Canes Venatici I, Hercules and Ursa Major II—the actual color-magnitude diagrams of these galaxies are given in Zucker et al. (2006a,b) and Belokurov et al. (2007c).

4.4 Application to Simulated Data

To test our detection algorithm, we carry out an extensive set of simulations in which we add mock dwarf galaxy satellites and globular clusters to the SDSS DR5 catalog. In particular, we add to the catalog the g and r magnitudes of stars from the simulated objects, at specified right ascensions and declinations. These augmented catalogs are then fed through our automated pipeline, and the number of stellar overdensities with significance above the threshold is calculated as a function of distance, size and luminosity. We explore how changes in the $g-r$ color cuts and kernel sizes (σ_1 from Eq. 4.7) affect the efficiency of the algorithm.

The g and r photometry of all simulated objects is based on that of the globular cluster M92. The left panel of Figure 4.8 shows the color-magnitude diagram (CMD) of M92, together with a main-sequence and red giant branch ridgeline from Clem (2006), to which we have added a horizontal branch ridgeline. From the r-band data, we construct a main-sequence and red giant branch luminosity function and approximate it with a smooth fit, as shown in the middle panel of Figure 4.8. We also determine the luminosity function for the stars on the horizontal branch ridgeline. We populate

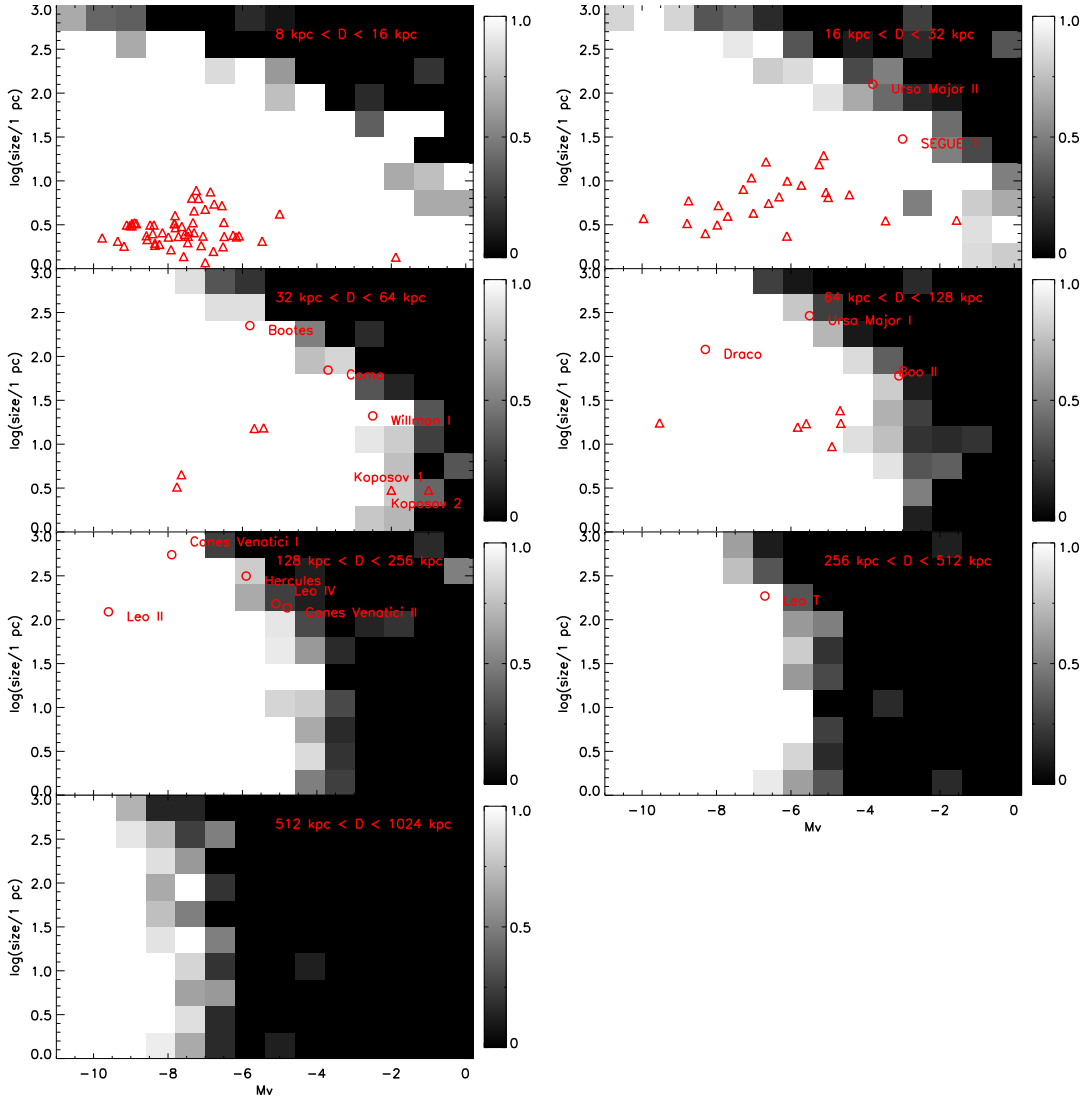

Figure 4.10: Detection efficiency maps for Milky Way satellites, shown as a function of luminosity and size for different distance bins. White indicates 100% detection efficiency, black indicates 0%. Red circles mark the locations of the known dwarf galaxies, red triangles the known globular clusters (data taken from Harris (1996)). Notice that many of the very recent SDSS satellite galaxy discoveries occur near the boundary, where the detection efficiency is changing rapidly.

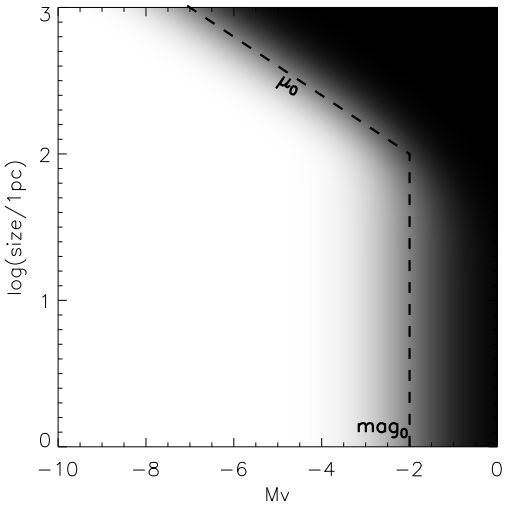

Figure 4.11: Characterizing the satellite galaxy detectability: this illustrative figure shows the model function $\epsilon(M_V, \mu)$ (from Eq. 4.8) used to fit the observed detection efficiencies from the simulations and demonstrating the role played by the thresholds $M_{V,\mathrm{lim}}$ and μ_{lim}. The function parameters used to produce the plot were $M_{V,\mathrm{lim}} = -2\,\mathrm{mag}$, $\mu_{\mathrm{lim}} = 29.5\,\mathrm{mag\,arcsec^{-2}}$, $\sigma_M = 1\,\mathrm{mag}$, $\sigma_\mu = 1\,\mathrm{mag}$

the ridgelines using the luminosity function. The choice is appropriate, as M92 (12 Gyrs, [Fe/H] ≈ -2) is typical of the old, metal-poor populations in the Milky Way satellites (see e.g. van den Bergh, 2000). Additionally, we add a scatter in r- and g- magnitudes, derived from a fit to the errors in the SDSS point-spread function photometry, as illustrated in the right panel of Figure 4.8.

The spatial distribution of stars in the simulated objects is chosen to follow a Plummer law, which is a reasonable fit to most of the Milky Way dwarf spheroidals (see e.g. Irwin and Hatzidimitriou, 1995; Kleyna et al., 2002). For ellipticities less than 0.5 – which corresponds to the most flattened of the SDSS discoveries, Hercules and Ursa Major II (Belokurov et al., 2007c; Zucker et al., 2006a) – the detection efficiency of objects barely changes with ellipticity. The Plummer radius, luminosity and distance are chosen to cover uniformly in logarithmic space the following ranges: Plummer radius $1\,\mathrm{pc} < r_h < 1\,\mathrm{kpc}$, luminosity $-11 \lesssim M_V \lesssim 0$ and heliocentric distance $10\,\mathrm{kpc} < D < 1\,\mathrm{Mpc}$. We generate 8000 galaxies with random right ascension and declination within the DR5 footprint. We then split the simulated sample into 20 distance bins to eliminate overlap between simulated objects. The stars from the simulated galaxies are

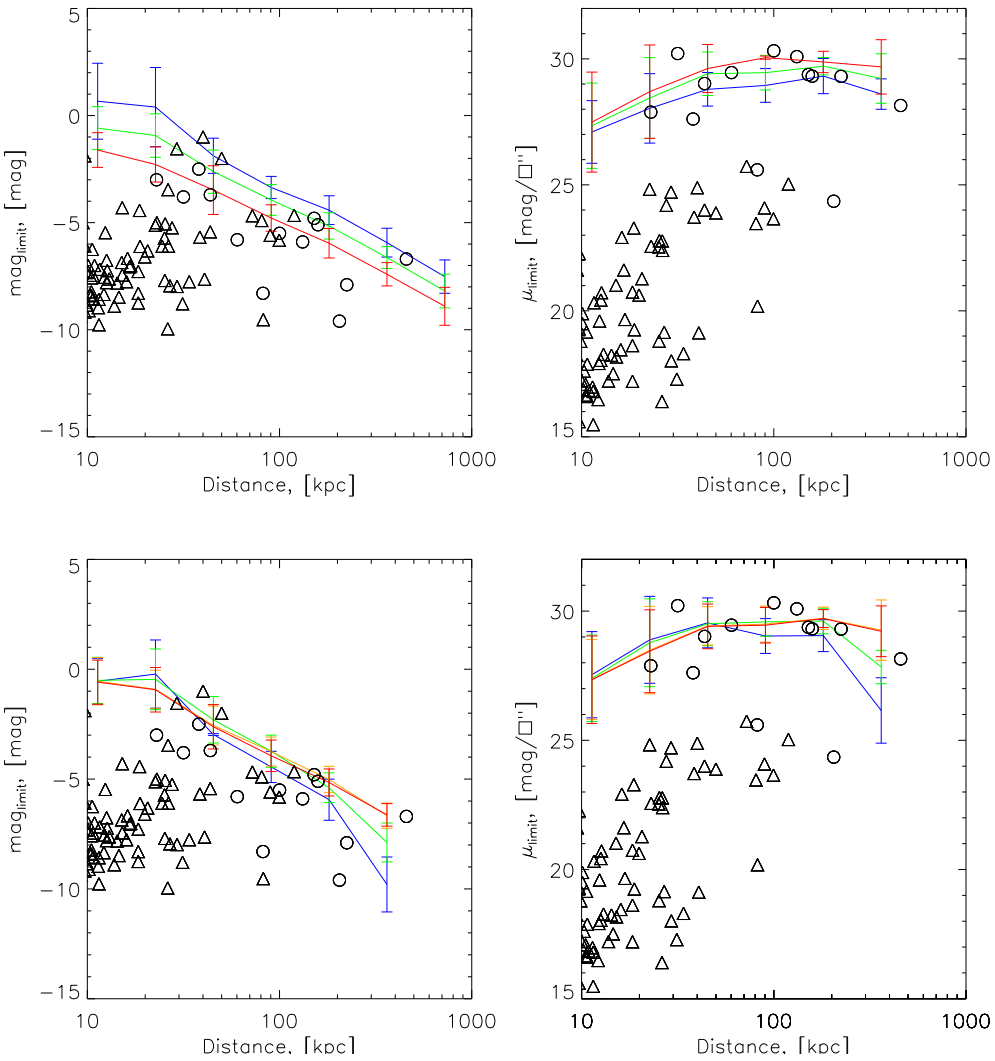

Figure 4.12: The known satellites and globular clusters shown in two-dimensional plots of Galactocentric distance versus absolute magnitude (left) and surface brightness (right). Circles mark the locations of the known dwarf galaxies, triangles the globular clusters. The error bars show either σ_M or σ_μ derived from our model fits (see Eq. 4.8). The detectability of the objects depends on their location relative to the limiting absolute magnitude (left) and surface brightness (right) as a function of Galactocentric distance for each kernel size/color cut employed in the search. Upper panels: The three lines show the detection limits for different sizes of the inner Gaussian in the kernel (blue – $2'$, green – $4'$, red – $8'$). Lower panels: The four lines show the detection limits for the different $g-r$ color cuts employed (black – 0.2, blue – 0.4, green – 0.6, orange – 0.9, red –1.2) and fixed kernel size of $4'$.

added to the DR5 stellar catalog. Figure 4.9 shows mock CMDs for simulated objects matching the recently discovered dwarf galaxies Canes Venatici I, Hercules and Ursa Major II (Belokurov et al., 2007c; Zucker et al., 2006a,b). These are good approximations to the observed CMDs of these objects.

In our simulations, we test several inner kernel sizes. The reason is that for a given distance, the kernel size gives rise to an optimum physical size of the detectable objects. For example, at a distance of 50 kpc, a kernel size of $4'$ corresponds to a physical size of $\simeq$60 pc. As we want our algorithm to be sensitive to objects of different sizes, we use three different inner kernel sizes, namely $\sigma_1 = 2'$, $4'$ and $8'$. An object is considered to be detected if it is above a threshold on the map convolved with at least one of the kernels (the threshold for the $2'$ kernel is 6.50, for the $4'$ kernel – 5.95 and for the $8'$ kernel – 6.00, see Section 4.3). We refer to this procedure as the combined kernel. This is equivalent to the algorithm used in the previous Section, because the list of detections for $2'$, $4'$ and $8'$ kernels includes all the known dwarfs.

Figure 4.10 shows two-dimensional efficiency maps as a function of luminosity and size in seven distance bins spanning the range 8 kpc to 1 Mpc. For Figure 4.10, we have used the color cut of $g - r < 1.2$ and the combined kernel, together with an outer kernel of size $\sigma_2 = 60'$. Black corresponds to zero detection efficiency, and white to unit efficiency. The locations of the known Milky Way globular clusters and dwarf galaxies in this parameter space are recorded as red triangles and circles. While a number of known objects lie well within the efficiency boundary, some of the recent discoveries lie close the boundary. It is evident that there is no steady gradient in efficiency, but rather a steep boundary between detectability and non-detectability. In fact, the primary contribution to the finite-extent of the gradient visible in the Figures is produced by the significant extent of the individual distance bins (the width of the distance bins is 0.3 dex). The pixel size in magnitude is 0.8, and in $\log r_{\rm h}$, it is 0.3. This means that there are typically 10 objects in each bin and so we expect moderate fluctuations due to shot noise.

As the efficiency changes so quickly near the boundary, and as several objects lie close to this zone, we carried out more detailed simulations on objects similar to the known dwarfs. We created 1000 Monte Carlo realizations of each of the known dwarfs, and fed them into the pipeline. Table 4.3 lists the derived detection efficiencies for

each object. The detection efficiencies are $\gtrsim 50\%$, with the sole exception of Boo II, confirming our assertion that the known satellites possess high detection probabilities.

For the regime in which objects are larger than the kernel size, some of the stars belonging to the satellite are missed by the window function, and for such objects the detectability is determined by the number of stars within the window function, i.e. the surface brightness. This effect produces the surface brightness limit seen in Figure 4.10. For objects smaller than the kernel size, all the stars are within the window function regardless of the size of the objects, therefore for such objects, the detectability doesn't depend on physical size, but depends only on the total number of stars, i.e. the luminosity. This effect produces the rapid change in detection efficiency at fixed absolute magnitude evident in Figure 4.10. These two regimes can be modeled with thresholds in surface brightness and absolute magnitude by adopting a functional form:

$$\epsilon(M_V, \mu) = G\left(\frac{M_V - M_{V,\mathrm{lim}}}{\sigma_M}\right) G\left(\frac{\mu - \mu_{\mathrm{lim}}}{\sigma_\mu}\right), \tag{4.8}$$

where G denotes the Gaussian integral, which is defined as

$$G(x) = \frac{1}{\sqrt{2\pi}} \int_x^\infty \exp(-t^2/2)dt. = \frac{1}{2}\, erfc\left(\frac{x}{\sqrt{2}}\right) \tag{4.9}$$

To describe the detectability in each distance bin, there are four parameters that are fitted – namely the detection thresholds in surface brightness μ_{lim} and absolute magnitude $M_{V,\mathrm{lim}}$, together with their widths σ_μ and σ_M. As an illustrative example, the grey-scale map of the efficiency function $\epsilon(M_V, \mu)$ from Eq. 4.8 is shown in Figure 4.11, with dashed lines indicating the thresholds. Note the shape of the detection boundary, with the prominent "knee", which corresponds to the boundary between the two detection regimes for objects of different sizes at fixed distance, as described above.

The two key parameters for the detection pipeline are the inner kernel size σ_1 and the color cut applied to the source catalogs. The top two panels of Figure 4.12 show the dependence of $M_{V,\mathrm{lim}}$ and μ_{lim} on distance, when convolved with the three different inner kernels. For a given kernel, the limiting magnitude declines roughly linearly with the logarithm of distance. Objects at the limiting magnitude have an apparent size that is smaller than the kernel size and their detection significance is reduced by the background contribution. Shrinking the kernel size removes some of the background and increases the significance of fainter satellites. The dependence of the $M_{V,\mathrm{lim}}$ and

$\mu_{\rm lim}$ on distance for the combined kernel is not plotted, because in the top left panel of Figure 4.12 the combined kernel basically follow the dependence of $2'$ kernel and in the top right panel of Figure 4.12 the combined kernel follow the dependence of $8'$ kernel. This is illustrated in the top left panel of Figure 4.12, where it is clear that a smaller kernel allows us to detect fainter objects. However, as the top right panel shows, this is at the expense of satellite size. Larger kernels pick up more stars from extended objects and hence reach fainter surface brightness. When combining different kernels in the pipeline, the overall limits in surface brightness and absolute magnitude ($2'$, $4'$, $8'$, see Section 4.3) can be approximated by the blue line in the top left panel of Figure 4.12 and the red line in the top right panel of Figure 4.12. Smaller kernels allow the detection of galaxies that are low in absolute magnitude, and larger kernels allow the detection of galaxies that are fainter in surface brightness. It is also reassuring to see that the error bars σ_M are of the same order as the difference in the limiting magnitude moving to a neighboring bin.

We explore the effects of changing color cuts and report the results in the bottom two panels of Figure 4.12. The color cut of $g - r < 0.4$ can improve slightly the magnitude limit for nearby objects by selecting turn-off stars. This improvement deteriorates rapidly as we exhaust the supply of turn-off stars. At larger distances, red color cuts like $g - r < 1.2$ are more efficient at picking up giant stars. The same effect explains the drop in $\mu_{\rm lim}$ and $M_{V,\rm lim}$ at large distances for bluish color cuts. Our choice of color cut $g - r < 1.2$ is conservative, mostly eliminating thin disk stars, and is, overall, the best-behaved and most robust. It also allows us to minimize the influence of metallicity and age changes in the stellar population of the satellites.

4.5 The Luminosity Function

4.5.1 Analysis of the detection efficiency maps

With an understanding of which satellite galaxies can be detected in SDSS DR5, together with our sample of actual detections, we can now estimate the luminosity function of faint Milky Way satellites. We start by re-examining the efficiency maps in Figure 4.10, where the locations of the known Milky Way globular clusters and dwarf galaxies are overplotted as red triangles and circles respectively. We can conclude that within the DR5 footprint there are certainly no bright satellites (either globulars or

Object	Efficiency
Bootes	1.00
Draco	1.00
Leo I	1.00
Leo II	1.00
SEGUE 1	1.00
Canes Venatici I	0.99
Willman I	0.99
Coma	0.97
Koposov 1	0.90
Leo IV	0.79
Ursa Major II	0.78
Leo T	0.76
Hercules	0.72
Ursa Major I	0.56
Koposov 2	0.48
Canes Venatici II	0.47
Boo II	0.20

Table 4.3: Detection efficiencies of simulated objects resembling known satellites.

Distance	$\mathbf{M_{V,lim}}$	$\mu_{\mathbf{lim}}$
kpc	mag	mag/$\Box''$
11	0.6	27.5
22	0.4	28.7
45	−1.9	29.6
90	−3.4	30.0
180	−4.4	29.9
260	−5.9	29.9
720	−7.5	29.6

Table 4.4: Limiting satellite absolute magnitude and surface nrightness as a function of distance

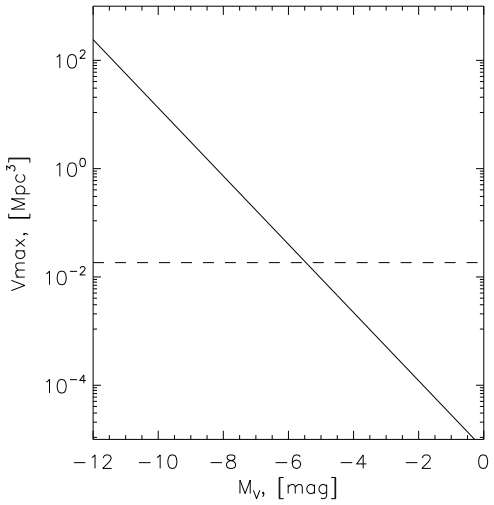

Figure 4.13: The accessible volume within the DR5 footprint for galaxies with different luminosities and surface brightnesses $\mu_{\rm lim}$, $\mu \lesssim 30\,{\rm mag}/\Box''$ (see Figure 4.12. The volume limited by the virial radius (280 kpc) and within DR5 is shown by the dashed line.

galaxies) nearby ($D < 32\,{\rm kpc}$) that have eluded discovery. However, the disrupting galaxy UMa II (Zucker et al., 2006a) provides a clue as to the likely locations of remnants. It is still possible that disrupted galaxies remain undiscovered nearby. They can lurk in the black portions of the uppermost two panels of Figure 4.10.

All that has survived in the inner Galaxy ($8 < D < 16\,{\rm kpc}$) is a population of globular clusters, which occupy a small region in the luminosity and size parameter space. They are predominantly old globular clusters belonging to the bulge. Only the densest survive against the disruptive effects of Galactic tides and shocking, which is illustrated by the apparent size bias. Notice that the datapoints lie well away from the detection boundary, suggesting that the sample is complete at least within $8 < D < 16\,{\rm kpc}$. Moving outwards ($16 < D < 32\,{\rm kpc}$), the globular clusters belong to the halo and may have been accreted (Mackey and Gilmore, 2004). Their size distribution is broader. Some of these objects are in the process of disruption, such as Pal 5 and NGC 5466 (Belokurov et al., 2006a; Dehnen et al., 2004; Fellhauer et al., 2007; Odenkirchen et al., 2001). The very faint and distant globular clusters discovered recently by Koposov et al. (2007b) are visible in the third panel of Figure 4.10 ($32 < D < 64\,{\rm kpc}$) right on the border of detectability. Further such sparse globulars may

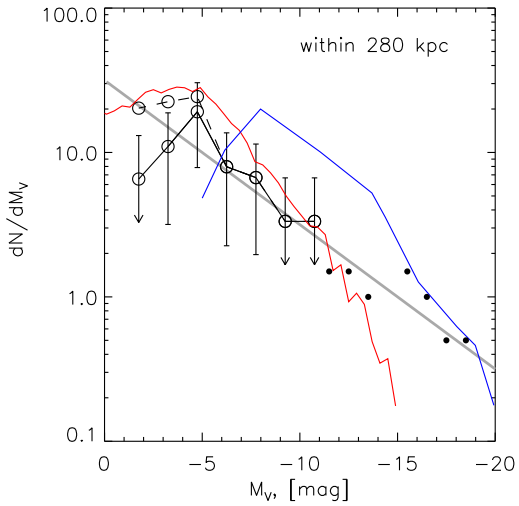

Figure 4.14: The luminosity functions of Milky Way satellite galaxies within ∼280 kpc (virial radius) inferred from our analysis under the assumption of two different radial distributions of satellites, NFW-like (solid black line) and isothermal (dashed black line). The calculation uses the satellite list and the volume correction factor obtained with the pipeline using the cuts $r < 22.5$ and $S_{\rm star} > 5.95$. The arrows on error bars indicate that there is only one galaxy in the particular bin, and so the Poisson error is formally 100%. The theoretical prediction of Figure 1 of Benson et al. (2002) is shown in a red line, and the prediction of Somerville (2002) for $z_{reion} = 10$ is shown as a blue line. Additionally, the luminosity function for the bright ($M_V < -11$) satellites of the Milky Way sampled over the whole sky together with the bright M31 satellites within 280 kpc from Metz and Kroupa (2007) is plotted with filled small symbols (the list of plotted objects consists of Sgr, LMC, SMC, Scu, For, LeoII, LeoI, M32, NGC 205, And I, NGC 147, And II, NGC 185, And VII, IC 10). The function $dN/dM_V = 10 \times 10^{0.1\,(M_V+5)}$ is shown in grey.

remain undetected.

Beyond 30 kpc, the dwarf spheroidals begin to appear. The long-known dwarfs such as Draco and Sculptor lie far from the boundary, in regions of the luminosity and size parameter space where the DR5 search efficiency is unity. However, all the recent SDSS discoveries, such as Canes Venatici I, Bootes and Hercules, lie close to the detection boundary, where the efficiency declines rapidly from unity to zero. Belokurov et al. (2007c) claimed that there is a paucity of objects with half-light radii between ~ 40 pc and ~ 100 pc. Our calculations support the idea that the gap is real and not produced by selection effects. If there were objects with radii between ~ 40 pc and ~ 100 pc, there is a broad range of parameter space in which they would have been found.

Although most of the new detections lie in the gray areas of the plot, the empty white regions with unit efficiency are telling us something important. There are swathes of the parameter space in which we would have detected objects if they existed. For example, there are very few bright objects ($M_V < -6$). The absence of detections of bright objects does by itself provide a strong constraint on the luminosity function of Milky Way satellites. There also do not appear to be any analogues of the extended, luminous star clusters found in M31 by Huxor et al. (2005). Although SDSS data may still contain evidence for further, hitherto unknown, dwarf galaxies, it is unlikely that their nature can be unambiguously established without substantial quantities of follow-up imaging. We emphasize that, since we never probe fainter than a certain surface brightness limit, an even larger population of very low surface brightness galaxies – which can not be detected with SDSS – may exist.

4.5.2 Estimation of the Luminosity function

Figure 4.13 shows the accessible volume for galaxies of different luminosities probed by our algorithm (which in practice is a function mostly of the luminosity) within the SDSS DR5 footprint. As the logarithm of distance scales roughly linearly with limiting magnitude (see Figure 4.12), so does the logarithm of the accessible volume. Using this, and the fact that the SDSS survey covers $\sim 1/5$ of the sky, we can convert the set of known objects into a volume corrected luminosity function[1].

[1]The existing data on the globular cluster population indicate that at least some globular clusters have complicated metallicity, age distributions and kinematics and may in fact be stripped nuclei of dwarf galaxies (Piotto et al., 2007; Zinnecker et al., 1988). The selection of such objects which

The observed luminosity function is constructed using all the well-established dwarf galaxies in DR5, namely Leo II, Draco, Leo I, CVn I, Boo I, Hercules, UMa II, Com, CVn II, Leo T, UMa I, Leo IV as well as the possible dwarf Willman 1. Segue 1 is not used because it is not in DR5 (Belokurov et al., 2007c), and Boo II is not used because it is not detected with our adopted identification-pipeline parameters. All the satellites included in our calculation have a surface brightness of at least 30 mag arcsec^{-2}. To relate the observed number of satellite galaxies in our sample to the total number of satellites in the Milky Way halo, it is necessary to adopt an underlying radial distribution of satellite galaxies (see Appendix A). In a given magnitude interval, we know the observed number of satellites within $V_{\rm max}(M_V)$ from Figure 4.13, together with their detection efficiencies from Table 4.3. If we assume a number density law $n(r)$ for the satellites, then its normalization at each magnitude interval can be fixed by integrating the density law out to $V_{\rm max}$. The total number of satellites within 280 kpc (the virial radius of the halo) is now the integral of the density law out to this limit. Figure 4.14 shows the results of the calculation for two such density laws. The dashed line shows the luminosity function assuming the satellites are distributed in an isothermal sphere (namely, $n(r) \propto 1/r^2$). The solid line shows the luminosity function if the density fall-off is steeper at large radii ($n(r) \propto 1/r^3$, analogous to Navarro-Frenk-White profile, although to prevent the $1/r^3$ profile from diverging in the MW center we use $n(r) \propto r^{-2}(r + r_{\rm c})^{-1}$ with the core radius $r_c = 10\,{\rm kpc}$). Of course, the nature of some of the objects we have included in the dwarf galaxy luminosity function is still uncertain – in particular, Willman 1 may be a globular cluster, although Martin et al. (2007) provide evidence for a metallicity spread and dark matter content. It is unclear whether Leo T should be included or excluded, as it is most likely a transition object with rather different properties from the other dwarf spheroidal galaxies in our sample. The error bars in Figure 4.14 are given by the square root of the number of datapoints in the absolute magnitude interval divided by the volume correction factor. At the bright end, the error bars are large, since we have only two objects with $M_V < -9$, namely Leo I ($M_V = -11.5$) and Leo II ($M_V = -9.6$). At the faint end, the error bars are also large because of the substantial volume correction factor. In Figure 4.14, we show the luminosity function for satellites within 280 kpc (a proxy for a Milky Way

are considered as dwarf galaxies is an additional source of uncertainty in any luminosity function determination.

virial radius (Benson et al., 2002; Klypin et al., 2002)). To define the bright end of the luminosity function, which cannot be reliably determined from our data since DR5 does not contain dwarfs brighter than $M_V \sim -11$, we have also included in Figure 4.14 the estimate of the luminosity function (filled points) for the bright satellites of the Milky Way sampled over the full sky, together with the bright M31 satellites within 280 kpc from Metz and Kroupa (2007). In Figure 4.14, we also overplot the power-law function $dN/dM_V = 10 \times 10^{0.1\,(M_V+5)}$, which approximates the datapoints in the range of $-19 < M_V < -2$ (with probably some flattening at $M_V \sim -4$). The integration of this power-law gives approximately 45 dwarfs brighter than -5.0, and 85 dwarfs brighter than -2.0.

There are a number of theoretical predictions of the luminosity function of the Local Group in the literature. For example, Somerville (2002) shows the results of semi-analytic galaxy formation calculations, including the effects of supernova feedback and photoionization. The luminosity function from Somerville (2002) for $z_{reion} = 10$ (Page et al., 2007) are plotted with blue line in Figure 4.14. Although the numbers of luminous satellites are in reasonable agreement with the data, the shape of the luminosity function is not. All Somerville's (2002) luminosity functions turn over at $M_V \approx -9$ or brighter, depending on the epoch of reionization, whereas the luminosity function derived in Figure 4.14 turns over fainter than $M_V \approx -5$, if at all. Therefore, Somerville's (2002) theoretical calculations overproduce Draco-like objects ($M_V \approx -10$) by a factor of a few, and underproduce much fainter galaxies like Boo ($M_V \approx -6$) by almost an order of magnitude.

Benson et al. (2002) also provides calculations of the luminosity function of the Milky Way satellites, including the effects of tidal disruption as well as photoionization. They report the luminosity functions for dwarfs with a range of of different central surface brightness cuts, namely $18, 20, 22, 24$ and 26 mag arcsec^{-2}, the last of which is plotted in Figure 4.14 in a red line. At first glance, the fit seems plausible, especially given the size of the error bars on the datapoints. The turn over in Benson et al.'s luminosity function is at $M_V \approx -3$ and the numbers of predicted satellites at faint magnitudes are also consistent given the uncertainties. However, Benson et al.'s model significantly underproduces the number of bright satellites. Additionally, Benson et al.'s satellites have a much higher central surface brightness – our SDSS survey corresponds to a surface brightness cut of ~ 30 mag arcsec^{-2}. Figure 2 of Benson et al. (2002)

does show the luminosity function for all objects, irrespective of surface brightness. Although there has been a large change in the luminosity function on moving from a detection threshold of 22 to 26 mag arcsec^{-2}, there is only a small change on moving from 26 to ∞ mag arcsec^{-2}.

4.6 Conclusions

There have been persistent discrepancies between the observed numbers of Milky Way satellites and the predictions from numerical simulations of galaxy formation for a number of years. Although here has been a cavalcade of discoveries of new Milky Way satellites using the SDSS over the last two years, a systematic search – with quantifiable detection limits and efficiencies – not been undertaken. In this chapter we have presented a quantitative search methodology for Milky Way satellite galaxies in SDSS data and have used this method to compute detection efficiency maps, which ultimately allow the construction of the satellite galaxy luminosity function.

In our method, the star count map is convolved with a family of kernels which are the difference of two Gaussians. Intuitively, this algorithm can be understood as constructing an estimate of the local stellar density minus the background. By attaching a statistical significance to the overdensities in the convolved image, this enables us to construct a ranked list of candidates. Although this idea is simple enough, its practical application is hampered by the fact that the separation between stars and galaxies by the SDSS pipeline becomes unreliable at magnitudes fainter than $r \simeq 22.5$. The resulting false positives must be removed by cross-correlating with galaxy catalogs. The significance threshold of peaks in our survey is set by requiring the detection pipeline to produce a "clean" list of Milky Way satellites.

To compute the detection efficiency, we create mock SDSS catalogs with stars from simulated dwarf galaxies and use Monte Carlo methods to estimate recovery as a function of satellite galaxy parameters and heliocentric distance. There is a sharp boundary between detectability and non-detectability. The efficiency maps make clear that there are large domains in parameter space in which objects would have been detected had they existed. In particular, even at heliocentric distances as great as 1 Mpc, objects brighter than $M_V \sim -8$ would have been detectable in SDSS. Similarly, populations of

extended, luminous star clusters would have been found in SDSS, if they existed in the Milky Way.

With the efficiency in hand, we can – for the first time – correct the observed luminosity function of the Milky Way satellites for selection effects and compute the true luminosity function. The number density of satellite galaxies continues to rise well below $M_V \sim -8^m$; depending on the radial distribution model assumed it may or may not flatten or turn over at $M_V \gtrsim -5$. Overall, the luminosity function of *all* Milky Way satellites may be reasonably well described by a power-law, $dN/dM_V = 10 \times 10^{0.1(M_V+5)}$ from $M_V = -2$ to -18. This power-law predicts ~ 45 satellites brighter than $M_V = -5$, and $\sim$85 satellites brighter than $M_V = -2$. The normalization of the luminosity function is in reasonable agreement with the predictions of semi-analytic modeling of galaxy formation, but the shape is not. There also remains a discrepancy in the distribution of surface brightnesses of such objects, in the sense that the semi-analytic models underproduce dwarfs with a central surface brightness fainter than 26 mag arcsec^{-2}.

5

A quantitative explanation of the observed population of Milky Way satellite galaxies.

This chapter reproduces the paper: S. Koposov, J. Yoo , H.-W. Rix, D. H. Weinberg, A. V. Macciò, J. Miralda-Escudé "The quantitative analysis of the observed population of Milky Way satellite galaxies.", published in ApJ, volume 696, page 2179-2194, May 2009.

5.1 Introduction

The inflationary cold dark matter scenario predicts an initial fluctuation spectrum with power that continues down to small scales, and in consequence it predicts a mass function of dark matter halos that rises steeply towards low masses. A significant fraction of these halos survive as gravitationally self-bound units long after falling into more massive halos. As pointed out forcefully by Klypin et al. (1999) and Moore et al. (1999), the predicted number of subhalos within a Milky Way-like galaxy halo greatly exceeded the then known numbers of Milky Way or Local Group dwarf satellites, when subhalos and observed dwarfs were matched based on velocity dispersion or corresponding circular velocity (see also Kauffmann et al., 1993). This discrepancy between predicted and observed numbers has become known as the "missing satellite problem."

5. A QUANTITATIVE EXPLANATION OF THE OBSERVED POPULATION OF MILKY WAY SATELLITE GALAXIES.

Proposed solutions fall into three general categories. The first modifies the properties of dark matter or the primordial fluctuations from inflation in a way that eliminates the low mass dark matter subhalos themselves (e.g. Bode et al., 2001; Kamionkowski and Liddle, 2000; Spergel and Steinhardt, 2000; Zentner and Bullock, 2003). The second appeals to astrophysical mechanisms that suppress star formation in low mass halos so that they do not become observable dwarf satellites; photo-heating by the meta-galactic UV background is an attractive mechanism because it naturally introduces a cutoff at approximately the correct velocity scale (Bullock et al., 2000; Kravtsov et al., 2004; Somerville, 2002). The third possibility, arguably a variant of the second, is that the numerous dwarf companions of the Milky Way actually exist but have been missed by observational searches.

In this chapter we revisit the "missing satellite problem" with particular emphasis on the role of the new dwarf companions discovered in imaging data from the Sloan Digital Sky Survey (SDSS; York et al. 2000; Adelman-McCarthy et al. 2008). There are now about a dozen of these (Belokurov et al. 2006b, 2007c; Irwin et al. 2007; Koposov et al. 2007b; Walsh et al. 2007; Willman et al. 2005b; Zucker et al. 2006b; a couple of systems still have ambiguous status), most of them at least an order of magnitude less luminous than the faintest of the previously known, "classical" satellites.[1] Spectroscopic follow-up (e.g. Geha et al., 2009; Martin et al., 2007; Simon and Geha, 2007) for many of them indicates that they are indeed dark matter dominated systems, even though most are fainter than typical globular clusters, as low as only $\sim$1000 $L_\odot$ (e.g. Belokurov et al., 2007c; Martin et al., 2008). Remarkably, almost all of the newly found faint satellite galaxies have stellar velocity dispersions in the range $3 - 10$ km s^{-1}, though their luminosities vary widely. Similarly, the total masses within the inner 300 pc span less than an order of magnitude (Strigari et al., 2008).

Since the SDSS imaging in which these satellites have been discovered covers only $\sim 20\%$ of the sky, a naive accounting would increase the estimated number of Milky Way companions by $5 \times 12 = 60$, in addition to the ten classical satellites. However, Koposov et al. (2008a) use a well-defined identification algorithm to show that the SDSS dwarfs are also subject to strong radial selection effects. Most of the newly discovered objects could only have been found within distances of 50-100 kpc, much

[1] Throughout the chapter we use "faint" and "bright" to refer to intrinsic luminosity rather than apparent brightness.

smaller than the inferred virial radius of the Milky Way's dark matter halo ($\sim 280\,\mathrm{kpc}$ for $\rho_{\rm vir}/\bar{\rho} = 340$; Xue et al. 2008). The faintest SDSS dwarfs are detectable over only 1/1000 of the halo virial volume (including the factor of five for sky coverage). Walsh et al. (2009) have recently reached similar conclusions based on an independent identification algorithm and independent Monte Carlo tests.

Such analyses are the basis for 'volume corrections' for the faint Milky Way satellite population. With proper volume corrections applied, the luminosity function of faint Milky Way satellite galaxies turns out to be a rather shallow power law in the range $-15 < \mathrm{M}_V < -3$ (Koposov et al., 2008a). These results in turn imply that the number of satellites brighter than $M_V = -3$ is ~ 80 or more, and the number above $M_V = 0$ could be a few hundred. Tollerud et al. (2008) reached a similar conclusion, adopting a radial satellite distribution based on the *Via Lactea* simulation of Diemand et al. (2007). Even this census counts only dwarfs that are above the effective surface brightness threshold for SDSS detection. With the Koposov et al. (2008a) detection algorithm, this threshold is approximately 30 mag arcsec^{-2} (V-band), with a weak dependence on luminosity and distance. The dwarfs found in SDSS have surface brightnesses that range from 24 to 30 mag arcsec^{-2}.

Studies of the high redshift Lyα forest indicate that the small scale power expected in the standard ΛCDM scenario (inflationary cold dark matter with a cosmological constant) is indeed present in the primordial fluctuation spectrum (Abazajian, 2006; Narayanan et al., 2000; Seljak et al., 2006; Viel et al., 2005). Astrophysical suppression of star formation, and photo-ionization suppression in particular, has emerged as the most plausible and hence popular solution to the "missing satellite" conundrum. Within this category, there have been different proposals about what subhalos host the observed dwarf satellites. Bullock et al. (2000) suggested that the observed dwarfs are those whose subhalos assembled a substantial fraction of their mass before reionization, and thus before the onset of photo-ionization suppression. Stoehr et al. (2002) suggested that the measured stellar velocity dispersions are well below the virial velocity dispersions of the dark matter subhalos, and that the observed dwarfs occupy subhalos that are still above the velocity threshold where star-formation suppression occurs. Kravtsov et al. (2004) used N-body simulations to show that roughly 10% of subhalos lose a large fraction ($\sim 90\%$) of their mass during dynamical evolution without being completely disrupted; they suggested that the observed dwarfs occupy subhalos that were above

the suppression threshold at the time they became satellites but have suffered extensive mass loss since then. These papers and others (e.g., Orban et al. 2008; Somerville 2002; Strigari et al. 2007) focus on explaining the classical (pre-SDSS) dwarf spheroidal population, with luminosities in the range $-8 < M_V < -15$ (excluding the Magellanic clouds) and stellar velocity dispersions in the range 8 km s^{-1} $< \sigma_* <$ 25 km s^{-1}. The recently discovered SDSS dwarfs have much lower luminosities ($-8 < M_V < -1.5$), lower surface brightness, and somewhat lower velocity dispersion ($\sigma_* \sim 5$ km s^{-1}), so they could have a distinct formation mechanism, or they could form a continuum with the classical dwarf spheroidals.

The new SDSS discoveries and their quantified detectability are the basis for the model-data comparison in this chapter. We construct and test models of the Milky Way dwarf satellite population that incorporate Monte Carlo realizations of merger trees for $10^{12} M_\odot$ (main galaxy) halos, a detailed analytic model for the dynamical evolution and disruption of subhalos, and a variety of recipes for assigning stellar masses to these subhalos motivated by ideas in the existing literature. For most of our models, we assume that a subhalo can only accrete gas to form stars (a) before the epoch of reionization or (b) after reionization if its virial velocity exceeds a critical threshold before it enters the Milky Way halo and becomes a satellite. The spirit of the exercise is similar to that of Bullock et al. (2000), but the dynamical modeling of subhalos is more sophisticated, and we are now in a position to include directly the (strong) constraints imposed by the SDSS dwarfs accounting for the radial selection function found by Koposov et al. (2008a). In contrast to most previous studies, we treat the luminosity distribution as the primary test of models, rather than the stellar velocity dispersions or central masses (Li et al., 2008; Macciò et al., 2009; Strigari et al., 2007, 2008), or the inferred but unobservable subhalo circular velocities. This emphasis is motivated by the fact that the luminosity is the foremost quantity that matters for the observational selection. We consider stellar velocity dispersions and central masses as an additional test, but their interpretations are affected by the uncertainty in the dark matter profiles of the subhalos associated with observed dwarfs.

5.2 The Population of Dark Matter Subhalos in the Milky Way

Our model for the Milky Way satellites is based on the cold dark matter scenario, with each satellite forming initially in a separate dark matter halo that at some point falls into the Milky Way's dark matter halo. We refer to the bound dark matter satellites orbiting in the Milky Way halo as subhalos. A subhalo may or may not correspond to a dwarf satellite galaxy, depending on whether it contains an observable number of stars. In this Section we describe our model for computing the dynamical evolution of subhalos.

We use the dynamical dark-matter-only model of subhalos developed by Yoo et al. (2007) to compute the subhalo population and its orbital distribution. This model is described in detail in Yoo et al. (2007), where a much larger halo of $10^{15}\,M_{\odot}$ was considered as a model of a massive cluster of galaxies. Here we consider instead a final halo of $10^{12}\,M_{\odot}$ at the present time as a representation of the Milky Way galaxy. Despite the change in the final halo mass, the model remains basically the same as described in Yoo et al. (2007), so here we make only a brief summary of its description.

The model uses the extended Press-Schechter formalism to generate a Monte Carlo merger tree of the parent halo at the present time (Bond et al., 1991; Press and Schechter, 1974). We follow the dynamical evolution of all the subhalos with masses $M_h > 10^6\,M_{\odot}$ until they merge with the Milky Way and lose their mass below $M_h = 10^5\,M_{\odot}$. All halos start as isolated objects, and they grow in mass by accretion and mergers for as long as they remain isolated. At some redshift, $z_{\rm sat}$, they merge into a larger halo (either the Milky Way or another object that will become a Milky Way subhalo). After this merger, the object has become a satellite or subhalo and it stops growing in mass. It can subsequently lose mass by tidal stripping when it passes near the center of its parent halo or undergoes encounters with other subhalos. The subhalo is subject to dynamical friction, which tends to shrink its orbit, and to random encounters with other subhalos, which on average expand the orbit. The orbital eccentricity is also subject to random variations. The model allows for the presence of subhalos within other subhalos. When a subhalo is disrupted, any subhalos it contained are dispersed into the new, larger parent halo. This simple analytic model is able to reproduce the subhalo mass function, in reasonably good agreement with that found in numerical

N-body simulations (Shaw et al., 2006; Yoo et al., 2007; Zentner et al., 2005). For the present purpose, this approach has the advantage (over N-body) of easily affording the required mass resolution and multiple halo realizations.

We adopt a flat ΛCDM cosmology with matter density $\Omega_m = 0.24$, baryon density $\Omega_b = 0.04$, power spectrum normalization $\sigma_8 = 0.8$, Hubble constant $h = 0.7$, and a primordial spectral index $n_s = 0.95$, consistent with recent measurements (Spergel et al. 2007; Tegmark et al. 2006). The matter power spectrum is computed by using the transfer function of Eisenstein and Hu (1999). We generate six Monte Carlo merger trees of a Milky-Way sized halo. Each realization provides the subhalo mass function, their orbital elements and density profiles at the present time. Our statistical results are the average of the six different realizations.

The dynamical model of Yoo et al. (2007) uses the Jaffe profile and its velocity dispersion to model subhalos and their dynamical interactions, for reasons of numerical simplicity and because large galaxies that are tidally-limited satellites of a larger halo are reasonably well modelled by a Jaffe sphere for their baryon plus dark matter density profiles. However, the very low-mass dwarf satellites tend to be dominated by dark matter even in their inner parts. We therefore make an adjustment to better connect our Monte Carlo simulation results to the observed Milky Way dwarf galaxies: we use the subhalo masses and orbital elements, which are the quantities most robustly computed in the Yoo et al. (2007) model, but we calculate the density profiles and velocity dispersions of subhalos assuming that they have an NFW profile (Navarro et al., 1997). Using the standard spherical collapse model, the virial radius of an isolated halo is assigned as

$$R_{\rm vir} = \left[\frac{3\,M_{\rm halo}}{4\,\pi\,\Delta_c\,\bar{\rho}_m(z)}\right]^{\frac{1}{3}} \quad , \tag{5.1}$$

where $\Delta_c = (18\,\pi^2 + 82\,x - 39\,x^2)/(1+x)$ (Bryan and Norman, 1998), $x = -(1-\Omega_m)/(\Omega_m(1+z)^3 + 1 - \Omega_m)$, and the mean cosmic density is $\bar{\rho}_m(z) = \Omega_m \rho_c (1+z)^3$. The halo concentration c is computed using the relation from Bullock et al. (2001a), scaled to $\sigma_8 = 0.8$ according to Macciò et al. (2007), with $c = 0.8 \times 9 \times \left(M_h/10^{13} h^{-1} M_\odot\right)^{-0.13}/(1+z)$.

For the model in this chapter, we use in particular the subhalo masses at two different special epochs: $M_{\rm rei} \equiv M_{\rm tot}(z = z_{\rm rei})$ when the universe reionizes and the

photo-ionization background starts to suppress the star formation efficiency in low mass halos, and $M_{\rm sat} \equiv M_{\rm tot}(z_{\rm sat})$ at the epoch when a halo merges into a larger halo and we presume that subsequent star formation and gas accretion is halted in the subhalo. We shall also use below the halo circular velocity $V_{\rm circ}$, which is the virial circular velocity, $V_{\rm circ} \equiv [(G\,M_{\rm tot})/R_{\rm vir}]^{1/2}$. (Here $M_{\rm tot}$ refers to the total mass including dark matter and a universal fraction of baryons.)

In Figure 5.1 we show the distribution of $\rm M_{subhalo}$ at redshifts $z = 0$ (left panel), $z = z_{\rm sat}$ (middle panel) and $z = 8$, 11, and 14 (right panel). As expected, the mass distribution is close to a power-law, except near the resolution limit of our simulations. Also, in Figure 5.2 we show the accretion history of the MW subhalo population, by plotting the halo masses of the present day MW subhalos at the time of accretion vs. the redshift at which they became satellites of larger halos. We see that most of the MW subhalos became satellites at $z < 2$. Most of the accreted satellites have small circular velocities $V_{\rm circ} < 20$ km s^{-1}, so they lie in a range where gas accretion and star formation are likely to be suppressed after the epoch of reionization (Bullock et al., 2000; Quinn et al., 1996; Thoul and Weinberg, 1996).

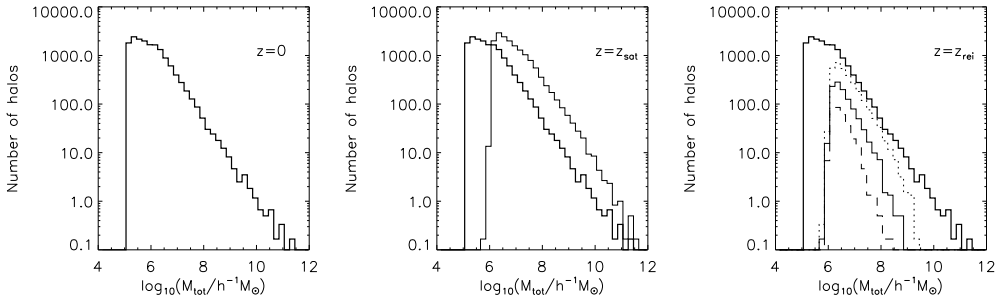

Figure 5.1: Mass distribution of dark matter subhalos at different epochs. *Left panel*: The present-day ($z = 0$) mass function of subhalos within a Milky Way-like halo. This histogram is repeated in the other two panels for reference. *Middle panel*: Distribution of mass that present-day subhalos had at $z = z_{\rm sat}$, the epoch at which they became a satellite within a larger halo (*thin line*); tidal stripping of satellite halos is manifesting important. *Right panel*: Mass distribution of present day MW subhalos at the epoch of reionization, for $z_{\rm rei} = 8$ (*dotted*), 11 (*thin solid*), and 14 (*dashed*). All panels reflect the average of six different realizations of MW-like halos. The flattening below $M = 10^6\,h^{-1}M_\odot$ and the sharp cut-off at $M = 10^5\,h^{-1}M_\odot$ arise from the mass resolution limits of our simulations.

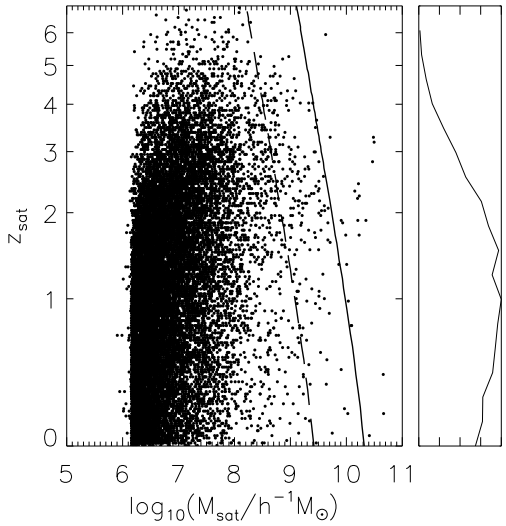

Figure 5.2: Epochs when (sub-)halos were accreted into larger halos, and masses at that time. This Figure illustrates the results from one Monte-Carlo realization of the semi-analytic model, with each point showing the redshift $z_{\rm sat}$ at which a subhalo first became a satellite in a larger halo against its total mass $M_{\rm sat}$ at that epoch. The small panel on the right shows the distribution of $z_{\rm sat}$. Solid and dashed lines show the locus of halos with $V_{\rm circ}(z_{\rm sat}) = 40$ km s^{-1} and 20 km s^{-1}, respectively.

5.3 Populating the DM halos with Stars

5.3.1 Recipes to assign stellar masses to subhalos

To make direct observational predictions from these models, we populate each subhalo in a given Monte-Carlo realization with stars according to a sequence of recipes, then test how many of these satellites could have been found within the SDSS. Some of these recipes are mathematically simple illustrations, while others are motivated by the expected effects of ionization and cooling physics as discussed in the introduction. For reference, the nomenclature of the recipes is summarized in Table 5.1. In all cases we calculate the stellar mass based on the subhalo mass (dark matter plus baryons in the universal fraction) at the accretion epoch $z_{\rm sat}$, denoted $M_{\rm sat}$. We implicitly assume that satellites do not accrete new material to form additional stars and that tidal stripping of the dark matter does not affect the stellar content of the satellite if it survives to the present day. Simulations suggest that these assumptions are reasonable but not perfect approximations (Peñarrubia et al., 2008; Simha et al., 2008).

We begin with the simplest model (denoted Model 1A), that the stellar mass is a constant fraction of the subhalo mass at the time of accretion into the main halo:

$$M_* = f_* \times M_{\rm sat}. \tag{5.2}$$

The arguments of Klypin et al. (1999) and Moore et al. (1999) suggest that this model will fail badly, and we show that it does indeed fail despite the new satellite discoveries and the radial selection biases that affect them. There is ample evidence that the efficiency of star formation declines rapidly towards low masses even well above the dwarf satellite regime (e.g., van den Bosch et al. 2007). In Model 1B, we allow the stellar fraction to vary as a power law of $M_{\rm sat}$ below a threshold M_0:

$$M_* = f_* \times \mathtt{min}\left(\left(\frac{M_{\rm sat}}{M_0}\right)^{\alpha}, 1\right) \times M_{\rm sat}\ . \tag{5.3}$$

Our second approach to modeling stellar masses includes the effects of a pervasive energetic radiation field after the epoch of reionization, which heats gas and hence keeps it from accumulating at the centers of low-mass halos. Calculations by Quinn et al. (1996) and Thoul and Weinberg (1996) showed that gas accretion in halos with the circular velocities below $V_{\rm circ} \sim 30 - 40$ km s^{-1} is strongly suppressed, while substantially larger halos are minimally affected (see also Gnedin 2000; Weinberg et al. 1997). In

this spirit, we assume that halos below a critical circular velocity form no stars after reionization, and we thus assign stellar masses

$$M_* = \begin{cases} f_* \times M_{\rm sat} & \text{if } V_{\rm circ}(z_{\rm sat}) > V_{\rm crit} \\ f_* \times M_{\rm rei} & \text{if } V_{\rm circ}(z_{\rm sat}) < V_{\rm crit}. \end{cases} \tag{5.4}$$

This model (Model 2) has three adjustable parameters — f_*, $V_{\rm crit}$, and $z_{\rm rei}$ — with expectations that $V_{\rm crit} \sim 20 - 40$ km s^{-1} and $z_{\rm rei} \sim 11$ (e.g. Dunkley et al., 2009; Weinmann et al., 2007). The approach is similar to that of Bullock et al. (2000), except that we treat $V_{\rm crit}$ as free parameter, and the stellar mass formed before the epoch of reionization is assigned using $M_* = f_* \times M_{\rm rei}$, instead of simply dividing galaxies into "observable" or "unobservable" classes based on the fraction of the mass accreted by $z_{\rm rei}$.

Our third class of models is similar to the second, but it replaces the sharp threshold of equation (5.4) with the continuous transition found in numerical simulations by Gnedin (2000), Hoeft et al. (2006), and Okamoto et al. (2008). The numerical results in these papers can be described fairly well by a formula similar to that in Gnedin (2000), with the fraction of baryons that cool in low mass halos suppressed by a factor $[1+0.26(V_{\rm crit}/V_{\rm circ})^3]^{-3}$; well after the reionization redshift, the critical velocity is found to be approximately independent of redshift. Gnedin (2000) found $V_{\rm crit} \sim 40$ km s^{-1}, but these results were artificially affected by numerical resolution (N. Gnedin, private communication). Hoeft et al. (2006) and Okamoto et al. (2008) find $V_{\rm crit} \sim 25 - 30$ km s^{-1}. Including the pre-reionization contribution to M_*, this model (Model 3A) becomes

$$M_* = \frac{f_* \times (M_{\rm sat} - M_{\rm rei})}{(1 + 0.26\,(V_{\rm crit}/V_{\rm circ}(z_{\rm sat}))^3)^3} + f_* \times M_{\rm rei}\ . \tag{5.5}$$

The assumption that all halos can form stars before $z_{\rm rei}$ may not be justified because in halos with virial temperature $T_{\rm vir} \lesssim 10^4$ K ($V_{\rm circ} \lesssim 10$ km s^{-1}) the gas does not get hot enough to cool by atomic processes, and simulations that include molecular cooling suggest that gas cooling and star formation is very inefficient in such halos (Barkana and Loeb, 1999; Bovill and Ricotti, 2009; Haiman et al., 1997; Machacek et al., 2001; O'Shea and Norman, 2008; Wise and Abel, 2007). We will therefore consider variant models (Model 3B) that eliminate stellar mass in pre-reionization halos below a critical

threshold $V_{\rm crit,r} \sim 10$ km s^{-1}.[1] In Model 3B, halos with $V_{\rm circ}(z_{\rm rei}) < V_{\rm crit,r}$ have stellar mass

$$M_* = \frac{f_* \times M_{\rm sat}}{(1 + 0.26\,(V_{\rm crit}/V_{\rm circ}(z_{\rm sat}))^3)^3}\ , \tag{5.6}$$

while halos with $V_{\rm circ}(z_{\rm rei}) > V_{\rm crit,r}$ have mass given by equation (5.5).

To determine very roughly the plausible range of values for the stellar mass fraction f_*, we can refer to the results of Strigari et al. (2007), who derived $M(< r_{\rm tidal})/L) = 30 - 800 M_\odot/L_\odot$ for the classical dwarfs, and Simon and Geha (2007), who measured velocity dispersions for SDSS dwarfs and inferred total mass-to-light ratios of $140 - 1800 M_\odot/L_\odot$. For a stellar mass-to-light ratio $M_*/L_V = 1 M_\odot/L_\odot$, we infer plausible values of $f_* \sim 10^{-4} - 10^{-2}$, though these are very uncertain because all the dynamical mass-to-light ratio determinations suffer from the fact that the stars in luminous bodies of the dSphs probe only the inner parts of the dark matter potential wells. Another line of argument comes from matching the mean space density of dark matter halos to that of observed *field* dwarfs: Tinker and Conroy (2009) find $f_* \approx 10^{-3.6}$ at absolute magnitude $M_r \approx -10$. In the rest of the chapter, we will frequently refer to the stellar mass fraction normalized by the universal baryon fraction:

$$F_* \equiv \frac{f_*}{\Omega_b/\Omega_m} = 6.25 f_*. \tag{5.7}$$

Note that f_* and F_* refer to stellar fractions in halos where the efficiency is *not* suppressed, i.e., $V_{\rm circ}(z_{\rm sat}) > V_{\rm crit}$. We will frequently refer to the quantity $(M_*/M_{\rm sat}) \times (\Omega_m/\Omega_b)$ as the "star formation efficiency," by which we mean the efficiency with which the halo converted the baryons available to it at $z_{\rm sat}$ (for a universal baryon fraction) into stars observable at $z = 0$.

5.3.2 Detectability and observable properties for the simulated satellites

velocity

Color-magnitude diagrams for the faint dwarf spheroidal galaxies in the Milky Way halo show that the stellar populations are predominantly 'old' (older than several Gyrs) and metal poor ([Fe/H]$\lesssim -1$). To convert stellar masses to luminosities, we assume

[1] We will refer to these as models with "pre-reionization suppression," but this simply means that halos with $V_{\rm circ}(z_{\rm rei})$ below a critical threshold form stars with very low efficiency (too low to produce observable satellites), most likely because of inefficient cooling rather than active feedback.

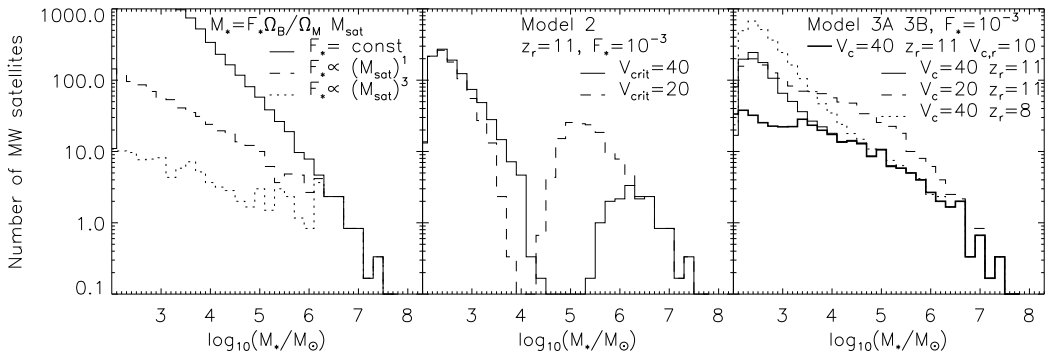

Figure 5.3: Predicted stellar mass functions of all satellites within the MW's virial radius (280 kpc), for a variety of models. *Left panel*: The solid, dotted, and dashed lines represent, respectively, Model 1A with $F_* = 10^{-3}$ and Model 1B with $(F_*, M_0, \alpha) = (10^{-3}, 10^{10}\,M_\odot, 1)$ and $(10^{-3}, 10^{10}\,M_\odot, 2)$. *Middle panel*: The two curves show predictions of Model 2, with $F_* = 10^{-3}$, $z_{\rm rei} = 11$, and $V_{\rm crit} = 40$ km s^{-1} (*solid*), and $V_{\rm crit} = 20$ km s^{-1} (*dashed*). *Right panel*: Thin solid, dashed, and dotted lines represent Model 3A with $(F_*, V_{\rm crit}, z_{\rm rei}) = (10^{-3}, 40\text{ km s}^{-1}, 11)$, $(10^{-3}, 30\text{ km s}^{-1}, 11)$, and $(10^{-3}, 40\text{ km s}^{-1}, 8)$, respectively. The thick solid curve shows model 3B with $F_* = 10^{-3}$, $V_{\rm crit} = 40$ km s^{-1}, $z_{\rm rei} = 11$, and $V_{\rm crit,r} = 10$ km s^{-1}. All curves reflect the average of six realizations of MW halos. These are the predicted *complete* satellite (stellar) mass functions, with no radial or sky coverage selection effects.

Model Name	**Present-Epoch Stellar Mass**
1A	$M_* = f_* \times M_{\rm sat}$
1B	$M_* = f_* \times \mathtt{min}((M_{\rm sat}/M_0)^\alpha, 1) \times M_{\rm sat}$
2	$M_* = \begin{cases} f_* \times M_{\rm sat} & \text{if } V_{\rm circ}(z_{\rm sat}) > V_{\rm crit} \\ f_* \times M_{\rm rei} & \text{if } V_{\rm circ}(z_{\rm sat}) < V_{\rm crit} \end{cases}$
3A	$M_* = \frac{f_* \times (M_{\rm sat} - M_{\rm rei})}{(1+0.26\,(V_{\rm crit}/V_{\rm circ})^3)^3} + f_* \times M_{\rm rei}$
3B	same as 3A for halos with $V_{\rm circ}(z_{\rm rei}) > V_{\rm crit,r}$, for halos with $V_{\rm circ}(z_{\rm rei}) < V_{\rm crit,r}$ $M_* = \frac{f_* \times M_{\rm sat}}{(1+0.26\,(V_{\rm crit}/V_{\rm circ})^3)^3}$

Table 5.1: List of models used

that all of our model dwarfs have a stellar mass-to-light ratio $M_*/L_V \approx 1 M_\odot/L_\odot$ appropriate to an old, metal poor population (Bruzual and Charlot, 2003; Martin et al., 2008). The light of the lowest luminosity dwarfs can be dominated by a handful of bright stars and thus subject to stochastic variations. We ignore this complication; our "luminosities" are simply scaled stellar masses: $L_V/L_\odot = M_*/M_\odot$. This seems appropriate, since the luminosities of the dwarfs galaxies are usually measured either by integrating over the luminosity function of old stellar population matched to the observed luminosity function of stars in dwarfs(Belokurov et al., 2006b) or by averaging over possible stochastic variations of galaxy luminosity(Martin et al., 2008).

The detectability of a faint stellar MW satellite galaxy in an SDSS-like search depends on its luminosity and its distance from the Sun, as quantified by Koposov et al. (2008a) (see also Walsh et al., 2009). On the basis of these results (Figure 12 of Koposov et al. 2008a) we model the detectability of each simulated satellite as a binary decision using the criterion

$$\log_{10}(D_\odot/1\,\mathrm{kpc}) < 1.1 - 0.228 M_V \tag{5.8}$$

Our simulations provide the current Galactocentric distance and orbital apocenter and pericenter for each subhalo, but not the orientation of the orbit. We therefore assign the heliocentric distance of the satellites

$$D_\odot = \sqrt{8.5^2 + D_{GC}^2 - 2 \times 8.5 \times D_{GC} \cos(\phi)}\ , \tag{5.9}$$

where D_{GC} is the Galactocentric distance (in kpc) from the simulations and $\cos(\phi)$ is a random variable uniformly distributed between -1 and 1 (ϕ is the angle between radial vectors from the GC to the Sun and to the subhalo). This method assumes that the satellite orbits are isotropically distributed across the sky (see Tollerud et al., 2008, for discussion of the validity of this approximation). As expected from Koposov et al. (2008a), accounting for the detectability of satellites causes the 'observable' population to differ strongly from the 'simulated' one; only the brightest satellites are observable throughout the virial volume.

Not surprisingly, the Koposov et al. (2008a) analysis also reveals a surface brightness threshold for dwarf detection, which is approximately 30 mag arcsec^{-2} with little dependence on distance. We assume that any model dwarf that passes the luminosity

threshold also passes the surface brightness threshold. Many recent SDSS satellite discoveries do lie near that survey's surface brightness limit; this assumption can therefore only be tested with the next generation of sky surveys. We discuss implications of this assumption in §5.5.

With a model that assigns stellar luminosities to each satellite halo, we can predict the expected stellar velocity dispersions for comparison with those measured for MW satellites by Walker et al. (2007), Simon and Geha (2007), and Martin et al. (2007). This can be done straightforwardly if we assume that the stars are test particles — an assumption supported by the observed $(M/L)_{\rm dyn}(< R_{\rm eff}) \gg (M/L)_*(< R_{\rm eff})$ — orbiting in an NFW potential with an isotropic velocity dispersion. Then we can use the Jeans equation (Jeans, 1919) to derive the velocity dispersion profile of stars:

$$\frac{d(\nu(r)\,\sigma^2(r))}{d\,r} + \nu(r)\,\frac{G\,M(r)}{r^2} = 0, \tag{5.10}$$

where ν is the density distribution of stars (see Strigari et al. 2007 for more detailed treatment). Here we assume that the density of stars follows a Plummer profile $\nu \propto [1+(r/r_p)^2]^{-2}$ (Plummer, 1911), which seems to fit observed density profiles reasonably well (Belokurov et al., 2007c; Wilkinson et al., 2002). The mass profile $M(r)$ used here is computed based on the virial radii and concentrations at the redshift $z_{\rm sat}$ of subhalo accretion. While the outer parts of the subhalos are tidally stripped, Peñarrubia et al. (2008) show that the stars and the inner part of the dark matter subhalo are stripped only at a very late stage, when the subhalo is close to complete disruption. They also show that the velocity dispersion in subhalos is a function of the total dark matter mass remaining bound inside the luminous body and therefore remains nearly constant until this late stage.

After numerically solving the Jeans Equation, we compute the expected light-weighted velocity dispersion within the optical radius as

$$\sigma_* = \frac{\int \nu(r)\sigma(r)\,dx\,dy\,dz}{\int \nu(r)\,dx\,dy\,dz}, \tag{5.11}$$

where the integration is done over a cylinder within a radius, $R = \sqrt{x^2+y^2}$ equal to the Plummer radius of the galaxy; the integral extends over $\pm\infty$ in z. The stellar velocity dispersion depends on the radial extent of the stellar tracers, which cannot be predicted within our simple modeling context (see also Benson et al., 2002). We

therefore use the *observed* properties of the faint Milky Way satellites to choose stellar radii, based on Martin et al. (2008). Specifically, we adopt Plummer radii $r_p = 150\,\mathrm{pc}$ for $M_V < -5$, and for fainter dwarfs we adopt a linear relation between $\log r_p$ and M_V with r_p rising from 20 pc at $M_V = 0$ to 150 pc at $M_V = -5$.

The additional important component of the detectability is the tidal disruption of the satellite galaxies. Although our semi-analytic model of dark matter subhalo evolution properly accounts for the tidal disruption of subhalos, it does not allow for the possibility that stars have been dispersed in a tidal stream while a small core of the subhalo survives. Here we simply classify a subhalo as unobservable if its current tidal radius is less than the expected Plummer radius of the stellar body, which would imply substantial tidal disruption of the stellar component. We also presume that a satellite is unobservable if its host subhalo has lost more than 99% of its original mass to tidal stripping.

5.4 Results

5.4.1 Stellar mass function of the full satellite populations

Figure 5.3 shows the predicted distribution of the *stellar* masses of satellites within $\mathrm{R_{virial}} = 280\,\mathrm{kpc}$, assuming 4π sky coverage and complete satellite detectability. In the left panel, the solid curve shows Model 1A with a constant $F_* = 10^{-3}$, making the stellar mass function a scaled version of the dark matter subhalo mass function. Introducing mass-dependent suppression, Model 1B with $\alpha = 1$ (dashed) and $\alpha = 2$ (dotted) lowers the low mass end of the stellar mass function as expected. Since this model also adopts $F_* = 10^{-3} = \text{const.}$ above $M_{\mathrm{sat}} = M_0 = 10^{10} M_\odot$, the high mass end of the mass function is unchanged.

The middle panel of Figure 5.3 shows Model 2, with post-reionization suppression of star formation in halos below a sharp circular velocity threshold, either $V_{\mathrm{crit}} = 40\ \mathrm{km\ s^{-1}}$ (solid) or $V_{\mathrm{crit}} = 20\ \mathrm{km\ s^{-1}}$ (dashed), where we have adopted $F_* = 10^{-3}$ and a reionization redshift $z_{\mathrm{rei}} = 11$. The resulting stellar mass functions for the satellite galaxies are strongly bimodal, with the low mass portion corresponding to dwarfs in which all stars formed before reionization and the high mass portion corresponding to halos that exceeded the critical velocity threshold before becoming satellites, $V_{\mathrm{circ}}(z_{\mathrm{sat}}) > V_{\mathrm{crit}}$. The low mass portion is just a scaled version of the subhalo mass

function at $z = z_{\rm rei}$. Above $M_* \approx 10^{6.5} M_\odot$ the host halos are all massive enough to have star formation after $z_{\rm rei}$, and the mass function is the same as that of Model 1. If the velocity threshold is lowered to $V_{\rm crit} = 20$ km s^{-1}, the high mass peak in the distribution of satellite stellar masses extends to lower values before photo-ionization suppression cuts it off.

The bimodal appearance of the middle panel of Figure 5.3 is a direct consequence of the sharp $V_{\rm circ}$ threshold for photo-ionization suppression. The right hand panel shows predictions for several variants of Model 3A and 3B, with the Gnedin (2000) formula (Eq. 5.5) used to describe photo-ionization suppression. With this smooth suppression, the "pre-reionization" and "post-reionization" portions of the mass function join to make a smooth overall mass function. The low mass end of the mass function is now a mix of satellites that formed their stars before reionization and satellites with $V_{\rm circ}(z_{\rm sat}) < V_{\rm crit}$ whose post-reionization star formation was strongly suppressed but not completely eliminated. Lowering the assumed reionization redshift from $z_{\rm rei} = 11$ to $z_{\rm rei} = 8$ boosts the stellar mass function below $M_* = 10^4 M_\odot$. Conversely, if we eliminate pre-reionization SF in dwarfs with $V_{\rm circ}(z_{\rm rei}) < V_{\rm crit,r} = 10$ km s^{-1} (thick solid line, Model 3B), the number of satellites with $M_* \leq 10^3 M_\odot$ drops by a large factor, while at higher masses the stellar mass function is unaffected. The difference between the thin and thick solid lines is the contribution of satellites that formed stars primarily before reionization in halos with $V_{\rm circ}(z_{\rm rei}) < 10$ km s^{-1}, for $z_{\rm rei} = 11$ and $V_{\rm crit} = 40$ km s^{-1}.

5.4.2 Distribution of observed dwarf satellite luminosities, $N(M_V)$

Figure 5.4 illustrates the impact of selection effects on the observable satellite population. For one realization of Model 3B (with parameters that yield a good match to observations), filled circles show satellites that would be detectable in an all-sky, SDSS-like survey (Koposov et al., 2008a), and open circles show un-detectable satellites. The low end of the luminosity distribution, with $M_V \gtrsim -5$, is strongly affected by the radial selection bias.

For direct comparison with observations, we therefore select only those model satellites whose combination of luminosity and distance would make them detectable. At the bright end, $M_V < -11$, we assume that existing photographic surveys are complete to $D_\odot = 280$ kpc, and we thus compare the total number of dwarfs across the

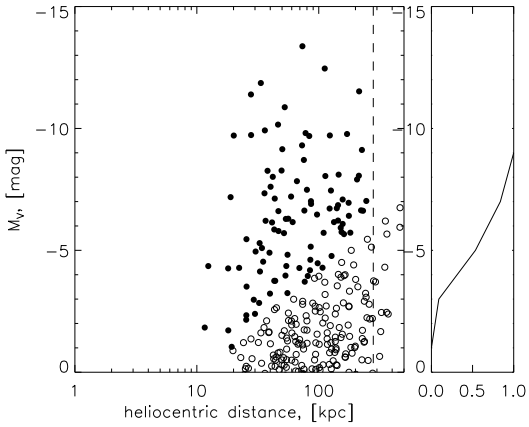

Figure 5.4: Detectability of the satellite galaxies predicted by our fiducial model (Model 3B), as a function of their heliocentric distance and stellar luminosity. Filled circles denote galaxies that can be detected with SDSS-like all-sky surveys, and empty circles denote those that cannot. The dashed line marks the approximate virial radius of the MW's dark matter halo; we will compare all model predictions to the observed MW satellite population only within this radius. The galaxies shown were taken from one Monte-Carlo realization of Model 3B with $(V_{\rm crit}, F_*, z_{\rm rei}, V_{\rm crit,r}) = (35 \text{ km s}^{-1}, 10^{-3}, 11, 10 \text{ km s}^{-1})$. The right panel shows the fraction of detectable galaxies as a function of luminosity.

whole sky to the total population of satellites within the virial radius in the simulation. For $M_V \geq -11$, we randomly select 1/5 of the model galaxies to mimic the 20% sky coverage of SDSS DR5, and we count only those satellites that would be detectable according to the criteria of Koposov et al. (2008a). We focus our data-model comparison on $N_{\rm obs}(M_V)$, the luminosity distribution of known MW satellites. We look at additional tests against stellar velocity dispersions, central masses, and the heliocentric radial distribution in § 5.4.3.

The luminosities, distances, and velocity dispersions of the observed Milky Way satellites that we use in all subsequent model - data comparisons were taken from various authors (Martin et al., 2008; Mateo, 1998; Metz and Kroupa, 2007) and are compiled in Table 5.2. The sample of SDSS satellites used here consists of those systems above the 50% completeness limits of Koposov et al. (2008a). We do not include two systems, Boo II and Leo V (Belokurov et al., 2008; Walsh et al., 2007), which do not formally satisfy the very conservative selection limits from Koposov et al. (2008a). These limits were chosen to avoid the issue of significant 'false positive' detections, at

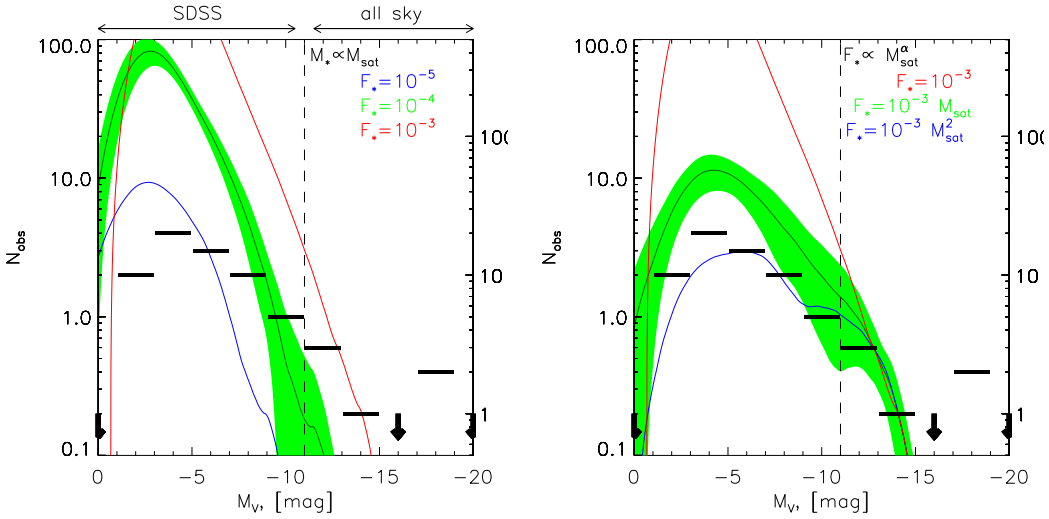

Figure 5.5: Model predictions for the observed satellite population, $N_{\rm obs}(M_V)$, including radial selection effects for the SDSS dwarfs. Horizontal bars show the number of currently known satellites (Table 2) in 2-magnitude bins; empty bins are plotted with an arrow. The SDSS and classical dwarfs are separated by the vertical line at $M_V = -11$; note that the y-axes for these two populations differ by a factor of five so that the model predictions (which incorporate a factor of 1/5 below $M_V = -11$ to account for SDSS sky coverage) are continuous across the boundary. *Left Panel:* Predictions of Model 1A, with $M_* \propto M_{\rm sat}$, for three values of F_*. For $F_* = 10^{-4}$, the green band shows the bin-by-bin $\pm 1\sigma$ range of the predictions from multiple realizations; the logarithmic width of this band is similar for other models. Model curves have been slightly smoothed with a polynomial filter. *Right Panel:* Comparison of Model 1A (red curve) to Model 1B, where the stellar mass fraction in halos with $M_{\rm sat} < 10^{10} M_\odot$ is is $F_* \propto M_{\rm sat}^\alpha$, with $\alpha = 1$ (green band) or $\alpha = 2$ (blue curve).

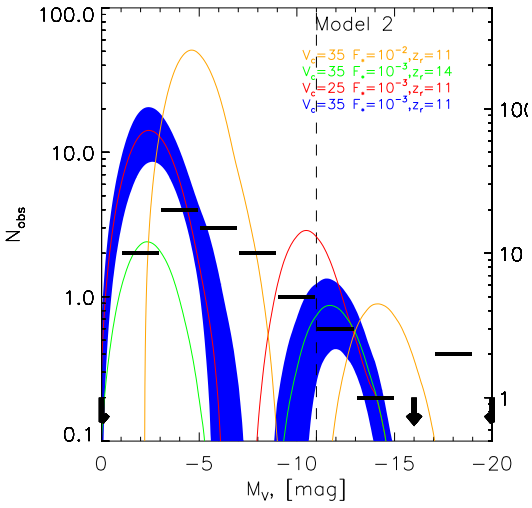

Figure 5.6: Predictions for Model 2, in which post-reionization star formation is sharply suppressed below a critical velocity $V_{\rm crit}$, in the same format as Figure 5.5. Blue, red, green, and orange curves/bands show the parameter combinations $(F_*, V_{\rm crit}, z_{\rm rei}) = (10^{-3}, 35\ {\rm km\ s^{-1}}, 11)$, $(10^{-3}, 25\ {\rm km\ s^{-1}}, 11)$, $(10^{-3}, 35\ {\rm km\ s^{-1}}, 14)$, and $(10^{-2}, 35\ {\rm km\ s^{-1}}, 11)$, respectively. This class of models predicts a bimodal distribution of satellite luminosities, with the faint portion ($M_V > -8$) coming entirely from pre-reionization star formation. The predicted $N(M_{\rm V})$ differs grossly from the observations.

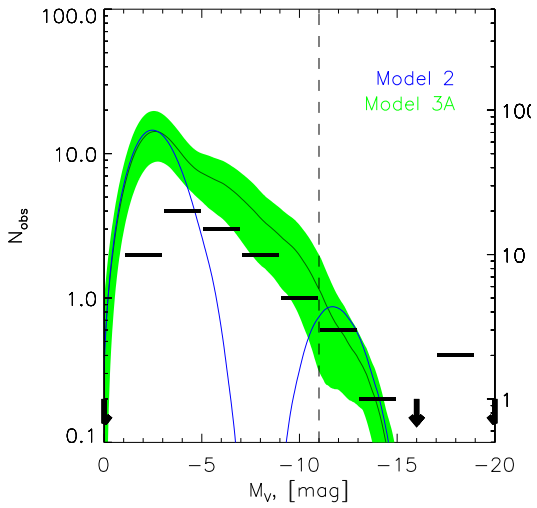

Figure 5.7: Comparison of Model 2 and Model 3A, both with parameters $F_* = 10^{-3}$, $V_{\rm crit} = 35$ km s^{-1}, and $z_{\rm rei} = 11$, in the same format as Figure 5.5. Switching to the continuous prescription for photo-ionization suppression fills in the gap between the two peaks of Model 2, while leaving the predictions at the highest and lowest luminosities unchanged.

the expense of leaving out 2 objects that deeper follow-up found to be 'real'. For the analysis presented here it is most important that the *same* selection criteria are applied to the mock satellite observations and the SDSS data. As our analysis subsequently shows, such a small difference in sample size is smaller than the model halo to halo variation of number of galaxies. Therefore the inclusion of omission of these two objects does not affect our results significantly.

Anyway, as we will see later, the halo to halo variation of number of galaxies in our models is noticeable, so we believe that the fact that we do not include two galaxies should not affect our results significantly.

The left panel of Figure 5.5 compares our simplest model ($M_* \propto M_{\rm sat}$, Model 1A) to the observed satellite counts, now including the satellite galaxy selection effects in the model. We randomly sample each of the six Monte Carlo halo simulations five times (choosing 1/5 of the faint satellites but always keeping the full set for $M_V < -11$), compute the mean model prediction as the mean of these 30 samplings, and compute the rms dispersion among these 30 in each absolute magnitude bin. Despite the selection bias against low luminosity satellites, this model fails drastically for any choice of F_*,

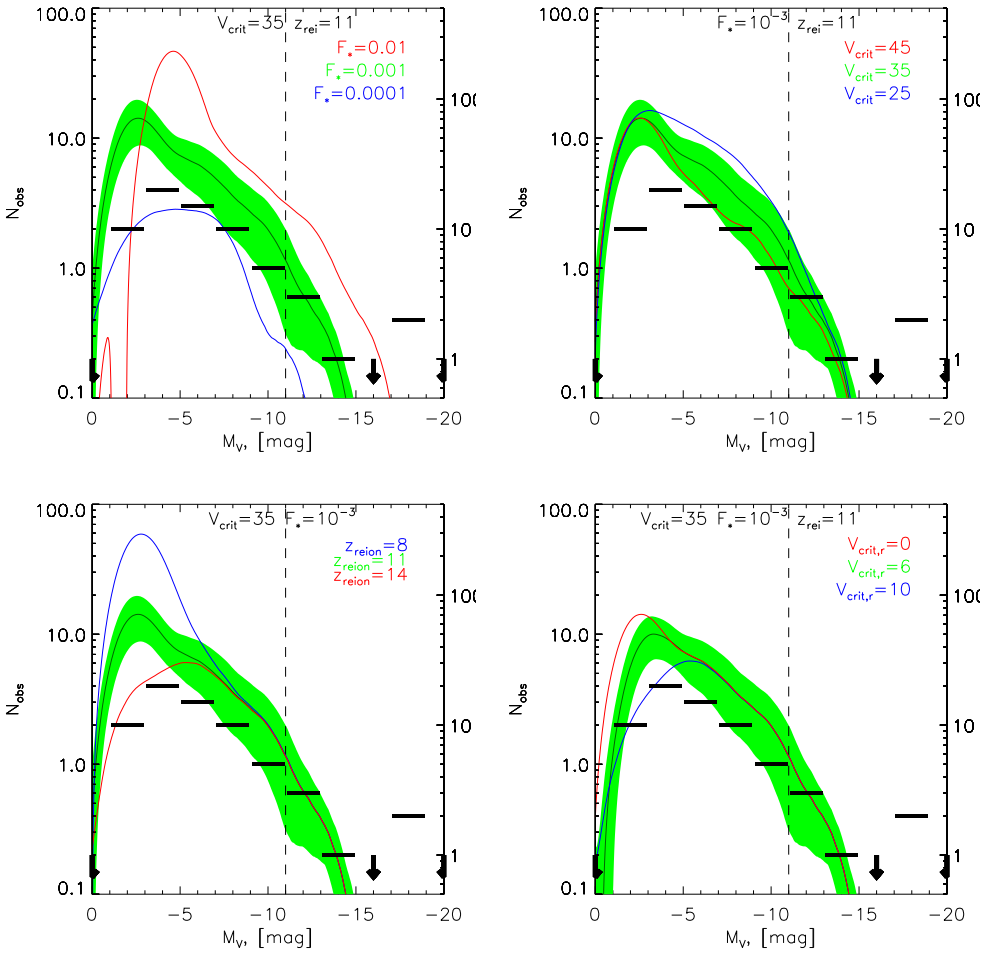

Figure 5.8: Predicted $N_{\rm obs}(M_V)$ for Models 3A and 3B with a variety of parameter choices, in the same format as Figure 5.5. In the first three panels, green bands show Model 3A predictions for a reference parameter set $F_* = 10^{-3}$, $V_{\rm crit} = 35$ km s^{-1}, $z_{\rm rei} = 11$. Red and blue curves show the impact of changing the stellar mass fraction to $F_* = 10^{-2}$ or 10^{-4} (top left), the critical velocity threshold to $V_{\rm crit} = 45$ km s^{-1} or 25 km s^{-1} (top right), or the reionization redshift to $z_{\rm rei} = 8$ or 14 (lower left). The lower right panel compares the prediction of this reference model (now shown by the red curve) to predictions of Model 3B with a pre-reionization critical threshold $V_{\rm crit,r} = 6$ km s^{-1} (green band) or 10 km s^{-1} (blue curve).

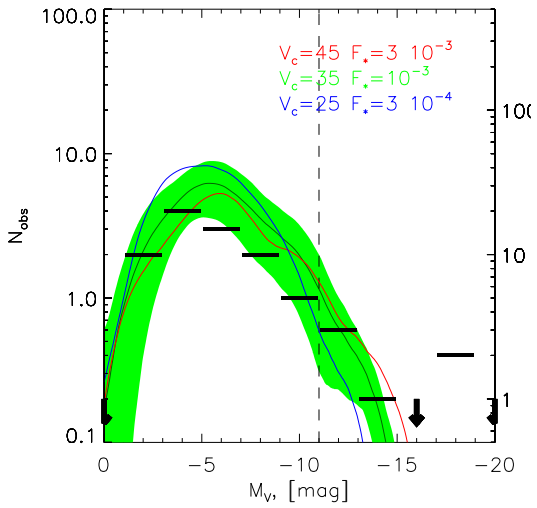

Figure 5.9: Degeneracy between F_* and $V_{\rm crit}$ for Model 3B, in the format of Figure 5.5. Blue, green, and red curves/bands show the parameter combinations $(F_*, V_{\rm crit}) = (3 \times 10^{-4}, 25 \text{ km s}^{-1})$, $(10^{-3}, 35 \text{ km s}^{-1})$, and $(3 \times 10^{-3}, 45 \text{ km s}^{-1})$, which all yield similar levels of agreement with the observations. We adopt $z_{\rm rei} = 11$ and $V_{\rm crit,r} = 10 \text{ km s}^{-1}$ in all cases.

predicting a much steeper luminosity function than observed. For example, the model with $F_* = 10^{-4}$ matches the observed counts near $M_V = -9$ but predicts far too many satellites fainter than $M_V = -6$. Selection effects and newly discovered satellites have not altered this basic discrepancy, first emphasized by Klypin et al. (1999) and Moore et al. (1999). The green band shows the 1σ dispersion in predicted counts, and it is clear that statistical fluctuations will not resolve the discrepancy either.

In the right panel we apply our purely empirical modification, $M_*/M_{\rm sat} \propto M^\alpha$ below a halo mass $M_{\rm sat} = M_0 = 10^{10} M_\odot$ (Model 1B). With $F_* = 10^{-3}$ and $\alpha = 2$, this model achieves reasonable agreement with the the observed $N_{\rm obs}(M_V)$ over the full range $0 \geq M_V \geq -15$. The agreement can be further improved by adjusting F_* and M_0, so it appears that this level of mass-dependent suppression is approximately what is needed to explain the observed shape of $N_{\rm obs}(M_V)$. Linear suppression ($\alpha = 1$, green band) is not sufficient, predicting an excess of faint dwarfs when normalized to the bright dwarfs. All of our models fail to match the brightest bin (comprised of the SMC and LMC); we defer discussion of this discrepancy to the end of this Section.

Figure 5.6 shows the expected $N_{\rm obs}(M_V)$ distributions for Model 2, which has a

sharp $V_{\rm crit}$ threshold for the suppression of SF after reionization in small halos. As in Figure 5.3, the predicted $N_{\rm obs}(M_V)$ is bimodal, with a bright peak corresponding to halos that exceeded $V_{\rm crit}$ before $z_{\rm sat}$ and a faint peak corresponding to stars formed before reionization. Raising the stellar fraction F_* with other parameters fixed (orange vs. blue) shifts both peaks horizontally to higher M_V; the faint peak also increases in height because the brighter (though still faint) satellites can be seen over a larger fraction of the MW virial volume. Lowering $V_{\rm crit}$ with other parameters fixed (red vs. blue) has no impact on the faint peak, but the bright peak extends to fainter magnitudes and grows in height because lower mass halos can now be populated with stars after reionization. Raising $z_{\rm rei}$ (green vs. blue) with other parameters fixed has no impact on the bright peak, but it shifts the faint peak downwards in amplitude and slightly downwards in location because halos have accreted less mass by this higher redshift. While photo-ionization suppression reduces the discrepancy with the number of faint satellites seen in Model 1A, these sharp threshold models predict a gap between the faint and bright satellites that is clearly at odds with the data.

Figure 5.7 compares the Model 2 predictions with those of Model 3A, which uses the Gnedin (2000) formula to incorporate a smoothly increasing suppression of the stellar mass fraction in halos with $V_{\rm circ}(z_{\rm sat}) \lesssim V_{\rm crit}$. In both cases we use parameters $F_* = 10^{-3}$, $V_{\rm crit} = 35$ km s^{-1}, $z_{\rm rei} = 11$. Model 3A is more physically realistic than Model 2, with a mass-dependent suppression that is calibrated on numerical simulations (and is approximately consistent with three independent numerical studies). Galaxies formed in halos with $V_{\rm circ}(z_{\rm sat}) \lesssim V_{\rm crit}$ now fill the gap that was present in Model 2, producing a luminosity distribution that rises continuously from $M_V = -14$ down to $M_V = -2$, before radial selection effects finally cut it off. With these parameter choices, pre-reionization dwarfs dominate the counts (and exceed the observations) for $M_V \leq -4$, but suppressed post-reionization dwarfs dominate the counts at all brighter magnitudes.

Since Model 3 is both more physically realistic and more empirically successful than Models 1 and 2, we focus on it for the remainder of the chapter, including Model 3B in which pre-reionization star formation is suppressed below a circular velocity threshold. Figure 5.8 systematically explores the impact of parameter variations in Models 3A and 3B. In the first three panels, the green band shows the Model 3A predictions for a fiducial set of parameter choices, $F_* = 10^{-3}$, $V_{\rm crit} = 35$ km s^{-1}, and $z_{\rm rei} = 11$.

Changing F_* (top left) shifts the predicted distribution horizontally to higher or lower luminosities, with some change in shape at the faint end because of the luminosity dependence of radial selection effects. Changing $V_{\rm crit}$ alters the predicted counts at intermediate luminosities, $-4 > M_V > -11$, while having little effect at the faint end (where pre-reionization dwarfs dominate) or at the bright end (where most galaxies exceed the highest threshold considered here). Changing $z_{\rm rei}$ alters the height of the pre-reionization peak at faint luminosities but has minimal impact for $M_V < -7$.

With our fiducial parameter choices, Model 3A substantially overpredicts the number of satellites with $M_V \approx -3$. Raising the reionization redshift to $z_{\rm rei} = 14$ erases this discrepancy, but this value of $z_{\rm rei}$ seems implausible given the strong and rapidly evolving opacity of the intergalactic medium at $z \approx 6$ seen in quasar spectra (Fan et al., 2006), and it is only marginally consistent with the WMAP5 results. In the lower right panel, we return to $z_{\rm rei} = 11$ but suppress pre-reionization star formation in halos with $V_{\rm circ}(z_{\rm rei}) < 6$ km s^{-1} (green) or 10 km s^{-1} (blue), motivated by the inefficient gas cooling expected below the threshold for atomic line excitation (Model 3B). The $V_{\rm crit,r} = 10$ km s^{-1} model yields acceptable agreement with the observed number counts over the full range $0 \geq M_V \geq -15$. The $V_{\rm crit,r} = 6$ km s^{-1} model still yields an excess of faint satellites; results for $V_{\rm crit,r} = 8$ km s^{-1} (not shown) are nearly identical to those for 10 km s^{-1}, indicating that an 8 km s^{-1} threshold is already sufficient to essentially eliminate the contribution of pre-reionization dwarfs. This pre-reionization suppression appears to be critical to explaining the number of dwarfs observed by the SDSS.

Within Model 3B, there is strong degeneracy between the values of F_* and $V_{\rm crit}$. Figure 5.9 shows that the parameter combinations $(F_*, V_{\rm crit}) = (3 \times 10^{-3}, 45$ km s$^{-1})$, $(10^{-3}, 35$ km s$^{-1})$, and $(3 \times 10^{-4}, 25$ km s$^{-1})$ all yield similar predictions and acceptable agreement with the observed number counts. The lower values of $V_{\rm crit}$ are favored by the numerical studies of Hoeft et al. (2006) and Okamoto et al. (2008). For the remainder of the chapter we will adopt $(F_*, V_{\rm crit}, z_{\rm rei}, V_{\rm crit,r}) = (10^{-3}, 35$ km s$^{-1}, 11, 10$ km s$^{-1})$ as the fiducial parameter values for Model 3B.

For this fiducial model, Figure 5.10 illustrates in more detail the relative importance of stars formed before and after reionization. For systems with $V_{\rm circ}(z_{\rm rei}) > V_{\rm crit,r}$, filled circles show the fraction of their stars that formed before reionization. For systems with $V_{\rm circ}(z_{\rm rei}) < V_{\rm crit,r}$, open circles show the fraction of stars that *would* have formed

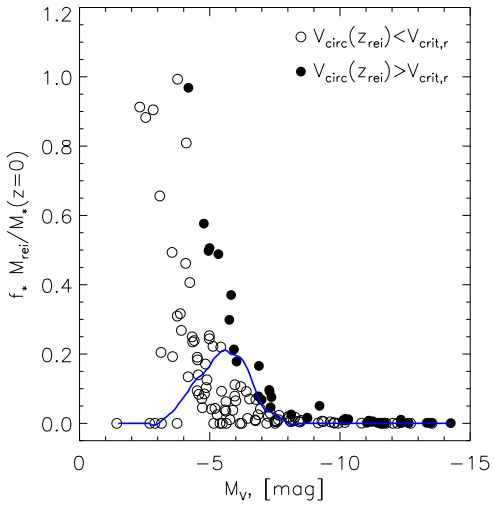

Figure 5.10: Fraction of pre-reionization stars in observable satellites of different luminosities, as predicted by the fiducial Model 3B. Filled circles show $f_* M(z_{\rm rei})/M_*(z = 0)$, the fraction of the stellar mass that formed by $z_{\rm rei}$, for systems that exceeded the pre-reionization threshold, $V_{\rm circ}(z_{\rm rei}) > V_{\rm crit,r} = 10$ km s^{-1}. Open circles show $f_* M(z_{\rm rei})/M_*(z = 0)$ for systems with $V_{\rm circ}(z_{\rm rei}) < V_{\rm crit,r}$, but in the context of Model 3B these systems do not form any stars before reionization. The curve shows the fraction of satellites that formed more than 10% of their stars before the epoch of reionization, in bins of luminosity.

before reionization, but because of the $V_{\rm crit,r}$ threshold these galaxies have no pre-reionization stars in this model. At every satellite luminosity, the average fraction of pre-reionization stars is small, or even zero, but albeit for different reasons at high and low luminosities. The host halos for the brighter, "classical" dwarf satellites were typically massive enough at $z_{\rm rei}$ to exceed $V_{\rm crit}$, but that initial population of stars was subsequently swamped by the much larger post-reionization population. In contrast, the halos that now host the very faintest known satellites ($M_V > -4$) did not exceed $V_{\rm crit,r}$ at $z_{\rm rei}$ and hence — in Model 3B — did not form any stars before $z_{\rm rei}$. A small fraction of the satellites with $M_V \approx -5$ have large populations of pre-reionization stars; these are subhalos that just exceeded $V_{\rm crit,r}$ at $z_{\rm rei}$ but have low enough values of $V_{\rm circ}(z_{\rm sat})$ that their post-reionization star formation was strongly suppressed. If the pre-reionization threshold at $V_{\rm crit,r}$ were smooth rather than sharp, then some additional fainter systems might have significant fractions of pre-reionization stars. However, the general conclusion that pre-reionization star formation should be a small fractional contribution at all satellite luminosities seems fairly robust, provided this star formation is suppressed in halos below the atomic cooling threshold, as seems to be required to match the observed luminosity distribution.

Figure 5.11 shows the complete stellar luminosity function of MW satellites inside 400 kpc, in the absence of any selection effects or incompleteness, again for the fiducial model. (We choose 400 kpc for ease of comparison to Tollerud et al. 2008.) In contrast to other figures, it shows the luminosity function for the whole sky (4π sr) and in terms of dN/dM_V (i.e., in bins of 1 magnitude). Absent selection effects, the luminosity function continues to rise toward faint magnitudes (as noted by Koposov et al., 2008a), contrary to the almost flat luminosity distribution of observed dwarfs. The total number of satellites within 400 kpc brighter than $M_V = 0$ expected for the fiducial Model 3B is 230 ± 35. This value is somewhat lower than the 400 derived by Tollerud et al. (2008), but since both estimates extrapolate the number of known dwarfs by a factor of ~ 10, we do not place much weight on this difference.

None of the models shown in Figures 5.5–5.9 reproduce the brightest observed bin — i.e., they all fail to produce satellites as bright as the SMC and the LMC. Our successful models have low stellar mass fractions, $F_* \sim 10^{-3}$, even well above the photo-ionization threshold $V_{\rm crit}$. The most massive subhalos in our Monte Carlo realizations have typical mass $M_{\rm sat} \sim 10^{11} M_\odot$ (ranging from $10^{10.5} M_\odot$ to $10^{11.4} M_\odot$),

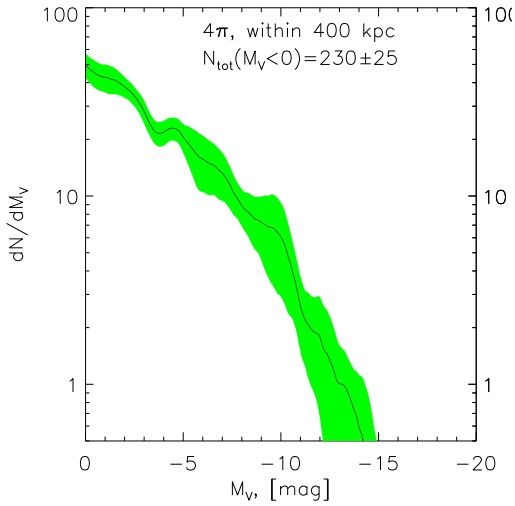

Figure 5.11: The predicted number of MW satellites per unit magnitude within 400 kpc across the whole sky averaged from 6 MC realizations, using the fiducial model parameters (Model 3B with $F_* = 10^{-3}$, $V_{\rm crit} = 35$ km s^{-1}, $V_{\rm crit,r} = 10$ km s^{-1}, and $z_{\rm rei} = 11$) and assuming no observational incompleteness. The total number of satellites with stellar luminosities brighter than $M_V = 0$ is 230 ± 25. Note that this Figure gives counts in 1-magnitude bins rather than the 2-magnitude bins used in earlier Figures.

with second-ranked halos that are $0.2-0.4$ dex less massive. Reproducing the $\sim 10^9 M_\odot$ stellar masses of the Magellanic Clouds then requires much higher stellar mass fractions $F_* \sim 0.05$. To reproduce the full satellite population, the efficiency of gas accretion and star formation must continue to rise with halo mass above $V_{\rm crit}$, or at least it must be higher for the SMC and LMC hosts. Since the number of bright SMC and LMC-like objects in our model are determined mainly by one parameter F_*(because these objects are not suppressed by the photo-ionization), that rise of star formation efficiency can not be accommodated with our simple model without introducing additional parameters.

5.4.3 Velocity dispersions, central masses, and radial distributions

As discussed in §5.3.2, predicting stellar velocity dispersions requires assumptions beyond those needed to compute $N_{\rm obs}(M_V)$. In particular, we assume that the satellites' host subhalos have NFW profiles with concentration given by the theoretically expected mean $c(M)$ relation at $z_{\rm sat}$, and that subsequent dynamical evolution (e.g., tidal stripping) does not alter the mass distribution of the inner parts of the subhalo probed by the stars. We also take the observed stellar radii ($20-150\,$pc, see § 5.3.2 for details) as input rather than predicting them from a physical model. With these assumptions, the right panel of Figure 5.12 shows the predicted distribution of stellar velocity dispersions for Model 3B with our fiducial parameter choices. The characteristic value and narrow spread of velocity dispersions for the newly discovered SDSS dwarfs arises quite naturally from these models, despite the large range of stellar luminosities and host subhalo masses. The predicted distribution is more sharply peaked than the observed one, probably because we did not include scatter in the halo concentration-mass relation and did not include observational uncertainties in the dispersion measurements. The mean value of σ_* differs by $< 20\%$ between data and model, but we consider this small discrepancy is not worrisome, given the simplicity of our dynamical modeling.

The total masses of dwarf satellites are difficult to determine observationally because of the small extent of the stellar distributions relative to the expected extent of the dark matter subhalo. However, Strigari et al. (2008) show that the total mass (principally dark matter) within a radius of $300\,$pc, M_{300}, can be inferred robustly from observations for nearly all of the known satellites. The top panel of Figure 5.13 compares the fiducial model predictions of M_{300} to the Strigari et al. (2008) measurements. The model (red diamonds) naturally reproduces the key result of Strigari et al. (2008): over

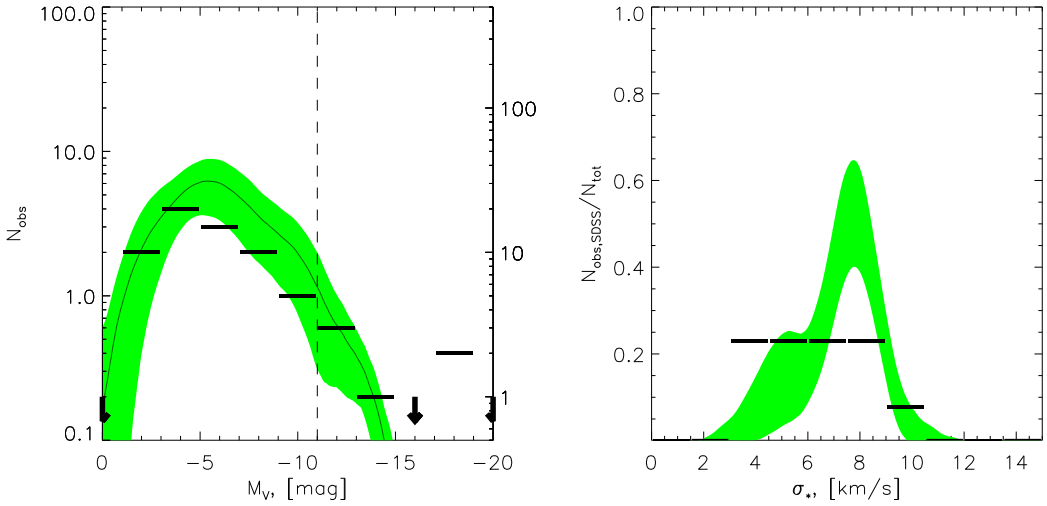

Figure 5.12: Predictions of Model 3B with the fiducial parameters $(F_*, V_{\rm crit}, z_{\rm rei}, V_{\rm crit,r}) = (10^{-3}, 35 \text{ km s}^{-1}, 11, 10 \text{ km s}^{-1})$ compared to the observed distributions of absolute magnitude (left) and stellar velocity dispersions (right). The format of the left panel is the same as Figure 5.5. The right panel shows predicted and observed velocity dispersions only for the SDSS dwarfs — i.e., those with $M_V > -11$ — with data taken from Simon and Geha (2007).

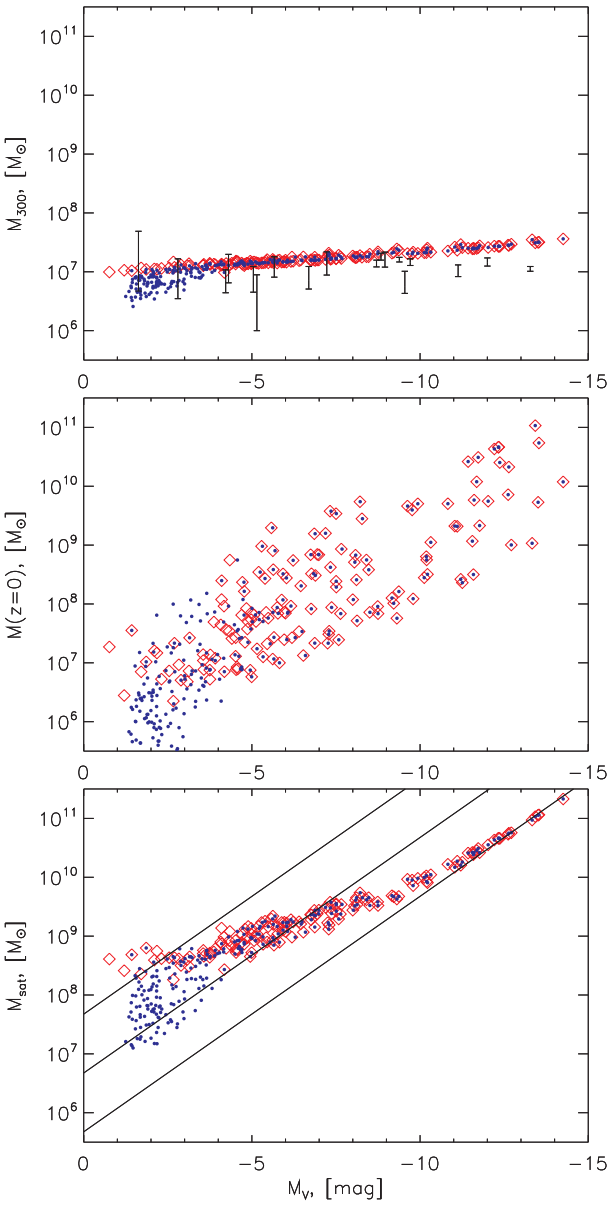

Figure 5.13: Masses of the DM subhalos within the central 300 pc (top), their total present-day masses (middle) and their masses at the time of accretion into larger halos (bottom). We only show halos hosting observable satellites within the MW virial radius, as a function of satellite luminosity. Red diamonds show all the observable galaxies from six realizations of the fiducial Model 3B with $(F_*, V_{\rm crit}, z_{\rm rei}, V_{\rm crit,r}) = (10^{-3}, 35 \text{ km s}^{-1}, 11, 10 \text{ km s}^{-1})$. Blue filled circles show the predictions of Model 3A, which includes pre-reionization dwarfs (or, equivalently, has $V_{\rm crit,r} = 0$). Error bars show the estimates of M_{300} for observed MW satellites from (Strigari et al., 2008). Solid lines in the bottom panel show, from top to bottom, $M_*/M_{\rm sat} = 10^{-5}$, 10^{-4}, and 10^{-3}. Our models do not incorporate scatter in the concentration-mass relation; adding the theoretically expected scatter would add roughly 0.15 dex of rms scatter to the M_{300} predictions.

an enormous range of luminosities, the satellites have a narrow range of M_{300}, tightly concentrated around $10^7 M_\odot$. The theoretical prediction is artificially tight because we have not included scatter in halo concentrations, which would produce roughly 0.15 dex (rms) of scatter in M_{300} (see Macciò et al. 2009, figure 1). The model predicts a weak trend of M_{300} with luminosity, which is not evident in the data (but is similar to that predicted by Macciò et al. 2009).

While the M_{300} range of the satellites is low, the range of *total* subhalo masses (at $z = 0$) is more than three orders of magnitude, as shown in the middle panel of Figure 5.13. The trend of total mass with luminosity is much stronger than the trend for M_{300}, though there is a large scatter in mass at fixed luminosity because of tidal stripping. The near constancy of M_{300} is a consequence of the density profiles of CDM halos: NFW halos with the theoretically predicted $c(M)$ relation have only a weak dependence of M_{300} on total mass over the range $\sim 10^7 - 10^{10} M_\odot$ that hosts observed Milky Way satellites (see Macciò et al. 2009 for further discussion). Thus our models and the models of Macciò et al. (2009) are able to reproduce the narrow observed range of M_{300} without much difficulty (see also Li et al. 2008, who examine M_{600} rather than M_{300}). We note, however, that if we also allow satellites to form stars with efficiency $F_* = 10^{-3}$ before reionization (Model 3A), then the M_{300} range for the lowest luminosity dwarfs, with $M_V > -3$, extends downwards to $M_{300} \sim 10^{6.5} M_\odot$ (blue circles in Figure 5.13). Thus, careful dynamical measurements for the faintest dwarfs could in principle distinguish whether they arise mainly from pre-reionization star formation or from highly suppressed post-reionization star formation in more massive halos. It is noticeable that our model as well as the models of Macciò et al. (2009) and Li et al. (2008) predicts that M_{300} or M_{600} should slightly increase with galaxy luminosity contradicting the observations, where there is no correlation at all of M_{300} versus luminosity (Strigari et al., 2008). The reason of this disagreement is yet to be understood. It either can be caused by some problems with the data (selection effects or systematics in M_{300} measurements) or by some astrophysical effects. For example Macciò et al. (2009) eliminates the correlation of M_{300} versus luminosity by assuming that the inner profile of the halos with low concentration (i.e. massive halos) is modified during the process of tidal stripping (Kazantzidis et al., 2004).

Comparing the middle and upper panels shows that a small number of objects have $M(z = 0)$ lower than M_{300}, which is possible because we calculate M_{300} based

on the subhalo profile at accretion. The tidal radii of these systems are $< 300\,\mathrm{pc}$, but they are all faint satellites for which the stellar Plummer radii are small. While their true M_{300} values should be $M(z = 0)$, the values calculated in the upper panel are probably more directly comparable to the quantities estimated by Strigari et al. (2008), who extrapolate to 300 pc for the faintest systems assuming that they are not tidally truncated within this radius. To minimize the tidal effects one may also compute the masses within 100 pc instead of 300 pc. For our simulated galaxies we also derive M_{100}, which are in the range $1 \times 10^6 - 4 \times 10^6\,M_\odot$ and are also consistent with the $M_{100} \approx 1 \times 10^6 - 3 \times 10^6\,M_\odot$ measurements from Strigari et al. (2008)(supplementary information).

The bottom panel of Fig. 5.13 shows the value of $M_{\rm sat}$ as a function of luminosity. The relation obviously reflects the underlying formula used to assign stellar masses to the DM halos (eqn. 5.5), and the scatter caused by the range of accretion redshifts (which affects the $M_{\rm sat} - V_{\rm circ}$ mapping) is small. Even the faintest observable dwarfs have $M_{\rm sat} \sim 10^{8.5} M_\odot$, but they have star formation efficiencies of only $\sim 10^{-5}$. The difference between the middle and bottom panels illustrates the effect of tidal stripping. Nearly all the spread of $M(z = 0)$ at fixed M_V comes from different degree of tidal stripping.

Figure 5.14 compares the distribution of heliocentric distances of the MW satellites found in the SDSS to the predicted distribution for $M_V > -11$ satellites from our fiducial model. We show one distribution for each of the six Monte Carlo halo realizations. There are significant halo-to-halo variations in the predicted distributions, and the observed distribution follows the lower envelope of the predictions. The distance distribution is strongly influenced by the radial selection effects (the model predictions would be very different if we did not include them), but it also depends on the radial profile of subhalos and the dependence of this profile on $M_{\rm sat}$ and $z_{\rm sat}$, so matching the observed distribution is a significant additional success of the model.

5.5 Conclusions

The satellite discoveries in the SDSS (Belokurov et al., 2006b, 2007c; Irwin et al., 2007; Koposov et al., 2007b; Walsh et al., 2007; Willman et al., 2005b; Zucker et al., 2006b) have transformed our understanding of the MW's dwarf satellite population, extending

Galaxy	$\mathbf{M}_V$	σ_*	$\mathbf{D}_\odot$
Name	mag	km/s	kpc
Bootes	−6.3	6.6	60
Canes Venatici II	−4.9	4.6	150
Carina	−9.4	6.8	100
Coma	−4.1	4.6	45
Canes Venatici I	−8.6	7.6	220
Draco	−8.75	10.0	80
Fornax	−13.2	10.5	138
Hercules	−6.6	5.1	130
Leo I	−11.5	8.8	250
Leo II	−9.6	6.7	205
Leo IV	−5.0	3.3	160
LMC	−18.6	-	49
Sagittarius	−12.1	11.4	24
Sculptor	−11.1	6.6	80
Sextans	−9.5	6.6	86
Segue 1	−1.5	4.3	23
SMC	−17.2	-	58
Ursa Minor	−9.0	9.3	66
Ursa Major I	−5.5	7.6	100
Ursa Major II	−4.2	6.7	30
Willman I	−2.7	4.3	40

Table 5.2: Satellites used for the analysis and parameters adopted

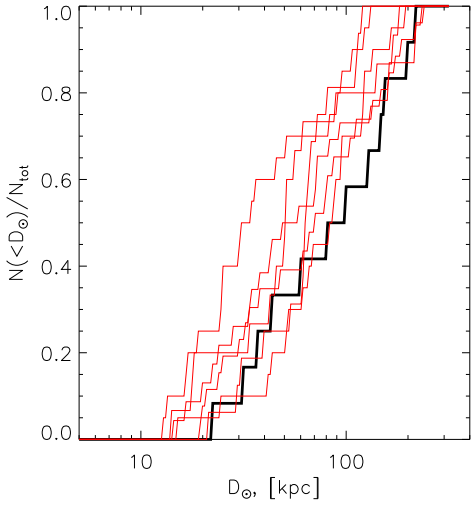

Figure 5.14: Comparison of the model predictions for the cumulative distance distribution of the satellite galaxies with those observed in the SDSS (black line). The predictions of the Model 3B with $(F_*, V_{\rm crit}, z_{\rm rei}, V_{\rm crit,r}) = (10^{-3}, 35 \text{ km s}^{-1}, 11, 10 \text{ km s}^{-1})$ are shown as red lines.

the luminosity range by two orders of magnitude and the implied number of systems by a factor of 20. Careful quantification of the SDSS satellite detection efficiency (Koposov et al., 2008a; Walsh et al., 2009) allows models that specify the relation between dark matter subhalos and their stellar content to be tested quantitatively against the observations. We have shown that CDM-based models incorporating previously advocated, physically plausible mechanisms for suppressing the stellar content of low mass halos can reproduce the observed properties of the known satellite population, including their numbers, luminosity distribution, stellar velocity dispersions, central masses, and heliocentric radius distribution. However, parameters of these models are tightly constrained, and alternative assumptions lead to conflict with the data. In summarizing our results, it is useful to review both what works and what doesn't.

What works is a model in which the photo-ionizing background suppresses gas accretion onto halos with $V_{\rm circ}(z_{\rm sat}) < V_{\rm crit} \approx 35$ km s^{-1} (Bullock et al., 2000; Quinn et al., 1996; Thoul and Weinberg, 1996), with the smooth mass-dependent suppression suggested by numerical simulations (eqn. 5.5; Gnedin 2000; Hoeft et al. 2006; Okamoto et al. 2008), and inefficient molecular cooling (and/or stellar feedback) drastically reduces the efficiency of star formation in pre-reionization halos below the hydrogen

atomic line cooling threshold $V_{\rm crit,r} \approx 10$ km s^{-1} (Barkana and Loeb, 1999; Bovill and Ricotti, 2009; Haiman et al., 1997; Machacek et al., 2001; O'Shea and Norman, 2008; Wise and Abel, 2007). There is some degeneracy between this model's two main parameters, $V_{\rm crit}$ and F_*, as shown in Figure 5.9, but with either parameter fixed the other is fairly well constrained (Figure 5.8). The other two parameters, $z_{\rm rei}$ and $V_{\rm crit,r}$, just need to be in a range that keeps pre-reionization star formation too low to affect the observable luminosity function. For the values $V_{\rm crit} = 25 - 35$ km s^{-1} favored by numerical simulations, F_* must be $\lesssim 10^{-3}$, so even subhalos above the $V_{\rm crit}$ threshold have star formation efficiency far lower than the values $F_* \approx 0.1 - 0.4$ found for bright galaxies (e.g., Dutton et al. 2007; Gnedin et al. 2007; Mandelbaum et al. 2006; Pizagno et al. 2005; Xue et al. 2008).

If we assign stellar extents based on observations, and make the reasonable dynamical assumptions discussed in §5.3.2, then our fiducial model naturally explains the characteristic value and narrow spread of stellar velocity dispersions found for SDSS dwarfs by Simon and Geha (2007). It also explains the characteristic value and narrow range of M_{300} values found by Strigari et al. (2008). The M_{300} values do not depend on the assumed stellar extent, and their narrow range arises from the theoretically predicted structure of CDM halos, which have a weak dependence of M_{300} on total halo mass over the range $M_{\rm halo} \sim 10^8 - 10^{11} M_\odot$. Thus any CDM-based model that prevents formation of observable dwarfs in halos below $\sim 10^7 M_\odot$ should qualitatively reproduce the Strigari et al. (2007, 2008) results (e.g., Li et al. 2008; Macciò et al. 2009). Tempering this success, however, is the fact that the total $z = 0$ subhalo masses in our model span three orders of magnitude; some of this range is a consequence of tidal stripping, but the span of $M_{\rm sat}$ values is only slightly narrower. The model, in combination with the radial selection biases found by Koposov et al. (2008a), also explains the observed heliocentric radius distribution of the SDSS dwarfs, which tests the predicted Galactocentric radius distribution of subhalos and its dependence on mass and accretion redshift.

Many alternative models fail badly in reproducing the observed luminosity distribution. Models with constant $M_*/M_{\rm sat}$ predict far too many faint satellites relative to bright satellites. The SDSS discoveries and luminosity-dependent selection biases do not in themselves resolve the "missing satellite" discrepancy highlighted by Klypin

et al. (1999) and Moore et al. (1999); strong mass-dependent suppression of star formation efficiency is still required to reconcile CDM predictions with observations. A simple model in which $M_*/M_{\rm sat} = 10^{-3}(\Omega_b/\Omega_m)(M_{\rm sat}/10^{10}M_\odot)^2$ for $M_{\rm sat} < 10^{10}M_\odot$ is reasonably successful at matching the observations. This successful "empirical" model has a mass dependence of star formation efficiency roughly like that of the successful, physically motivated photo-ionization model (eqn. 5.5; note that $M_{\rm sat} \propto V_{\rm circ}^3$ at fixed $z_{\rm sat}$).

Models with *sharp* suppression of star formation below the photo-ionization threshold $V_{\rm crit}$ fail at intermediate luminosities, $M_V \sim -8$. Pre-reionization star formation can provide the population of faint dwarfs in such a model, but there is an unacceptable gap between the faint and bright populations (or, for parameter choices that fill the gap, there is an excess of dwarfs at other luminosities). It is striking, therefore, that the *form* of the mass-dependent photo-ionization suppression found in numerical simulations is just that required to match the shape of the observed luminosity distribution. However, the conversion of accreted baryons to stars must be very inefficient for our fiducial model to work, and it is not obvious why this conversion efficiency should be mass independent.

The most interesting of our "negative" conclusions is that star formation in halos before reionization must be extremely inefficient to avoid producing too many satellites in the range $0 \gtrsim M_V \gtrsim -6$. Examination of Figure 5.8 suggests that the upper limit on the fraction of halo baryons converted to stars is a few $\times 10^{-4}$ for $z_{\rm rei} = 11$, or 10^{-3} if reionization is pushed back to $z_{\rm rei} = 14$. Madau et al. (2008) have reached exactly the same conclusion, with a similar numerical value for the efficiency limit, using the *Via Lactea II* simulation instead of a semi-analytic method to predict the model subhalo population. Suppression of star formation in halos below the hydrogen atomic line cooling threshold is physically plausible, as the metallicity is low and molecular cooling should be inefficient. For agreement with $N_{\rm obs}(M_V)$, we require pre-reionization suppression in halos with $V_{\rm circ}(z_{\rm rei}) < V_{\rm crit,r} \approx 10$ km s^{-1}.

There are several caveats to these conclusions. First, as discussed in §5.4.2, reproducing the Magellanic Clouds requires that the most massive subhalos have $M_*/M_{\rm sat} \sim 0.05 - 0.1$, well above the $F_* \sim 10^{-3}$ of our fiducial model. Thus, the photo-ionization suppression described by equation (5.5) must join onto a continuing increase of star formation efficiency with subhalo mass above $V_{\rm crit}$, an increase that is presumably driven

by other physical mechanisms. Indeed, there is nothing about our results that necessarily picks out photo-ionization as the suppression mechanism in low mass subhalos, but it is a mechanism that comes in naturally (one might argue inevitably) at the desired scale (Bullock et al., 2000), and the numerically calibrated form yields a good match to the observed luminosity distribution.

In our fiducial model, even the faintest SDSS dwarfs form most of their stars after reionization, but they have $V_{\rm circ}(z_{\rm sat})$ far enough below $V_{\rm crit}$ that their star formation is highly suppressed according to equation (5.5). The SDSS dwarfs are physically a continuum with the classical dwarfs, and their much lower luminosities are a consequence of the highly non-linear relation between star formation efficiency and halo mass below $V_{\rm crit}$. Halos with $V_{\rm circ}(z_{\rm rei}) > V_{\rm crit,r}$ form pre-reionization stars, but in nearly all cases they grow large enough by $z_{\rm sat}$ that the post-reionization population dominates by a large factor. A small number of systems with $M_V \approx -5$ could have large fractions of pre-reionization stars, but at any luminosity such systems are rare. These conclusions are robust within our framework, but if we allowed for departures from our adopted prescriptions — in particular if photo-ionization suppression for $V_{\rm circ} \ll V_{\rm crit}$ were more aggressive than equation (5.5) implies and pre-reionization suppression weaker than we have assumed — then it might be possible to construct models in which many dwarfs with $M_V \gtrsim -6$ are pre-reionization "fossils." The efficiency of converting halo baryons to stars in these systems must still be $\sim 10^{-4}$ or less to avoid producing too many faint satellites. Bovill and Ricotti (2009) and Salvadori and Ferrara (2009) have argued that halos cooling by H_2 before reionization naturally give rise to the physical and chemical properties of the SDSS dwarfs. However, even the low star formation efficiencies $\sim 0.5\% - 2\%$ found by Salvadori and Ferrara (2009) appear far too high to be consistent with the observed number counts. On the other hand, Busha et al. (2009) propose a model in which post-reionization suppression of star formation is highly efficient (a sharp threshold) but the star formation efficiency in pre-reionization halos is strongly mass dependent, effectively spreading the low luminosity peak evident in our Figure 6 up towards higher luminosities so that it fills out the entire faint end of the luminosity function.

A third caveat is that we do not explain the origin of the observed stellar extents; we just show that once the observed extents are adopted as inputs, then the observed stellar velocity dispersions emerge naturally. One possible explanation is that the baryons in

low mass halos condense *until* they reach a scale at which the velocity dispersion is a few km s^{-1}, and that this minimum dispersion provides the conditions necessary for star formation. We also have not attempted to explain the chemical abundance distributions or star formation histories of the satellites (see, e.g., Orban et al. 2008; Salvadori and Ferrara 2009; Salvadori et al. 2008).

A final caveat is that we have assumed that all dwarfs luminous enough to be found in the SDSS also lie above the surface brightness threshold for detection, which is about 30 mag $arcsec^{-2}$ (Koposov et al., 2008a). Since some of the known satellites approach this threshold, it is possible that others fall below it. A large population of lower surface brightness dwarfs would change the number counts that our model reproduces. Note also that a large population of pre-reionization dwarfs would be observationally allowed if they lie below the surface brightness threshold; however, even in this scenario the pre-reionization dwarfs do not account for the presently known satellites. Deeper large area imaging surveys, such as Pan-STARRS, the Dark Energy Survey, and LSST, will show whether the MW satellite population includes a significant number of lower surface brightness systems.

Our model makes several predictions that can be tested by these upcoming surveys or by further follow-up studies of known dwarfs. Deeper surveys should reveal many more satellites, more than 200 with $M_V < 0$ and $D_\odot < 400$ kpc over the full sky, with the luminosity function shown in Figure 5.11. Deep imaging of Andromeda and other nearby galaxies can show whether they have similar satellite systems, though these searches will not reach the extremely low luminosities that can be probed in the MW. Most satellites in our model have stellar extents that are substantially smaller than the present-day tidal radius of their host halo. Tidal tails and tidal disruption should be rare, an implication that may be challenged by photometric evidence on the profiles and shapes of the ultra-faint galaxies, which have been interpreted as signs of tidal distortion or disruption (e.g. Martin et al. 2008). Measurements of the total subhalo masses of known dwarfs would provide a powerful test of the model predictions in Figure 5.13, but the small stellar extents may make such measurements impossible. Our models predict that satellites continue to form stars down to $z_{\rm sat}$ or below, and many observable systems should have $z_{\rm sat} = 1 - 2$ (see Figure 5.2). These predictions may be testable with detailed stellar population modeling.

Our results greatly strengthen the argument (Benson et al., 2002; Bullock et al., 2000; Kravtsov et al., 2004; Somerville, 2002) that photo-ionization naturally reconciles the CDM-predicted subhalo population with the observed dwarf spheroidal population, thus solving the "missing satellite problem" highlighted by Klypin et al. (1999) and Moore et al. (1999). The fiducial model presented here offers a detailed, quantitative resolution of this problem in light of new, greatly improved observational constraints, while relying on previously postulated and physically reasonable mechanisms to suppress star formation in low mass halos. The MW satellites provide a fabulous laboratory for studying galaxy formation at the lowest mass scales, and much remains to be understood about gas cooling, star formation, feedback, and chemical enrichment in these systems. These issues provide challenging targets for numerical simulations and semi-analytic models, whose predictions can be tested against detailed studies of the dynamics and stellar populations of the known dwarf satellites and of the many new satellites that will be revealed by the next generation of sky surveys.

5. A QUANTITATIVE EXPLANATION OF THE OBSERVED POPULATION OF MILKY WAY SATELLITE GALAXIES.

6

Conclusions and future prospects

6.1 Conclusions

The Milky Way is the galaxy which we can study in the most detail. Such studies have demonstrated that the MW is a unique laboratory to learn about galaxy formation. One of the most promising ways to study our Galaxy is through large surveys such as the Sloan Digital Sky Survey. This survey has proven itself to be a treasure trove for studies of the Milky Way and the understanding galaxy formation. In this thesis I have demonstrated how we can learn more about the MW, especially its stellar substructure, through data mining and discoveries in the SDSS dataset and how to use these observational discoveries to better understand the process of galaxy formation.

The main results obtained in this thesis are that:

- I have developed a new algorithmic technique to search for localized stellar overdensities in the Milky Way halo. The application of this technique to the SDSS dataset allowed me to find two previously undiscovered globular clusters with unusual properties. These clusters are two of the faintest observed in the halo and are probably in the final stages of "self-evaporation". Based on the expected short life-times of these objects I suggested that the halo may be filled with such tiny globular clusters, some of which must be in late stages of self-evaporation. Since one of the globular clusters lies close to the Sagittarius tidal stream I also suggested that it may have been torn from the Sgr dwarf galaxy.

- I have developed a novel set of techniques allowing the analysis of stellar streams in the Galactic halo. I have used these techniques to study one particular long

stellar stream named GD-1. This stream is extremely faint and contains only around 2000 stars scattered along a 60-degree arc on the sky. After applying advanced filtering and modeling techniques to the SDSS dataset, I have for the first time determined the statistical proper motion of the stream stars, and their 3-dimensional positions. I have performed spectroscopic observations of a sample of stars spread along the stream in order to determine the radial velocities along the stream. Altogether, these data has allowed me to construct, for the first time, a 6-D map of the stream along more than 60° on the sky. Under the assumption that the GD-1 stellar stream traces one orbit in the Galactic potential, I have constrained several parameters of the Galactic potential. Using the model of a spheroidal logarithmic potential, I have derived its flattening $q_\phi = 0.88^{+0.09}_{-0.06}$ (which is the only measurement of the shape of the potential at ∼15 kpc distance from the Galactic center) and circular velocity at the Sun's radius $V_c = 224 \pm 13$ km/s (which is one of the most precise measurements to date). I have also tried to constrain the flattening of the dark matter halo by using a 3-component Galaxy model consisting of a disk, a bulge and a halo, but the existing data only allowed me to determine the lower limit on the flattening of the dark matter halo: $q_\phi > 0.9$ with 90% confidence.

- Using the technique I developed to find overdensities in stellar catalogues, I have undertaken a systematic, automatic search for overdensities in the SDSS DR5 data. In order to understand its completeness limits, I have applied the same techniques to an extensive mock dataset, which consisted of a large sample of artificial galaxies and clusters with different sizes and luminosities, added to the real SDSS DR5 data. This allowed me to determine the detection efficiency of my algorithm for objects with different sizes, luminosities and located at different distances. I have found that there is an almost distance-independent surface brightness limit of ∼30 mag/sq.arcsec which does not allow fainter objects to be discovered, and a distance-dependant luminosity limit. Using these results I have derived the incompleteness-corrected luminosity function of MW satellites which can be directly compared to the luminosity functions predicted by different galaxy formation models.

- Understanding the SDSS incompleteness of the searches for dwarf galaxies in the MW halo allowed me, for the first time, to make an accurate comparison of the predictions of galaxy formation models for Milky Way satellites with observations and constrain the models. I used a semi-analytical DM simulation and a set of analytical recipes in order to assign stellar masses to individual DM halos and thus predict what the population of dwarf galaxies in the MW halo should look like. After taking into account the radial incompleteness of searches for dwarf galaxies and tidal disruption, I could compare the distribution of different properties of potentially observable galaxies in the simulations with the properties of observed galaxies. Despite the recently increased sample of dwarf galaxies and despite a thorough understanding of dramatic radial incompleteness of SDSS, a large difference remains between the number of DM halos and the number of observed galaxies, if all halos host galaxies. Additional ingredients in the galaxy formation models, which suppress the formation of galaxies in small DM halos, are required in order to solve the discrepancy. I have shown that if the photo-evaporation of cold gas in low-mass DM halos after the epoch of reionization and the suppression of H_2 cooling before the epoch of reionization are included in the models, then they can perfectly match the observations. Apart from reproducing the observed luminosity function well these models also reproduce the radial distribution and stellar velocity dispersion distributions of MW satellites. The model also correctly predicts that the total mass within 300 pc from the center of satellites, M_{300}, is $\sim 10^7\,M_\odot$, which is consistent with recent measurements. On that basis I could conclude that my model gives a physically motivated solution of the "missing satellite" problem.

Overall the study of the MW using the data from the Sloan Digital Sky Survey constitutes a considerable progress in understanding the Milky Way and its outskirts. It also presents a range of data mining techniques that can be used when the data from new surveys will come.

6.2 Future prospects

"Near-field cosmology" is a rapidly developing field and, with the advent of current and future large surveys such as Pan-STARRS (Kaiser et al., 2002), GAIA (Perryman

et al., 2001), LSST (Tyson, 2002), the work presented in this thesis can be continued and expanded. In this section I present some future projects, which extend the ideas presented in this thesis.

6.2.1 MW halo structure

Recently it has been demonstrated that the MW stellar halo has a great deal of substructure. Numerous stellar streams and dwarf satellites were found in it. The luminosity of some of these satellites are extremely low (e.g. clusters from Chapter 2) and close to the edge of the current detectability (see Chapter 4). Some of these low luminosity objects may be undergoing tidal stripping or disruption. It seems that now our searches are able to detect structures, of which is unclear, whether they are *bona fide* dwarfs or just small, gravitationally unbound clumps of halo stars. Thus, the distribution of stars in the halo on these small scales is not yet understood. To what extent is the MW halo filled with gravitationally unbound small stellar clumps remnants of severely disrupted satellites? Or is it relatively smooth on small scales? I think that a possible way to tackle this problem is to use proper color-magnitude selection/filters, that will allow the quantification of stellar population densities at certain distances. The statistical properties of the stellar distribution can then be calculated properly and compared to Poisson statistics. Another way of looking at this problem would be the measurement of the correlation function of the halo stars. I think that a better understanding of small scale structure in the MW halo is necessary to constrain the number of accretion events in the MW halo and to understand the efficiency of tidal disruption and phase mixing in the halo.

6.2.2 Searches for stellar streams

In the last few years several new stellar streams have been found, many by relatively simplistic methods, or even by eye. Since our expectations from the models indicate that the number of streams is potentially much larger than we seem to see now, we need more advanced methods to search for streams, similar to the method presented in Chapter 2 and used to find stellar clusters in the data. For example the Hough transform or the generalized Hough transform (Duda and Hart, 1972; Koposov, 2008) seem to be good candidates for finding streams. An experiments with these methods (Koposov, 2008) has shown that these methods are able to find known streams, and the detection

of these streams may be done automatically. Thus, the idea of the future research in that field is to use the Hough transform together with the proper color-magnitude filter to detect stellar streams in SDSS and other surveys. In principal, if the final stream searching method is fully automated, then its completeness properties can be determined, enabling a direct comparison between the simulations and the number of observed streams (as in Chapters 4 and 5).

6.2.3 Statistical proper motions

Our analysis of the GD-1 stream presented in Chapter 3 demonstrated for the first time that proper motions can be effective "filters" to significantly enhance the contrast of the structures in the MW halo. Although the proper motions in SDSS are only measured for stars brighter than $r = 20$ and the precision of the individual proper motion measurements is only ~ 3 mas/yr, they allow us to study the MW halo within 10 kpc around the Sun. I believe that the search for substructure combining 5 band photometry and proper motions has yet to reveal many interesting features in the halo.

6.2.4 Stream DM sub-halos interaction and the MW potential

Currently, we know several cold stellar streams in the MW halo, e.g the stream of Pal 5 and the GD-1 stream. The GD-1 stream is especially interesting since it spans $\sim$ 60 degrees on the sky. As I showed in Chapter 5 MW halo is presumably filled with many DM sub-halos without detectable stellar content. While orbiting the MW, all the cold streams should become perturbed by these dark matter halos, become hotter, more dispersed, tilted or getting strange density gradients along the streams. I am interested in tackling the question of what observational signatures one could find of interaction of a DM halo with the detailed structure of a cold stream (such as Pal 5 or GD-1). I envisage to study whether the streams' orbits, velocity dispersions and other properties require the presence of a disturbance from a simple orbit around the MW. Evidence for the stream-DM halo interaction, if observed, would be an extremely important confirmation of the success of the CDM paradigm.

It is clear that Milky Way (sub-)structure will remain an exciting, rapidly developing field for the next decade, or even longer.

Appendix A

The Calculation of the Correction to the Luminosity Function

To calculate the luminosity function of Milky Way satellites within $r_{\rm LF} = 280\,{\rm kpc}$, we select all the satellites within DR5 which are interior to $r_{\rm LF}$, and construct the histogram of M_V of these objects. From the simulations, we know that not all objects are detected with 100% efficiency and the histogram $h(M_V)$ is weighted with the object detection efficiencies.

$$h(M_V) = \sum_i \frac{1}{\epsilon_i} \delta(M_V, M_{V,i})$$

where ϵ_i is the detection efficiency of i-th object, $M_{V,i}$ its luminosity, and $\delta(M_V, M_{V,i}) = 1$, if M_V and $M_{V,i}$ are within one bin of the histogram, and 0 otherwise.

Figure 4.12, shows how the maximal accessible distance depends on the galaxy luminosity (the $r_{\rm max}(M_V)$ function). From this function, we can construct the maximal accessible volume within the DR5 footprint (which covers 1/5 of the sky) as a function of galaxy luminosity, namely $V_{\rm max}(M_V) = 4\pi/3\, f_{DR5}\, r^3_{\rm max}(M_V)$(see Figure 4.13), where f_{DR5} is the fraction of the sky covered by DR5 . Then we construct the incompleteness correction $c(M_V)$, using the probability distribution of the satellites $n(r)$. When the maximal accessible distance for a galaxy is greater than $r_{\rm LF}$, the correction is 1, if not it is equal to the ratio of number of satellites within $r_{\rm max}(M_V)$ to the number of satellites

within $r_{\rm LF}$:

$$c(M_V) = \begin{cases} \dfrac{\int_0^{r_{\max}(M_V)} n(r) r^2 \, dr}{\int_0^{r_{\rm LF}} n(r) r^2 \, dr} & if \ r_{\max}(M_V) < r_{\rm LF} \\ 1 & if \ r_{\max}(M_V) \geq r_{\rm LF} \end{cases}$$

Finally, the luminosity function is obtained by dividing the histogram of luminosities $h(M_V)$ by the incompleteness correction $c(M_V)$

References

Abadi, M. G., Moore, B., and Bower, R. G. Ram pressure stripping of spiral galaxies in clusters. *MNRAS*, 308:947–954 (1999). doi:10.1046/j.1365-8711.1999.02715.x. 2

Abadi, M. G., Navarro, J. F., Steinmetz, M., et al. Simulations of Galaxy Formation in a Λ Cold Dark Matter Universe. II. The Fine Structure of Simulated Galactic Disks. *ApJ*, 597:21–34 (2003). doi:10.1086/378316. 2

Abazajian, K. Linear cosmological structure limits on warm dark matter. *Phys. Rev. D*, 73(6):063513–+ (2006). doi:10.1103/PhysRevD.73.063513. 85

Abazajian, K. N., Adelman-McCarthy, J. K., Agüeros, M. A., et al. The Seventh Data Release of the Sloan Digital Sky Survey. *ApJS*, 182:543–558 (2009). doi:10.1088/0067-0049/182/2/543. 29

Abel, T., Bryan, G. L., and Norman, M. L. The Formation of the First Star in the Universe. *Science*, 295:93–98 (2002). doi:10.1126/science.1063991. 2

Adelman-McCarthy, J. K., Agüeros, M. A., Allam, S. S., et al. The Fourth Data Release of the Sloan Digital Sky Survey. *ApJS*, 162:38–48 (2006). doi:10.1086/497917. 57

Adelman-McCarthy, J. K., Agüeros, M. A., Allam, S. S., et al. The Sixth Data Release of the Sloan Digital Sky Survey. *ApJS*, 175:297–313 (2008). doi:10.1086/524984. 84

Aharonian, F., Akhperjanian, A. G., Bazer-Bachi, A. R., et al. The H.E.S.S. Survey of the Inner Galaxy in Very High Energy Gamma Rays. *ApJ*, 636:777–797 (2006). doi:10.1086/498013. 1

An, D., Johnson, J. A., Clem, J. L., et al. Galactic Globular and Open Clusters in the Sloan Digital Sky Survey. I. Crowded-Field Photometry and Cluster Fiducial Sequences in ugriz. *ApJS*, 179:326–354 (2008). doi:10.1086/592090. 28

REFERENCES

Babaud, J., Witkin, A. P., Baudin, M., et al. Uniqueness of the gaussian kernel for scale-space filtering. *IEEE Trans. Pattern Anal. Mach. Intell.*, 8(1):26–33 (1986). ISSN 0162-8828. 9, 59

Barkana, R. and Loeb, A. The Photoevaporation of Dwarf Galaxies during Reionization. *ApJ*, 523:54–65 (1999). doi:10.1086/307724. 92, 117

Barkana, R. and Loeb, A. In the beginning: the first sources of light and the reionization of the universe. *Phys. Rep.*, 349:125–238 (2001). doi:10.1016/S0370-1573(01)00019-9. 2

Bell, E. F., Zucker, D. B., Belokurov, V., et al. The Accretion Origin of the Milky Way's Stellar Halo. *ApJ*, 680:295–311 (2008). doi:10.1086/588032. 3

Belokurov, V., Evans, N. W., Bell, E. F., et al. The Hercules-Aquila Cloud. *ApJ*, 657:L89–L92 (2007a). doi:10.1086/513144. 21

Belokurov, V., Evans, N. W., Irwin, M. J., et al. The Discovery of Tidal Tails around the Globular Cluster NGC 5466. *ApJ*, 637:L29–L32 (2006a). doi:10.1086/500362. 76

Belokurov, V., Evans, N. W., Irwin, M. J., et al. An Orphan in the "Field of Streams". *ApJ*, 658:337–344 (2007b). doi:10.1086/511302. 21

Belokurov, V., Walker, M. G., Evans, N. W., et al. Leo V: A Companion of a Companion of the Milky Way Galaxy? *ApJ*, 686:L83–L86 (2008). doi:10.1086/592962. 99

Belokurov, V., Zucker, D. B., Evans, N. W., et al. A Faint New Milky Way Satellite in Bootes. *ApJ*, 647:L111–L114 (2006b). doi:10.1086/507324. 56, 84, 95, 114

Belokurov, V., Zucker, D. B., Evans, N. W., et al. The Field of Streams: Sagittarius and Its Siblings. *ApJ*, 642:L137–L140 (2006c). doi:10.1086/504797. 3, 14, 21, 56

Belokurov, V., Zucker, D. B., Evans, N. W., et al. Cats and Dogs, Hair and a Hero: A Quintet of New Milky Way Companions. *ApJ*, 654:897–906 (2007c). doi:10.1086/509718. 3, 8, 21, 56, 57, 68, 70, 72, 78, 79, 84, 96, 114

Benson, A. J., Bower, R. G., Frenk, C. S., et al. What Shapes the Luminosity Function of Galaxies? *ApJ*, 599:38–49 (2003). doi:10.1086/379160. 2

Benson, A. J., Lacey, C. G., Baugh, C. M., et al. The effects of photoionization on galaxy formation - I. Model and results at z=0. *MNRAS*, 333:156–176 (2002). doi: 10.1046/j.1365-8711.2002.05387.x. 1, 56, 77, 80, 96, 121

Bergström, L. Non-baryonic dark matter: observational evidence and detection methods. *Reports on Progress in Physics*, 63:793–841 (2000). doi:10.1088/0034-4885/63/5/2r3. 1

Bertin, E. Automatic Astrometric and Photometric Calibration with SCAMP. In C. Gabriel, C. Arviset, D. Ponz, and S. Enrique, editors, *Astronomical Data Analysis Software and Systems XV*, volume 351 of *Astronomical Society of the Pacific Conference Series*, pages 112–+ (2006). 11

Bertone, G., Hooper, D., and Silk, J. Particle dark matter: evidence, candidates and constraints. *Phys. Rep.*, 405:279–390 (2005). doi:10.1016/j.physrep.2004.08.031. 1

Binney, J. and Tremaine, S. *Galactic dynamics* (1987). 42

Blumenthal, G. R., Faber, S. M., Primack, J. R., et al. Formation of galaxies and large-scale structure with cold dark matter. *Nature*, 311:517–525 (1984). doi:10.1038/311517a0. 1

Bode, P., Ostriker, J. P., and Turok, N. Halo Formation in Warm Dark Matter Models. *ApJ*, 556:93–107 (2001). doi:10.1086/321541. 3, 84

Bond, J. R., Cole, S., Efstathiou, G., et al. Excursion set mass functions for hierarchical Gaussian fluctuations. *ApJ*, 379:440–460 (1991). doi:10.1086/170520. 87

Bovill, M. S. and Ricotti, M. Pre-Reionization Fossils, Ultra-Faint Dwarfs, and the Missing Galactic Satellite Problem. *ApJ*, 693:1859–1870 (2009). doi:10.1088/0004-637X/693/2/1859. 92, 117, 119

Bower, R. G., Benson, A. J., Malbon, R., et al. Breaking the hierarchy of galaxy formation. *MNRAS*, 370:645–655 (2006). doi:10.1111/j.1365-2966.2006.10519.x. 1

Brand, J. and Blitz, L. The Velocity Field of the Outer Galaxy. *A&A*, 275:67–+ (1993). 44

REFERENCES

Bruzual, G. and Charlot, S. Stellar population synthesis at the resolution of 2003. *MNRAS*, 344:1000–1028 (2003). doi:10.1046/j.1365-8711.2003.06897.x. 95

Bryan, G. L. and Norman, M. L. Statistical Properties of X-Ray Clusters: Analytic and Numerical Comparisons. *ApJ*, 495:80–+ (1998). doi:10.1086/305262. 88

Bullock, J. S. and Johnston, K. V. Tracing Galaxy Formation with Stellar Halos. I. Methods. *ApJ*, 635:931–949 (2005). doi:10.1086/497422. 3

Bullock, J. S., Kolatt, T. S., Sigad, Y., et al. Profiles of dark haloes: evolution, scatter and environment. *MNRAS*, 321:559–575 (2001a). doi:10.1046/j.1365-8711.2001.04068.x. 88

Bullock, J. S., Kravtsov, A. V., and Weinberg, D. H. Reionization and the Abundance of Galactic Satellites. *ApJ*, 539:517–521 (2000). doi:10.1086/309279. 84, 85, 86, 89, 92, 116, 119, 121

Bullock, J. S., Kravtsov, A. V., and Weinberg, D. H. Hierarchical Galaxy Formation and Substructure in the Galaxy's Stellar Halo. *ApJ*, 548:33–46 (2001b). doi:10.1086/318681. 56

Busha, M. T., Alvarez, M. A., Wechsler, R. H., et al. The Impact of Inhomogeneous Reionization on the Satellite Galaxy Population of the Milky Way. *ArXiv e-prints* (2009). 119

Carollo, D., Beers, T. C., Lee, Y. S., et al. Two stellar components in the halo of the Milky Way. *Nature*, 450:1020–1025 (2007). doi:10.1038/nature06460. 31

Carraro, G., Zinn, R., and Moni Bidin, C. Whiting 1: the youngest globular cluster associated with the Sagittarius dwarf spheroidal galaxy. *A&A*, 466:181–189 (2007). doi:10.1051/0004-6361:20066825. 15

Cash, W. Parameter estimation in astronomy through application of the likelihood ratio. *ApJ*, 228:939–947 (1979). doi:10.1086/156922. 37

Chabrier, G. The Galactic Disk Mass Budget. I. Stellar Mass Function and Density. *ApJ*, 554:1274–1281 (2001). doi:10.1086/321401. 24, 27

Clem, J. L. *Galactic star clusters in the u'g'r'i'z' photometric system*. Ph.D. thesis, University of Victoria (Canada) (2006). 67, 68

Cole, N., Newberg, H. J., Magdon-Ismail, M., et al. Maximum Likelihood Fitting of Tidal Streams with Application to the Sagittarius Dwarf Tidal Tails. *ApJ*, 683:750–766 (2008). doi:10.1086/589681. 36

Cole, S., Percival, W. J., Peacock, J. A., et al. The 2dF Galaxy Redshift Survey: power-spectrum analysis of the final data set and cosmological implications. *MNRAS*, 362:505–534 (2005). doi:10.1111/j.1365-2966.2005.09318.x. 2

Colless, M., Dalton, G., Maddox, S., et al. The 2dF Galaxy Redshift Survey: spectra and redshifts. *MNRAS*, 328:1039–1063 (2001). doi:10.1046/j.1365-8711.2001.04902.x. 1

de Jong, J. T. A., Rix, H.-W., Martin, N. F., et al. Numerical Color-Magnitude Diagram Analysis of Sloan Digital Sky Survey Data and Application to the New Milky way Satellites. *AJ*, 135:1361–1383 (2008). doi:10.1088/0004-6256/135/4/1361. 27

de Vaucouleurs, G., de Vaucouleurs, A., Corwin, Jr., H. G., et al. *Third Reference Catalogue of Bright Galaxies* (1991). 66

Dehnen, W. and Binney, J. J. Local stellar kinematics from HIPPARCOS data. *MNRAS*, 298:387–394 (1998). doi:10.1046/j.1365-8711.1998.01600.x. 44

Dehnen, W., Odenkirchen, M., Grebel, E. K., et al. Modeling the Disruption of the Globular Cluster Palomar 5 by Galactic Tides. *AJ*, 127:2753–2770 (2004). doi:10.1086/383214. 42, 44, 76

Dekel, A. and Silk, J. The origin of dwarf galaxies, cold dark matter, and biased galaxy formation. *ApJ*, 303:39–55 (1986). doi:10.1086/164050. 2

Dicke, R. H., Peebles, P. J. E., Roll, P. G., et al. Cosmic Black-Body Radiation. *ApJ*, 142:414–419 (1965). doi:10.1086/148306. 1

Diemand, J., Kuhlen, M., and Madau, P. Dark Matter Substructure and Gamma-Ray Annihilation in the Milky Way Halo. *ApJ*, 657:262–270 (2007). doi:10.1086/510736. 85

Diemand, J., Madau, P., and Moore, B. The distribution and kinematics of early high-σ peaks in present-day haloes: implications for rare objects and old stellar populations. *MNRAS*, 364:367–383 (2005). doi:10.1111/j.1365-2966.2005.09604.x. 55

Dolphin, A. E. Numerical methods of star formation history measurement and applications to seven dwarf spheroidals. *MNRAS*, 332:91–108 (2002). doi:10.1046/j.1365-8711.2002.05271.x. 27

Duda, R. O. and Hart, P. E. Use of the hough transformation to detect lines and curves in pictures. *Commun. ACM*, 15(1):11–15 (1972). ISSN 0001-0782. doi:http://doi.acm.org/10.1145/361237.361242. 126

Dunkley, J., Komatsu, E., Nolta, M. R., et al. Five-Year Wilkinson Microwave Anisotropy Probe Observations: Likelihoods and Parameters from the WMAP Data. *ApJS*, 180:306–329 (2009). doi:10.1088/0067-0049/180/2/306. 2, 92

Dutton, A. A., van den Bosch, F. C., Dekel, A., et al. A Revised Model for the Formation of Disk Galaxies: Low Spin and Dark Halo Expansion. *ApJ*, 654:27–52 (2007). doi:10.1086/509314. 117

Eisenstein, D. J. and Hu, W. Power Spectra for Cold Dark Matter and Its Variants. *ApJ*, 511:5–15 (1999). doi:10.1086/306640. 88

Eisenstein, D. J., Zehavi, I., Hogg, D. W., et al. Detection of the Baryon Acoustic Peak in the Large-Scale Correlation Function of SDSS Luminous Red Galaxies. *ApJ*, 633:560–574 (2005). doi:10.1086/466512. 2

Eyre, A. and Binney, J. Locating the orbits delineated by tidal streams. *ArXiv e-prints* (2009). 22

Fall, S. M. and Efstathiou, G. Formation and rotation of disc galaxies with haloes. *MNRAS*, 193:189–206 (1980). 1

Fan, X., Strauss, M. A., Becker, R. H., et al. Constraining the Evolution of the Ionizing Background and the Epoch of Reionization with z˜6 Quasars. II. A Sample of 19 Quasars. *AJ*, 132:117–136 (2006). doi:10.1086/504836. 2, 106

Fellhauer, M., Belokurov, V., Evans, N. W., et al. The Origin of the Bifurcation in the Sagittarius Stream. *ApJ*, 651:167–173 (2006). doi:10.1086/507128. 3, 4, 50

Fellhauer, M., Evans, N. W., Belokurov, V., et al. The tidal tails of NGC 5466. *MNRAS*, 380:749–756 (2007). doi:10.1111/j.1365-2966.2007.12111.x. 76

Ferguson, A. M. N., Irwin, M. J., Ibata, R. A., et al. Evidence for Stellar Substructure in the Halo and Outer Disk of M31. *AJ*, 124:1452–1463 (2002). doi:10.1086/342019. 3

Fukugita, M., Ichikawa, T., Gunn, J. E., et al. The Sloan Digital Sky Survey Photometric System. *AJ*, 111:1748–+ (1996). doi:10.1086/117915. 57

Geha, M., Willman, B., Simon, J. D., et al. The Least-Luminous Galaxy: Spectroscopy of the Milky Way Satellite Segue 1. *ApJ*, 692:1464–1475 (2009). doi:10.1088/0004-637X/692/2/1464. 84

Gehrels, N., Chincarini, G., Giommi, P., et al. The Swift Gamma-Ray Burst Mission. *ApJ*, 611:1005–1020 (2004). doi:10.1086/422091. 1

Ghez, A. M., Salim, S., Weinberg, N. N., et al. Measuring Distance and Properties of the Milky Way's Central Supermassive Black Hole with Stellar Orbits. *ApJ*, 689:1044–1062 (2008). doi:10.1086/592738. 44, 45, 46, 48, 50, 51, 52

Girardi, L., Bressan, A., Bertelli, G., et al. Evolutionary tracks and isochrones for low- and intermediate-mass stars: From 0.15 to 7 M_{sun}, and from Z=0.0004 to 0.03. *A&AS*, 141:371–383 (2000). doi:10.1051/aas:2000126. 13, 27, 36

Gnedin, N. Y. Effect of Reionization on Structure Formation in the Universe. *ApJ*, 542:535–541 (2000). doi:10.1086/317042. 91, 92, 98, 105, 116

Gnedin, O. Y., Kravtsov, A. V., Klypin, A. A., et al. Response of Dark Matter Halos to Condensation of Baryons: Cosmological Simulations and Improved Adiabatic Contraction Model. *ApJ*, 616:16–26 (2004). doi:10.1086/424914. 1

Gnedin, O. Y., Lee, H. M., and Ostriker, J. P. Effects of Tidal Shocks on the Evolution of Globular Clusters. *ApJ*, 522:935–949 (1999). doi:10.1086/307659. 18

Gnedin, O. Y. and Ostriker, J. P. Destruction of the Galactic Globular Cluster System. *ApJ*, 474:223–+ (1997). doi:10.1086/303441. 2, 7

Gnedin, O. Y., Weinberg, D. H., Pizagno, J., et al. Dark Matter Halos of Disk Galaxies: Constraints from the Tully-Fisher Relation. *ApJ*, 671:1115–1134 (2007). doi:10.1086/523256. 117

Grebel, E. K., Gallagher, III, J. S., and Harbeck, D. The Progenitors of Dwarf Spheroidal Galaxies. *AJ*, 125:1926–1939 (2003). doi:10.1086/368363. 2

Grillmair, C. J. Detection of a 60deg-long Dwarf Galaxy Debris Stream. *ApJ*, 645:L37–L40 (2006). doi:10.1086/505863. 21, 22

Grillmair, C. J. Four New Stellar Debris Streams in the Galactic Halo. *ApJ*, 693:1118–1127 (2009). doi:10.1088/0004-637X/693/2/1118. 3

Grillmair, C. J. and Dionatos, O. A 22deg Tidal Tail for Palomar 5. *ApJ*, 641:L37–L39 (2006a). doi:10.1086/503744. 21, 22, 53

Grillmair, C. J. and Dionatos, O. Detection of a 63deg Cold Stellar Stream in the Sloan Digital Sky Survey. *ApJ*, 643:L17–L20 (2006b). doi:10.1086/505111. 3, 21, 22, 23, 29, 42, 51

Grillmair, C. J., Freeman, K. C., Irwin, M., et al. Globular Clusters with Tidal Tails: Deep Two-Color Star Counts. *AJ*, 109:2553–+ (1995). doi:10.1086/117470. 22

Grillmair, C. J. and Johnson, R. The Detection of a 45 deg Tidal Stream Associated with the Globular Cluster NGC 5466. *ApJ*, 639:L17–L20 (2006). doi:10.1086/501439. 22

Gunn, J. E., Carr, M., Rockosi, C., et al. The Sloan Digital Sky Survey Photometric Camera. *AJ*, 116:3040–3081 (1998). doi:10.1086/300645. 57

Gunn, J. E., Siegmund, W. A., Mannery, E. J., et al. The 2.5 m Telescope of the Sloan Digital Sky Survey. *AJ*, 131:2332–2359 (2006). doi:10.1086/500975. 57

Haiman, Z., Rees, M. J., and Loeb, A. Destruction of Molecular Hydrogen during Cosmological Reionization. *ApJ*, 476:458–+ (1997). doi:10.1086/303647. 92, 117

Harris, W. E. A Catalog of Parameters for Globular Clusters in the Milky Way. *AJ*, 112:1487–+ (1996). doi:10.1086/118116. 16, 69

Helmi, A. Velocity Trends in the Debris of Sagittarius and the Shape of the Dark Matter Halo of Our Galaxy. *ApJ*, 610:L97–L100 (2004). doi:10.1086/423340. 3, 22, 50

Helmi, A., White, S. D. M., de Zeeuw, P. T., et al. Debris streams in the solar neighbourhood as relicts from the formation of the Milky Way. *Nature*, 402:53–55 (1999). doi:10.1038/46980. 3

Hernquist, L. and Mihos, J. C. Excitation of Activity in Galaxies by Minor Mergers. *ApJ*, 448:41–+ (1995). doi:10.1086/175940. 2

Hoeft, M., Yepes, G., Gottlöber, S., et al. Dwarf galaxies in voids: suppressing star formation with photoheating. *MNRAS*, 371:401–414 (2006). doi:10.1111/j.1365-2966.2006.10678.x. 92, 106, 116

Hogg, D. W., Finkbeiner, D. P., Schlegel, D. J., et al. A Photometricity and Extinction Monitor at the Apache Point Observatory. *AJ*, 122:2129–2138 (2001). doi:10.1086/323103. 57

Huxor, A. P., Tanvir, N. R., Irwin, M. J., et al. A new population of extended, luminous star clusters in the halo of M31. *MNRAS*, 360:1007–1012 (2005). doi:10.1111/j.1365-2966.2005.09086.x. 78

Ibata, R., Lewis, G. F., Irwin, M., et al. Great Circle Tidal Streams: Evidence for a Nearly Spherical Massive Dark Halo around the Milky Way. *ApJ*, 551:294–311 (2001). doi:10.1086/320060. 3, 22

Inman, R. T. and Carney, B. W. AM-4 - The poorest globular cluster? *AJ*, 93:1166–1171 (1987). doi:10.1086/114398. 8, 13

Innanen, K. A., Harris, W. E., and Webbink, R. F. Globular cluster orbits and the galactic mass distribution. *AJ*, 88:338–360 (1983). doi:10.1086/113320. 18

Irwin, M. and Hatzidimitriou, D. Structural parameters for the Galactic dwarf spheroidals. *MNRAS*, 277:1354–1378 (1995). 70

Irwin, M. J., Belokurov, V., Evans, N. W., et al. Discovery of an Unusual Dwarf Galaxy in the Outskirts of the Milky Way. *ApJ*, 656:L13–L16 (2007). doi:10.1086/512183. 8, 21, 56, 84, 114

Ivezić, Ž., Sesar, B., Jurić, M., et al. The Milky Way Tomography with SDSS. II. Stellar Metallicity. *ApJ*, 684:287–325 (2008). doi:10.1086/589678. 26, 27, 28

Jeans, J. H. *Problems of cosmogony and stellar dynamics* (1919). 96

Johnston, K. V., Law, D. R., and Majewski, S. R. A Two Micron All Sky Survey View of the Sagittarius Dwarf Galaxy. III. Constraints on the Flattening of the Galactic Halo. *ApJ*, 619:800–806 (2005). doi:10.1086/426777. 22

Kaiser, N., Aussel, H., Burke, B. E., et al. Pan-STARRS: A Large Synoptic Survey Telescope Array. In J. A. Tyson and S. Wolff, editors, *Society of Photo-Optical Instrumentation Engineers (SPIE) Conference Series*, volume 4836 of *Society of Photo-Optical Instrumentation Engineers (SPIE) Conference Series*, pages 154–164 (2002). doi:10.1117/12.457365. 125

Kamionkowski, M. and Liddle, A. R. The Dearth of Halo Dwarf Galaxies: Is There Power on Short Scales? *Physical Review Letters*, 84:4525–4528 (2000). doi:10.1103/PhysRevLett.84.4525. 84

Kauffmann, G., White, S. D. M., and Guiderdoni, B. The Formation and Evolution of Galaxies Within Merging Dark Matter Haloes. *MNRAS*, 264:201–+ (1993). 3, 83

Kazantzidis, S., Mayer, L., Mastropietro, C., et al. Density Profiles of Cold Dark Matter Substructure: Implications for the Missing-Satellites Problem. *ApJ*, 608:663–679 (2004). doi:10.1086/420840. 113

Klement, R., Rix, H.-W., Flynn, C., et al. Halo Streams in the Seventh Sloan Digital Sky Survey Data Release. *ApJ*, 698:865–894 (2009). doi:10.1088/0004-637X/698/1/865. 3

Kleyna, J., Wilkinson, M. I., Evans, N. W., et al. Dark matter in dwarf spheroidals - II. Observations and modelling of Draco. *MNRAS*, 330:792–806 (2002). doi:10.1046/j.1365-8711.2002.05155.x. 70

Klypin, A., Kravtsov, A. V., Valenzuela, O., et al. Where Are the Missing Galactic Satellites? *ApJ*, 522:82–92 (1999). doi:10.1086/307643. 2, 55, 83, 91, 104, 117, 121

Klypin, A., Zhao, H., and Somerville, R. S. ΛCDM-based Models for the Milky Way and M31. I. Dynamical Models. *ApJ*, 573:597–613 (2002). doi:10.1086/340656. 80

Koch, A., Grebel, E. K., Wyse, R. F. G., et al. Complexity on Small Scales: The Metallicity Distribution of the Carina Dwarf Spheroidal Galaxy. *AJ*, 131:895–911 (2006). doi:10.1086/499490. 3

Koposov, S. Searching for clusters and streams in large photometric surveys. In *American Institute of Physics Conference Series*, volume 1082 of *American Institute of Physics Conference Series*, pages 233–237 (2008). doi:10.1063/1.3059054. 126

Koposov, S. and Bartunov, O. Q3C, Quad Tree Cube – The new Sky-indexing Concept for Huge Astronomical Catalogues and its Realization for Main Astronomical Queries (Cone Search and Xmatch) in Open Source Database PostgreSQL. In C. Gabriel, C. Arviset, D. Ponz, and S. Enrique, editors, *Astronomical Data Analysis Software and Systems XV*, volume 351 of *Astronomical Society of the Pacific Conference Series*, pages 735–+ (2006). 57

Koposov, S., Bartunov, O., Belinskiy, A., et al. Storing and Accessing the Largest Astronomical Catalogs with the SAI CAS Project. In R. A. Shaw, F. Hill, and D. J. Bell, editors, *Astronomical Data Analysis Software and Systems XVI*, volume 376 of *Astronomical Society of the Pacific Conference Series*, pages 34–+ (2007a). 11, 57

Koposov, S., Belokurov, V., Evans, N. W., et al. The Luminosity Function of the Milky Way Satellites. *ApJ*, 686:279–291 (2008a). doi:10.1086/589911. 84, 85, 86, 95, 98, 99, 108, 116, 117, 120

Koposov, S., de Jong, J. T. A., Belokurov, V., et al. The Discovery of Two Extremely Low Luminosity Milky Way Globular Clusters. *ApJ*, 669:337–342 (2007b). doi:10.1086/521422. 21, 76, 84, 114

Koposov, S. E., Glushkova, E. V., and Zolotukhin, I. Y. Automated search for Galactic star clusters in large multiband surveys. I. Discovery of 15 new open clusters in the Galactic anticenter region. *A&A*, 486:771–777 (2008b). doi:10.1051/0004-6361:20078630. 9

Koposov, S. E., Rix, H.-W., and Hogg, D. W. Constraining the Milky Way potential with a 6-D phase-space map of the GD-1 stellar stream. *ArXiv e-prints* (2009a). 3, 4

Koposov, S. E., Yoo, J., Rix, H.-W., et al. A Quantitative Explanation of the Observed Population of Milky Way Satellite Galaxies. *ApJ*, 696:2179–2194 (2009b). doi:10.1088/0004-637X/696/2/2179. 3

Kravtsov, A. V., Gnedin, O. Y., and Klypin, A. A. The Tumultuous Lives of Galactic Dwarfs and the Missing Satellites Problem. *ApJ*, 609:482–497 (2004). doi:10.1086/421322. 84, 85, 121

Lampton, M., Margon, B., and Bowyer, S. Parameter estimation in X-ray astronomy. *ApJ*, 208:177–190 (1976). doi:10.1086/154592. 45

Law, D. R., Johnston, K. V., and Majewski, S. R. A Two Micron All-Sky Survey View of the Sagittarius Dwarf Galaxy. IV. Modeling the Sagittarius Tidal Tails. *ApJ*, 619:807–823 (2005). doi:10.1086/426779. 22, 50

Li, Y.-S., Helmi, A., De Lucia, G., et al. On the common mass scale of the Milky Way satellites. *ArXiv e-prints* (2008). 86, 113, 117

Lindeberg, T. Detecting salient blob-like image structures and their scales with a scale-space primal sketch: a method for focus-of-attention. *Int. J. Comput. Vision*, 11(3):283–318 (1993). ISSN 0920-5691. doi:http://dx.doi.org/10.1007/BF01469346. 59

Lindeberg, T. Edge detection and ridge detection with automatic scale selection. *Int. J. Comput. Vision*, 30(2):117–156 (1998). ISSN 0920-5691. doi:http://dx.doi.org/10.1023/A:1008097225773. 9, 59

Lupton, R., Gunn, J. E., Ivezić, Z., et al. The SDSS Imaging Pipelines. In F. R. Harnden, Jr., F. A. Primini, and H. E. Payne, editors, *Astronomical Data Analysis Software and Systems X*, volume 238 of *Astronomical Society of the Pacific Conference Series*, pages 269–+ (2001). 60

Lupton, R. H., Gunn, J. E., and Szalay, A. S. A Modified Magnitude System that Produces Well-Behaved Magnitudes, Colors, and Errors Even for Low Signal-to-Noise Ratio Measurements. *AJ*, 118:1406–1410 (1999). doi:10.1086/301004. 57

Macciò, A. V., Dutton, A. A., van den Bosch, F. C., et al. Concentration, spin and shape of dark matter haloes: scatter and the dependence on mass and environment. *MNRAS*, 378:55–71 (2007). doi:10.1111/j.1365-2966.2007.11720.x. 88

Macciò, A. V., Kang, X., and Moore, B. Central Mass and Luminosity of Milky Way Satellites in the Λ Cold Dark Matter Model. *ApJ*, 692:L109–L112 (2009). doi:10.1088/0004-637X/692/2/L109. 86, 113, 117

Machacek, M. E., Bryan, G. L., and Abel, T. Simulations of Pregalactic Structure Formation with Radiative Feedback. *ApJ*, 548:509–521 (2001). doi:10.1086/319014. 92, 117

Mackey, A. D. and Gilmore, G. F. Comparing the properties of local globular cluster systems: implications for the formation of the Galactic halo. *MNRAS*, 355:504–534 (2004). doi:10.1111/j.1365-2966.2004.08343.x. 76

Madau, P., Kuhlen, M., Diemand, J., et al. Fossil Remnants of Reionization in the Halo of the Milky Way. *ApJ*, 689:L41–L44 (2008). doi:10.1086/595814. 118

Majewski, S. R., Skrutskie, M. F., Weinberg, M. D., et al. A Two Micron All Sky Survey View of the Sagittarius Dwarf Galaxy. I. Morphology of the Sagittarius Core and Tidal Arms. *ApJ*, 599:1082–1115 (2003). doi:10.1086/379504. 3

Mandelbaum, R., Seljak, U., Kauffmann, G., et al. Galaxy halo masses and satellite fractions from galaxy-galaxy lensing in the Sloan Digital Sky Survey: stellar mass, luminosity, morphology and environment dependencies. *MNRAS*, 368:715–731 (2006). doi:10.1111/j.1365-2966.2006.10156.x. 117

Marigo, P., Girardi, L., Bressan, A., et al. Evolution of asymptotic giant branch stars. II. Optical to far-infrared isochrones with improved TP-AGB models. *A&A*, 482:883–905 (2008). doi:10.1051/0004-6361:20078467. 26, 27, 37

Markwardt, C. B. Non-linear Least Squares Fitting in IDL with MPFIT. *ArXiv e-prints* (2009). 44

Marquardt, D. W. An algorithm for least-squares estimation of nonlinear parameters. 11(2):431–441 (1963). ISSN 0368-4245. 44

Martin, C. L. Properties of Galactic Outflows: Measurements of the Feedback from Star Formation. *ApJ*, 513:156–160 (1999). doi:10.1086/306863. 2

Martin, N. F., de Jong, J. T. A., and Rix, H.-W. A Comprehensive Maximum Likelihood Analysis of the Structural Properties of Faint Milky Way Satellites. *ApJ*, 684:1075–1092 (2008). doi:10.1086/590336. 84, 95, 97, 99

Martin, N. F., Ibata, R. A., Chapman, S. C., et al. A Keck/DEIMOS spectroscopic survey of faint Galactic satellites: searching for the least massive dwarf galaxies. *MNRAS*, 380:281–300 (2007). doi:10.1111/j.1365-2966.2007.12055.x. 56, 79, 84, 96

Mateo, M. L. Dwarf Galaxies of the Local Group. *ARA&A*, 36:435–506 (1998). doi:10.1146/annurev.astro.36.1.435. 99

Metz, M. and Kroupa, P. Dwarf spheroidal satellites: are they of tidal origin? *MNRAS*, 376:387–392 (2007). doi:10.1111/j.1365-2966.2007.11438.x. 77, 80, 99

Meylan, G. and Heggie, D. C. Internal dynamics of globular clusters. *A&A Rev.*, 8:1–143 (1997). doi:10.1007/s001590050008. 7, 15

Miyamoto, M. and Nagai, R. Three-dimensional models for the distribution of mass in galaxies. *PASJ*, 27:533–543 (1975). 50

Monet, D. G., Levine, S. E., Canzian, B., et al. The USNO-B Catalog. *AJ*, 125:984–993 (2003). doi:10.1086/345888. 10, 29

Moore, B., Diemand, J., Madau, P., et al. Globular clusters, satellite galaxies and stellar haloes from early dark matter peaks. *MNRAS*, 368:563–570 (2006). doi:10.1111/j.1365-2966.2006.10116.x. 55

Moore, B., Ghigna, S., Governato, F., et al. Dark Matter Substructure within Galactic Halos. *ApJ*, 524:L19–L22 (1999). doi:10.1086/312287. 2, 55, 83, 91, 104, 118, 121

Munn, J. A., Monet, D. G., Levine, S. E., et al. An Improved Proper-Motion Catalog Combining USNO-B and the Sloan Digital Sky Survey. *AJ*, 127:3034–3042 (2004). doi:10.1086/383292. 29, 33

Munn, J. A., Monet, D. G., Levine, S. E., et al. Erratum: "an Improved Proper-Motion Catalog Combining Usno-B and the Sloan Digital Sky Survey" (2004, AJ, 127, 3034). *AJ*, 136:895–+ (2008). doi:10.1088/0004-6256/136/2/895. 29

Narayanan, V. K., Spergel, D. N., Davé, R., et al. Constraints on the Mass of Warm Dark Matter Particles and the Shape of the Linear Power Spectrum from the Lyα Forest. *ApJ*, 543:L103–L106 (2000). doi:10.1086/317269. 3, 85

Nash, S. G. Newton-type minimization via the Lánczos method. *SIAM J. Numer. Anal.*, 21(4):770–788 (1984). 37

Navarro, J. F., Frenk, C. S., and White, S. D. M. A Universal Density Profile from Hierarchical Clustering. *ApJ*, 490:493–+ (1997). doi:10.1086/304888. 88

Newberg, H. J., Yanny, B., Rockosi, C., et al. The Ghost of Sagittarius and Lumps in the Halo of the Milky Way. *ApJ*, 569:245–274 (2002). doi:10.1086/338983. 21

Odenkirchen, M., Grebel, E. K., Dehnen, W., et al. The Extended Tails of Palomar 5: A 10deg Arc of Globular Cluster Tidal Debris. *AJ*, 126:2385–2407 (2003). doi:10.1086/378601. 22

Odenkirchen, M., Grebel, E. K., Kayser, A., et al. Kinematics of the Tidal Debris of the Globular Cluster Palomar 5. *AJ*, 137:3378–3387 (2009). doi:10.1088/0004-6256/137/2/3378. 22

Odenkirchen, M., Grebel, E. K., Rockosi, C. M., et al. Detection of Massive Tidal Tails around the Globular Cluster Palomar 5 with Sloan Digital Sky Survey Commissioning Data. *ApJ*, 548:L165–L169 (2001). doi:10.1086/319095. 3, 8, 21, 22, 53, 76

Okamoto, T., Gao, L., and Theuns, T. Mass loss of galaxies due to an ultraviolet background. *MNRAS*, 390:920–928 (2008). doi:10.1111/j.1365-2966.2008.13830.x. 92, 106, 116

Orban, C., Gnedin, O. Y., Weisz, D. R., et al. Delving Deeper into the Tumultuous Lives of Galactic Dwarfs: Modeling Star Formation Histories. *ApJ*, 686:1030–1044 (2008). doi:10.1086/591496. 86, 120

O'Shea, B. W. and Norman, M. L. Population III Star Formation in a ΛCDM Universe. II. Effects of a Photodissociating Background. *ApJ*, 673:14–33 (2008). doi:10.1086/524006. 92, 117

Page, L., Hinshaw, G., Komatsu, E., et al. Three-Year Wilkinson Microwave Anisotropy Probe (WMAP) Observations: Polarization Analysis. *ApJS*, 170:335–376 (2007). doi:10.1086/513699. 80

Peñarrubia, J., Navarro, J. F., and McConnachie, A. W. The Tidal Evolution of Local Group Dwarf Spheroidals. *ApJ*, 673:226–240 (2008). doi:10.1086/523686. 91, 96

Peebles, P. J. E. Recombination of the Primeval Plasma. *ApJ*, 153:1–+ (1968). doi:10.1086/149628. 1

Perryman, M. A. C., de Boer, K. S., Gilmore, G., et al. GAIA: Composition, formation and evolution of the Galaxy. *A&A*, 369:339–363 (2001). doi:10.1051/0004-6361:20010085. 4, 23, 125

Pier, J. R., Munn, J. A., Hindsley, R. B., et al. Astrometric Calibration of the Sloan Digital Sky Survey. *AJ*, 125:1559–1579 (2003). doi:10.1086/346138. 57

Piotto, G., Bedin, L. R., Anderson, J., et al. A Triple Main Sequence in the Globular Cluster NGC 2808. *ApJ*, 661:L53–L56 (2007). doi:10.1086/518503. 78

Piotto, G., De Angeli, F., King, I. R., et al. Relative Frequencies of Blue Stragglers in Galactic Globular Clusters: Constraints for the Formation Mechanisms. *ApJ*, 604:L109–L112 (2004). doi:10.1086/383617. 14

Pizagno, J., Prada, F., Weinberg, D. H., et al. Dark Matter and Stellar Mass in the Luminous Regions of Disk Galaxies. *ApJ*, 633:844–856 (2005). doi:10.1086/491614. 117

Plummer, H. C. On the problem of distribution in globular star clusters. *MNRAS*, 71:460–470 (1911). 96

Press, W. H. and Schechter, P. Formation of Galaxies and Clusters of Galaxies by Self-Similar Gravitational Condensation. *ApJ*, 187:425–438 (1974). doi:10.1086/152650. 87

Prugniel, P., Soubiran, C., Koleva, M., et al. New release of the ELODIE library: Version 3.1. *ArXiv Astrophysics e-prints* (2007). 35

Quinn, T., Katz, N., and Efstathiou, G. Photoionization and the formation of dwarf galaxies. *MNRAS*, 278:L49–L54 (1996). 2, 89, 91, 116

Reid, M. J. and Brunthaler, A. The Proper Motion of Sagittarius A*. II. The Mass of Sagittarius A*. *ApJ*, 616:872–884 (2004). doi:10.1086/424960. 45

Reid, M. J., Menten, K. M., Zheng, X. W., et al. Trigonometric Parallaxes of Massive Star Forming Regions: VI. Galactic Structure, Fundamental Parameters and Non-Circular Motions. *ArXiv e-prints* (2009). 44

Ricotti, M. and Gnedin, N. Y. Formation Histories of Dwarf Galaxies in the Local Group. *ApJ*, 629:259–267 (2005). doi:10.1086/431415. 3

Riess, A. G., Strolger, L.-G., Tonry, J., et al. Type Ia Supernova Discoveries at z ¿ 1 from the Hubble Space Telescope: Evidence for Past Deceleration and Constraints on Dark Energy Evolution. *ApJ*, 607:665–687 (2004). doi:10.1086/383612. 1

Rockosi, C. M., Odenkirchen, M., Grebel, E. K., et al. A Matched-Filter Analysis of the Tidal Tails of the Globular Cluster Palomar 5. *AJ*, 124:349–363 (2002). doi:10.1086/340957. 22, 29

Rubin, V. C., Thonnard, N., and Ford, Jr., W. K. Extended rotation curves of high-luminosity spiral galaxies. IV - Systematic dynamical properties, SA through SC. *ApJ*, 225:L107–L111 (1978). doi:10.1086/182804. 1

Salvadori, S. and Ferrara, A. Ultra faint dwarfs: probing early cosmic star formation. *MNRAS*, 395:L6–L10 (2009). doi:10.1111/j.1745-3933.2009.00627.x. 119, 120

Salvadori, S., Ferrara, A., and Schneider, R. Life and times of dwarf spheroidal galaxies. *MNRAS*, 386:348–358 (2008). doi:10.1111/j.1365-2966.2008.13035.x. 120

Sarajedini, A., Bedin, L. R., Chaboyer, B., et al. The ACS Survey of Galactic Globular Clusters. I. Overview and Clusters without Previous Hubble Space Telescope Photometry. *AJ*, 133:1658–1672 (2007). doi:10.1086/511979. 15

Schlegel, D. J., Finkbeiner, D. P., and Davis, M. Maps of Dust Infrared Emission for Use in Estimation of Reddening and Cosmic Microwave Background Radiation Foregrounds. *ApJ*, 500:525–+ (1998). doi:10.1086/305772. 57

Searle, L. and Zinn, R. Compositions of halo clusters and the formation of the galactic halo. *ApJ*, 225:357–379 (1978). doi:10.1086/156499. 3

Seljak, U., Makarov, A., McDonald, P., et al. Can Sterile Neutrinos Be the Dark Matter? *Physical Review Letters*, 97(19):191303–+ (2006). doi:10.1103/PhysRevLett.97.191303. 85

Shaw, L. D., Weller, J., Ostriker, J. P., et al. Statistics of Physical Properties of Dark Matter Clusters. *ApJ*, 646:815–833 (2006). doi:10.1086/505016. 88

Silverman, B. W. *Density estimation for statistics and data analysis* (1986). 59

Simha, V., Weinberg, D. H., Dave, R., et al. The Growth of Central and Satellite Galaxies in Cosmological Smoothed Particle Hydrodynamics Simulations. *ArXiv e-prints* (2008). 91

Simon, J. D. and Geha, M. The Kinematics of the Ultra-faint Milky Way Satellites: Solving the Missing Satellite Problem. *ApJ*, 670:313–331 (2007). doi:10.1086/521816. 84, 93, 96, 111, 117

Smith, J. A., Tucker, D. L., Kent, S., et al. The u'g'r'i'z' Standard-Star System. *AJ*, 123:2121–2144 (2002). doi:10.1086/339311. 11, 57

Somerville, R. S. Can Photoionization Squelching Resolve the Substructure Crisis? *ApJ*, 572:L23–L26 (2002). doi:10.1086/341444. 56, 77, 80, 84, 86, 121

Somerville, R. S. and Primack, J. R. Semi-analytic modelling of galaxy formation: the local Universe. *MNRAS*, 310:1087–1110 (1999). doi:10.1046/j.1365-8711.1999.03032.x. 1

Sosin, C. and King, I. R. Deep HST/FOC Imaging of the Central Density Cusp of the Globular Cluster M15. *AJ*, 113:1328–1345 (1997). doi:10.1086/118346. 7

Spergel, D. N., Bean, R., Doré, O., et al. Three-Year Wilkinson Microwave Anisotropy Probe (WMAP) Observations: Implications for Cosmology. *ApJS*, 170:377–408 (2007). doi:10.1086/513700. 1, 88

Spergel, D. N. and Steinhardt, P. J. Observational Evidence for Self-Interacting Cold Dark Matter. *Physical Review Letters*, 84:3760–3763 (2000). doi:10.1103/PhysRevLett.84.3760. 84

Spitzer, L. *Dynamical evolution of globular clusters* (1987). 15

Springel, V., Di Matteo, T., and Hernquist, L. Modelling feedback from stars and black holes in galaxy mergers. *MNRAS*, 361:776–794 (2005). doi:10.1111/j.1365-2966.2005.09238.x. 2

Stetson, P. B. DAOPHOT - A computer program for crowded-field stellar photometry. *PASP*, 99:191–222 (1987). doi:10.1086/131977. 11

Stoehr, F., White, S. D. M., Tormen, G., et al. The satellite population of the Milky Way in a ΛCDM universe. *MNRAS*, 335:L84–L88 (2002). doi:10.1046/j.1365-8711.2002.05891.x. 55, 85

Stoughton, C., Lupton, R. H., Bernardi, M., et al. Sloan Digital Sky Survey: Early Data Release. *AJ*, 123:485–548 (2002). doi:10.1086/324741. 57, 60

Strigari, L. E., Bullock, J. S., Kaplinghat, M., et al. Redefining the Missing Satellites Problem. *ApJ*, 669:676–683 (2007). doi:10.1086/521914. 86, 93, 96

Strigari, L. E., Bullock, J. S., Kaplinghat, M., et al. A common mass scale for satellite galaxies of the Milky Way. *Nature*, 454:1096–1097 (2008). doi:10.1038/nature07222. 84, 86, 110, 112, 113, 114, 117

Tegmark, M., Eisenstein, D. J., Strauss, M. A., et al. Cosmological constraints from the SDSS luminous red galaxies. *Phys. Rev. D*, 74(12):123507–+ (2006). doi:10.1103/PhysRevD.74.123507. 1, 88

Thoul, A. A. and Weinberg, D. H. Hydrodynamic Simulations of Galaxy Formation. II. Photoionization and the Formation of Low-Mass Galaxies. *ApJ*, 465:608–+ (1996). doi:10.1086/177446. 2, 89, 91, 116

Tinker, J. L. and Conroy, C. The Void Phenomenon Explained. *ApJ*, 691:633–639 (2009). doi:10.1088/0004-637X/691/1/633. 93

Tollerud, E. J., Bullock, J. S., Strigari, L. E., et al. Hundreds of Milky Way Satellites? Luminosity Bias in the Satellite Luminosity Function. *ApJ*, 688:277–289 (2008). doi:10.1086/592102. 85, 95, 108

Tucker, D. L., Kent, S., Richmond, M. W., et al. The Sloan Digital Sky Survey monitor telescope pipeline. *Astronomische Nachrichten*, 327:821–+ (2006). doi:10.1002/asna.200610655. 57

Tyson, J. A. Large Synoptic Survey Telescope: Overview. In J. A. Tyson and S. Wolff, editors, *Society of Photo-Optical Instrumentation Engineers (SPIE) Conference Series*, volume 4836 of *Society of Photo-Optical Instrumentation Engineers (SPIE) Conference Series*, pages 10–20 (2002). doi:10.1117/12.456772. 126

van den Bergh, S. *The Galaxies of the Local Group*. Cambridge (2000). 70

van den Bosch, F. C., Yang, X., Mo, H. J., et al. Towards a concordant model of halo occupation statistics. *MNRAS*, 376:841–860 (2007). doi:10.1111/j.1365-2966.2007.11493.x. 2, 91

Viel, M., Lesgourgues, J., Haehnelt, M. G., et al. Constraining warm dark matter candidates including sterile neutrinos and light gravitinos with WMAP and the Lyman-α forest. *Phys. Rev. D*, 71(6):063534–+ (2005). doi:10.1103/PhysRevD.71.063534. 85

Walker, M. G., Mateo, M., Olszewski, E. W., et al. Velocity Dispersion Profiles of Seven Dwarf Spheroidal Galaxies. *ApJ*, 667:L53–L56 (2007). doi:10.1086/521998. 96

Walsh, S. M., Jerjen, H., and Willman, B. A Pair of Boötes: A New Milky Way Satellite. *ApJ*, 662:L83–L86 (2007). doi:10.1086/519684. 21, 56, 67, 84, 99, 114

Walsh, S. M., Willman, B., and Jerjen, H. The Invisibles: A Detection Algorithm to Trace the Faintest Milky Way Satellites. *AJ*, 137:450–469 (2009). doi:10.1088/0004-6256/137/1/450. 85, 95, 116

Weinberg, D. H., Hernquist, L., and Katz, N. Photoionization, Numerical Resolution, and Galaxy Formation. *ApJ*, 477:8–+ (1997). doi:10.1086/303683. 91

Weinmann, S. M., Macciò, A. V., Iliev, I. T., et al. Dependence of the local reionization history on halo mass and environment: did Virgo reionize the Local Group? *MNRAS*, 381:367–376 (2007). doi:10.1111/j.1365-2966.2007.12279.x. 92

White, S. D. M. and Rees, M. J. Core condensation in heavy halos - A two-stage theory for galaxy formation and clustering. *MNRAS*, 183:341–358 (1978). 1, 2

Whiting, A. B., Hau, G. K. T., and Irwin, M. The Southern Dwarf Hunt: Local Group Dwarf Candidates in the Southern Sky. *ApJS*, 141:123–146 (2002). doi:10.1086/340037. 8

Whiting, A. B., Hau, G. K. T., Irwin, M., et al. An Observational Limit on the Dwarf Galaxy Population of the Local Group. *AJ*, 133:715–733 (2007). doi:10.1086/510309. 56

Wilkinson, M. I., Kleyna, J., Evans, N. W., et al. Dark matter in dwarf spheroidals - I. Models. *MNRAS*, 330:778–791 (2002). doi:10.1046/j.1365-8711.2002.05154.x. 96

Willett, B. A., Newberg, H. J., Zhang, H., et al. An Orbit Fit for the Grillmair Dionatos Cold Stellar Stream. *ApJ*, 697:207–223 (2009). doi:10.1088/0004-637X/697/1/207. 22, 28, 29, 42, 51, 53

Willman, B., Blanton, M. R., West, A. A., et al. A New Milky Way Companion: Unusual Globular Cluster or Extreme Dwarf Satellite? *AJ*, 129:2692–2700 (2005a). doi:10.1086/430214. 56, 66

Willman, B., Dalcanton, J., Ivezić, Ž., et al. An SDSS Survey For Resolved Milky Way Satellite Galaxies. I. Detection Limits. *AJ*, 123:848–854 (2002). doi:10.1086/338438. 56

Willman, B., Dalcanton, J. J., Martinez-Delgado, D., et al. A New Milky Way Dwarf Galaxy in Ursa Major. *ApJ*, 626:L85–L88 (2005b). doi:10.1086/431760. 8, 56, 57, 66, 84, 114

Wise, J. H. and Abel, T. Suppression of H_2 Cooling in the Ultraviolet Background. *ApJ*, 671:1559–1567 (2007). doi:10.1086/522876. 92, 117

Xue, X. X., Rix, H. W., Zhao, G., et al. The Milky Way's Circular Velocity Curve to 60 kpc and an Estimate of the Dark Matter Halo Mass from the Kinematics of ˜2400 SDSS Blue Horizontal-Branch Stars. *ApJ*, 684:1143–1158 (2008). doi:10.1086/589500. 31, 44, 50, 51, 52, 85, 117

Yanny, B., Rockosi, C., Newberg, H. J., et al. SEGUE: A Spectroscopic Survey of 240,000 Stars with g = 14-20. *AJ*, 137:4377–4399 (2009). doi:10.1088/0004-6256/137/5/4377. 32

Yoo, J., Miralda-Escudé, J., Weinberg, D. H., et al. The Most Massive Black Holes in the Universe: Effects of Mergers in Massive Galaxy Clusters. *ApJ*, 667:813–825 (2007). doi:10.1086/521015. 87, 88

York, D. G., Adelman, J., Anderson, Jr., J. E., et al. The Sloan Digital Sky Survey: Technical Summary. *AJ*, 120:1579–1587 (2000). doi:10.1086/301513. 1, 8, 56, 84

Zentner, A. R., Berlind, A. A., Bullock, J. S., et al. The Physics of Galaxy Clustering. I. A Model for Subhalo Populations. *ApJ*, 624:505–525 (2005). doi:10.1086/428898. 88

Zentner, A. R. and Bullock, J. S. Halo Substructure and the Power Spectrum. *ApJ*, 598:49–72 (2003). doi:10.1086/378797. 3, 84

Zinnecker, H., Keable, C. J., Dunlop, J. S., et al. The Nuclei of Nucleated Dwarf Elliptical Galaxies - are they Globular Clusters? In J. E. Grindlay and A. G. D. Philip, editors, *The Harlow-Shapley Symposium on Globular Cluster Systems in Galaxies*, volume 126 of *IAU Symposium*, pages 603–+ (1988). 78

Zucker, D. B., Belokurov, V., Evans, N. W., et al. A Curious Milky Way Satellite in Ursa Major. *ApJ*, 650:L41–L44 (2006a). doi:10.1086/508628. 56, 68, 70, 72, 76

Zucker, D. B., Belokurov, V., Evans, N. W., et al. A New Milky Way Dwarf Satellite in Canes Venatici. *ApJ*, 643:L103–L106 (2006b). doi:10.1086/505216. 8, 56, 68, 72, 84, 114

Zwicky, F. Die Rotverschiebung von extragalaktischen Nebeln. *Helvetica Physica Acta*, 6:110–127 (1933). 1

Acknowledgements

I would like thank my advisor Prof. Dr. Hans-Walter Rix for his great help and support during my PhD. Also would like to thank my collaborators for their assistance throughout my PhD: Vasily Belokurov, Wyn Evans, David Hogg, David Weinberg, Jaiyul Yoo, Paul Hewett, Jelte de Jong, Andrea Macciò, Nicolas Martin. I'm also thankful to my friends: Dima Semenov, Tanya and Anton Vasyunin, Yaroslav Pavlyuchenkov for enjoyable years in Heidelberg.